2013

CAVITATION NANOBUBBLE ENHANCED FLOTATION PROCESS FOR MORE EFFICIENT COAL RECOVERY

Ahmed S. Sayed Ahmed
University of Kentucky, asobhy81@gmail.com

STUDENT AGREEMENT:

I represent that my thesis or dissertation and abstract are my original work. Proper attribution has been given to all outside sources. I understand that I am solely responsible for obtaining any needed copyright permissions. I have obtained and attached hereto needed written permission statements(s) from the owner(s) of each third-party copyrighted matter to be included in my work, allowing electronic distribution (if such use is not permitted by the fair use doctrine).

I hereby grant to The University of Kentucky and its agents the non-exclusive license to archive and make accessible my work in whole or in part in all forms of media, now or hereafter known. I agree that the document mentioned above may be made available immediately for worldwide access unless a preapproved embargo applies.

I retain all other ownership rights to the copyright of my work. I also retain the right to use in future works (such as articles or books) all or part of my work. I understand that I am free to register the copyright to my work.

REVIEW, APPROVAL AND ACCEPTANCE

The document mentioned above has been reviewed and accepted by the student's advisor, on behalf of the advisory committee, and by the Director of Graduate Studies (DGS), on behalf of the program; we verify that this is the final, approved version of the student's dissertation including all changes required by the advisory committee. The undersigned agree to abide by the statements above.

Ahmed S. Sayed Ahmed, Student

Dr. Daniel Tao, Major Professor

Dr. Tom Novak, Director of Graduate Studies

CAVITATION NANOBUBBLE ENHANCED FLOTATION PROCESS FOR MORE EFFICIENT COAL RECOVERY

DISSERTATION

A dissertation submitted in partial fulfillment of the requirements for the degree of Doctor of Philosophy in the College of Engineering at the University of Kentucky

By
Ahmed Sobhy Sayed-Ahmed

Lexington, Kentucky

Director: Dr. Daniel Tao, Professor of Mining Engineering

Lexington, Kentucky

2013

ABSTRACT OF DISSERTATION

CAVITATION NANOBUBBLE ENHANCED
FLOTATION PROCESS FOR MORE EFFICIENT COAL RECOVERY

Froth flotation is a widely used, cost effective particle separation process. However, its high performance is limited to a narrow particle size range, e.g., between 50 μm and 600 μm for coal and between 10 μm and 100 μm for minerals. Outside this range, the efficiency of froth flotation decreases significantly, especially for difficult-to-float particles of weak hydrophobicity (e.g., oxidized coal).

Nanobubbles integrated into a specially designed column flotation expanded the particle size range for efficient froth flotation as a result of increased probabilities of particle-bubble collision and attachment and reduced probability of detachment.

The major advantages of nanobubble enhanced flotation include lower collector and frother dosages since nanobubbles that are mostly smaller than 1 μm can be formed selectively on hydrophobic coal particles from dissolved air in coal slurry. Nanobubbles act as a secondary collector on particle surfaces, thereby resulting in considerably lower operating costs.

A systematic parametric investigation of the proposed technology was performed to understand the effects of process variables on separation performance with a typical coal sample using a specially designed flotation column and three 10-liters conventional flotation cells. Results indicate that the combustible recovery of a -150 μm coal increased by 5-50% in the presence of nanobubbles, depending on process operating conditions. Nanobubbles also significantly improved process separation efficiency and increased the flotation rate constant by more than 40%.

Theoretical evaluation of the innovative flotation technology was employed using specially designed apparatus to study the nanobubbles stability and the roles of nanobubbles on particle-bubble interactions, froth stability, and surface area flux. In addition, a detailed technical performance and economic evaluation was performed.

KEYWORDS: Nanobubble, Cavitation, Froth Flotation, Coal, Column Flotation

Ahmed Sobhy Sayed Ahmed

Student's Signature

8/21/2013

Date

CAVITATION NANOBUBBLE ENHANCED
FLOTATION PROCESS FOR MORE EFFICIENT COAL RECOVERY

By

Ahmed Sobhy Sayed-Ahmed

Dr. Daniel Tao

Director of Dissertation

Dr. Tom Novak

Director of Graduate Studies

8/21/2013

ACKNOWLEDGMENTS

I would like to express my sincere thanks to my advisor, Dr. Daniel Tao, for his guidance, motivation, and continual support throughout this work. Without his valuable expertise, participation and very helpful subject-related suggestions, the achievement of this work would not be possible.

I would like also to express my deepest gratitude to my dissertation committee members, Dr. Rick Q. Honaker, professor of Mining Engineering, Dr. James McDonough, professor of Mechanical Engineering, Dr. Tianxiang Li, associate professor of Mechanical Engineering and Dr. B. K. Parekh, associate professor of Mineral Processing for their guidance, valuable help, enthusiasm and suggestion. Special thanks to Mr. Ed Thompson for his assistance in the laboratory, his efforts of ensuring that the laboratory equipment is as practical, useful and efficient as plausible.

I wish to acknowledge the ICCI institute for the financial support. The project manager, Joseph Hirschi who provided valuable advice and support, which is greatly appreciated. Special thanks are given to Mach Coal Mine for providing the coal slurry sample employed in this study.

Finally, I wish to express my gratitude to my wife Amany Refaat Abdel-Wahid, my sons Musfata and Refaat, my daughter Mayar and the rest of my precious family. Without their patience, unselfish support and understanding such undertaking would not all have been possible. I want give special thanks to my mother Samia Metualli Salem, my brother Mohamed Sobhy, my sister Fatma Sobhy, and my parents-in-law, Refaat Abdel-Wahid and Mona Metualli Salem, for their great patience.

TABLE OF CONTENTS

LIST OF TABLES

LIST OF FIGURES

CHAPTER 1. INTRODUCTION

1.1. BACKGROUND

Worldwide most electricity is generated from coal and a majority of steel is produced today using coal as a reducing agent. Coal is also widely used in cement manufacture and other industries (World Coal Association, 2012). The United States is one of the largest users and producers of coal (U.S. Energy Information Administration, 2009). There are two main types of coal: low rank coal and high rank coal. Coal ranking is determined by degree of transformation of the original plant materials to carbon. Therefore, low rank coal, which can be subdivided into lignite and subbituminous, is low in carbon and energy value but high in hydrogen and oxygen contents. On the other hand, high rank coal, which can be subdivided into bituminous and anthracite, is high in carbon and therefore energy value but low in hydrogen and oxygen contents.

Coal has to be cleaned prior to its usage, and froth flotation is the most popular method in the industry for cleaning -600 μm or -150 μm coal particles from gangue minerals. Froth flotation exploits the difference in surface hydrophobicity of different particles. It is most efficient and cost effective for particles within a narrow size range, nominally from 50 μm to 600 μm for coal and from 10 μm to 100 μm for minerals (Feng and Aldrich, 1999; King, 1982; Trahar and Warren, 1976). The lower and upper particle size limits are determined by the probabilities of collision, attachment, and detachment (Tao, 2004). Previous studies have demonstrated that the flotation recovery of coal particles of poor floatability can be enhanced by use of nanobubbles (Tao et al., 2006; Tao et al., 2008; Fan et al., 2010d; Tao, Fan and Honaker, 2010).

Nanobubbles are nanoscopic bubbles that can be created by several methods such as ultrasonic (Farmer, Collings and Jameson, 2000; Kim, Song and Kim, 2000), solvent exchange (Lou et al., 2000; Paxton et al., 2004; Zhang et al., 2005; Zhang et al., 2006a; Zhang, Khan and Ducker, 2007; Hampton, Donose and Nguyen, 2008; Yang et al, 2009; Zhang and Maeda, 2011), pressure reduction (hydrodynamic cavitation) (Zhou et al.,

1997; Johnson and Cooke, 1981), or temperature change (Zhang, Khan and Ducker, 2007; Yang et al, 2007; Seddon et al., 2011). Nanobubbles selectively nucleate at the surface of hydrophobic particles (Zhou et al., 1997) because work of adhesion between a solid particle and water is always smaller than work of cohesion of water. Furthermore, work of adhesion decreases with increasing solid surface hydrophobicity measured by the contact angle (Zhou et al., 1997; Luttrell and Yoon, 1992).

1.2. OBJECTIVES

The overall objective of the dissertation was to study a cavitation nanobubble flotation process for enhanced recovery of coal particles by improving bubble-particle collision and attachment probabilities and by minimizing detachment probability. The specific objectives included:

- Reviewing fundamental characteristics of nanobubble formation, size distribution, stability and their effects on the froth flotation process.
- Developing a 5.08 cm diameter laboratory flotation column utilizing dual bubble generators that produce both nanobubbles (smaller than 1 μm) and regular sized bubbles of about 500 μm.
- Evaluating the specially designed flotation column to understand effects of different process variables on separation performance with a typical coal sample.
- Investigating a bank of three 10-liters conventional flotation cells integrated with nanobubble technology.
- Studying the fundamental roles of nanobubbles on particle-bubble interactions, froth stability, and surface area flux using specially designed apparatus.
- Evaluating the detailed technical and economic aspects of the innovative technology.

1.3. ORGANIZATION

The dissertation was organized into 6 chapters. Chapter 1 is an introduction. Chapter 2 is a comprehensive literature review and theoretical considerations on the subject of nanobubble enhanced froth flotation.

Extensive experimental work and theoretical study were performed. The experimental setups, procedures and measurement techniques are described in Chapter 3. Experimental results, observations, and discussions are given in Chapter 4 which is divided into six sections: section 4.1 is for sample characterization; section 4.2 is for specially designed laboratory column flotation; section 4.3 is for the bank of three 10-liters mechanical flotation cells; section 4.4 is for fundamental characterization of nanobubbles; 4.5 is for fundamental studies of nanobubble roles on particle-bubble interaction, froth stability, and surface are flux; and section 4.6 is for technical performance and economic evaluation of the proposed technology.

The conclusions of this study are presented in Chapter 5. Finally Chapter 6 contains suggestions for further study derived from a review of the results of this work.

CHAPTER 2. LITERTURE REVIEW & THEORITICAL CONSIDERATIONS

2.1. FUNDAMENTALS OF NANOBUBBLES

2.1.1. Formation

Generation of nanobubbles, which are tiny bubbles smaller than 1 μm, can be induced by a number of methods such as:

- Power ultrasonic: Ultrasonic waves reduce the pressure sharply below the saturated vapor pressure, causing the dissolved air to separate out as bubbles.
- Solvent exchange: A liquid of higher gas solubility is used to replace one of lower gas solubility to release the gas in forms of nanobubbles.
- Temperature change: Increasing the temperature of the solution decrease gas solubility and increases the gas released to produce nanobubbles.
- Turbulent flow (shearing): Nanobubbles are produced by cavitation tube or swirl flows.
- Microporous (sintered material): Nanobubbles are generated by blowing gas through a sintered or loosely bonded ceramic, metal, and glass with nanoscale open pores or a glass tube extended into a small diameter in the liquid.
- Electrolysis: Oxygen and hydrogen nanobubbles are produced by generating oxygen and hydrogen gases at the electrolysis electrodes. It is mainly used in electroflotation technique.
- Chemical reaction: Gas generated by chemical reactions produces tiny bubbles. For example, carbon dioxide produced by mixing acid with carbonate is used in a reactive flotation technique.

The most common method in froth flotation is the pressure reduction by hydrodynamic cavitation which is a process of creation of nanobubbles in a liquid as a result of the rupture of a liquid-liquid interface (work of cohesion of water W_c) or at a liquid-solid interface due to the rupture of a liquid-solid interface (work of adhesion W_a between water and solid). It takes place when the liquid pressure P is reduced to below a critical value with abrupt increase in the flow velocity U (Young, 1989), which is well described in Bernoulli's Equation (1):

$$P + \frac{1}{2}\rho U^2 = C \tag{1}$$

where ρ is water density.

W_c and W_a can be expressed in Equations (2) and (3), respectively (Tadros, 2005):

$$W_c = 2\gamma_l \tag{2}$$

$$W_a = \gamma_l(1+\cos\theta) \tag{3}$$

where γ_l is liquid surface tension and θ is three-phase contact angle.

Equations (2) and (3) indicate that the work of adhesion W_a is always smaller than the work of cohesion of water W_c, suggesting that nanobubble generation will occur preferentially at the solid/water interface. Since hydrophobic particles have a greater contact angle θ, they have a smaller value of W_a, indicating that hydrophobic particle surfaces are the more favorable sites for cavitation to take place. Therefore, the generation of nanobubbles by hydrodynamic cavitation is fundamentally a selective process, which should have a positive effect on flotation efficiency.

2.1.2. Size Distribution

Nanobubbles normally refer to nanoscopic-sized bubbles smaller than 1 μm as shown in Figure 2-1 (Fan et al., 2010a). Figure 2-1 shows that the nanobubbles generated by a cavitation tube are about two orders of magnitude smaller than microbubbles produced by a static mixer. Frother F507 produces smaller nanobubbles than frother MIBC. This is because the surface tension reduction by F507 is more significant than by MIBC.

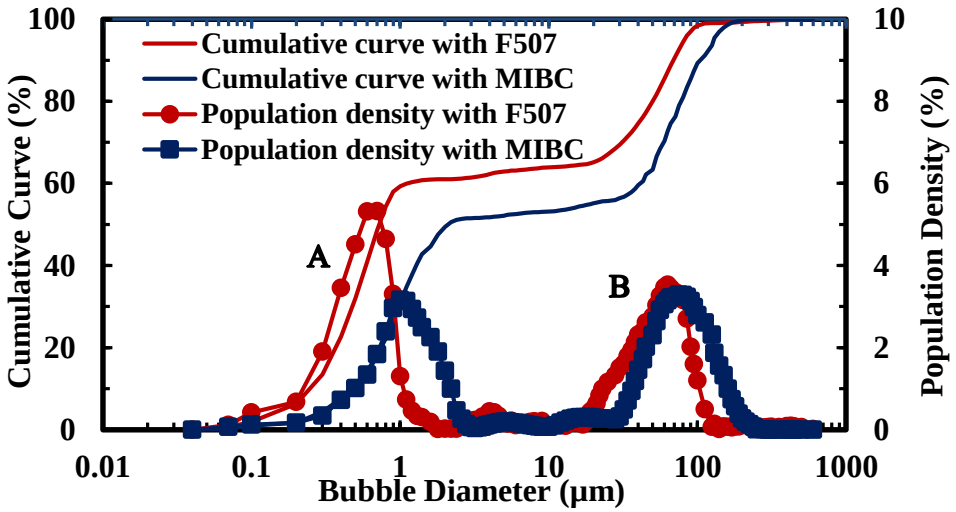

Figure 2-1. The size distribution curve for bubbles generated by static mixer (A) and cavitation tube (B) in water solution with 10 ppm MIBC and F507 (Fan et al., 2010a).

Ushikubo et al. (2010) employed a green badge (532 nm laser) Zetasizer Nano ZS particle size analyzer (ZEN3500, Sysmex Co., Japan), which detects Brownian motion of bubbles through dynamic light scattering (DLS), to measure the size distribution of the oxygen nanobubbles generated by a nozzle after mixing water with gas at a high pressure in a pressurized sump and the results are shown in Figure 2-2. The geometric mean of the nanobubble size was 137 nm

Figure 2-3 shows nanobubbles with a mean bubble diameter of 360-720 nm generated from Shirasu-porous-glass (SPG) membranes with a mean pore diameter of 43-85 nm

(Kukizaki and Goto, 2006). The nanobubble size was measured using a laser diffraction particle size analyzer (Kukizaki and Goto, 2006).

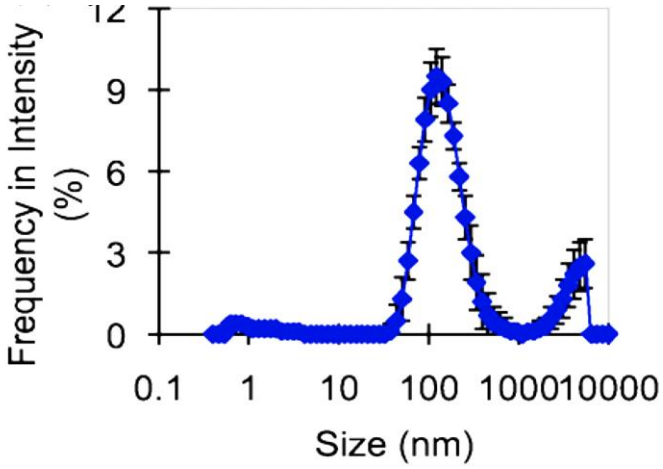

Figure 2-2. Oxygen nanobubble size distribution generated by a nozzle after stopping the gas introduction. The vertical bars represent the standard deviation of the replication data (Ushikubo et al., 2010).

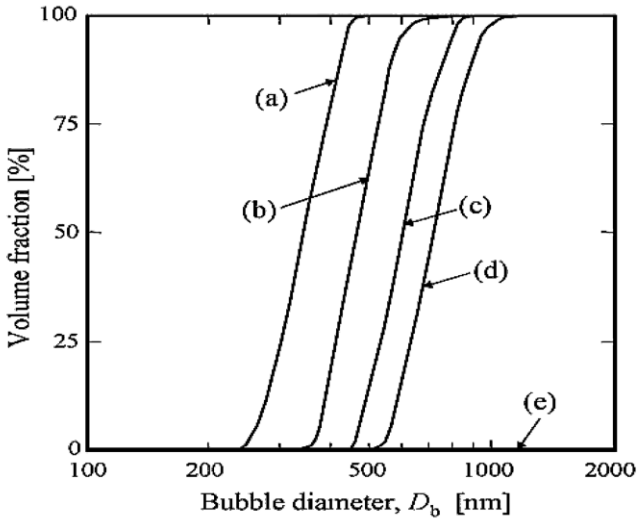

Figure 2-3. Cumulative size distribution of nanobubbles generated by (SPG) membranes with mean pore diameters of (a) 43 nm, (b) 55 nm, (c) 64 nm, (d) 85 nm. The flow velocity and concentration of sodium dodecyl sulfate were 0.7 m/s and 0.3 wt.%, respectively (Kukizaki and Goto, 2006).

2.1.3. Stability

Recent AFM studies have confirmed that nanobubbles are stable and can exist on a hydrophobic surface for several hours without discernible changes as shown in Figure 2-4 (Borkent et al., 2010) although the conventional Laplace equation suggests that the capillary pressure of a nanobubble is too great for the nanobubble to be stable. This is partly because nanoscopic contact angle is much larger than the macroscopic contact angle and the radius of curvature is large because the apparent radius of the nanobubble is usually larger than two times its height on hydrophobic surface (Borkent et al., 2010). Nanoscopic contact angle of nanobubbles with a hydrophobic surface is typically larger than 100^{o} as shown in Figure 2-4 and Figure 2-5 (Borkent et al., 2010 and Johnson et al., 2012). The nanoscopic contact angle is more than twice the measured macroscopic contact angle of a water droplet deposited on the same surface (Borkent et al., 2010).

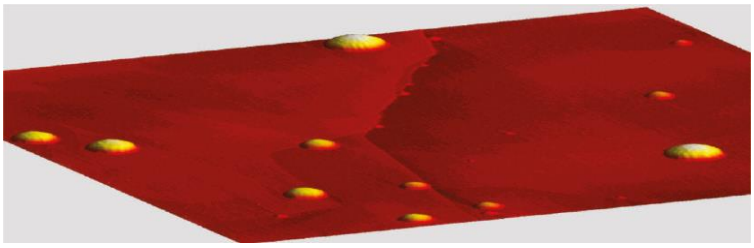

Figure 2-4. AFM image of surface nanobubbles on a hydrophobic surface inside a large water droplet. The image is 2000 x 2000 x 40 nm^3 (Borkent et al., 2010).

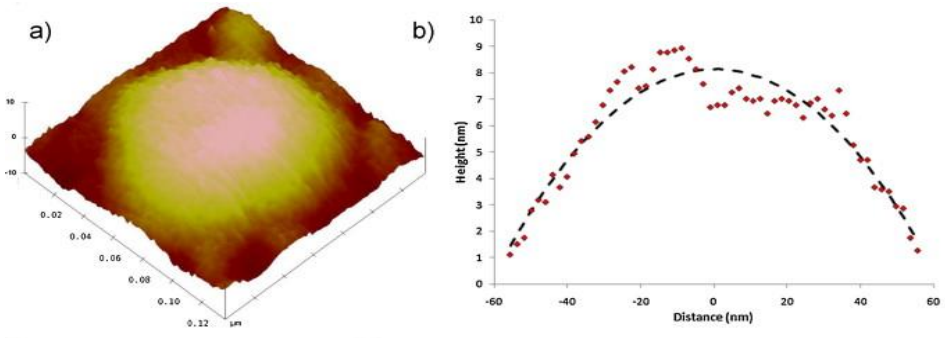

Figure 2-5. AFM image of a nanobubble that exists on a hydrophobic surface with a contact angle larger than 100^{o} (Johnson et al., 2012).

Nanobubbles also are very stable in liquid and can maintain their size without significant change as shown in Figure 2-6 and Figure 2-7. Figure 2-6 shows that the effective diameter can be maintained at 750 nm within 1 hour (Cho et al., 2005). Figure 2-7 shows that the geometric mean of nanobubbles generated in water by a nozzle was 137 nm after stopping the generation of the nanobubbles. The diameter increased slightly to 272 nm after several days (Ushikubo et al., 2010).

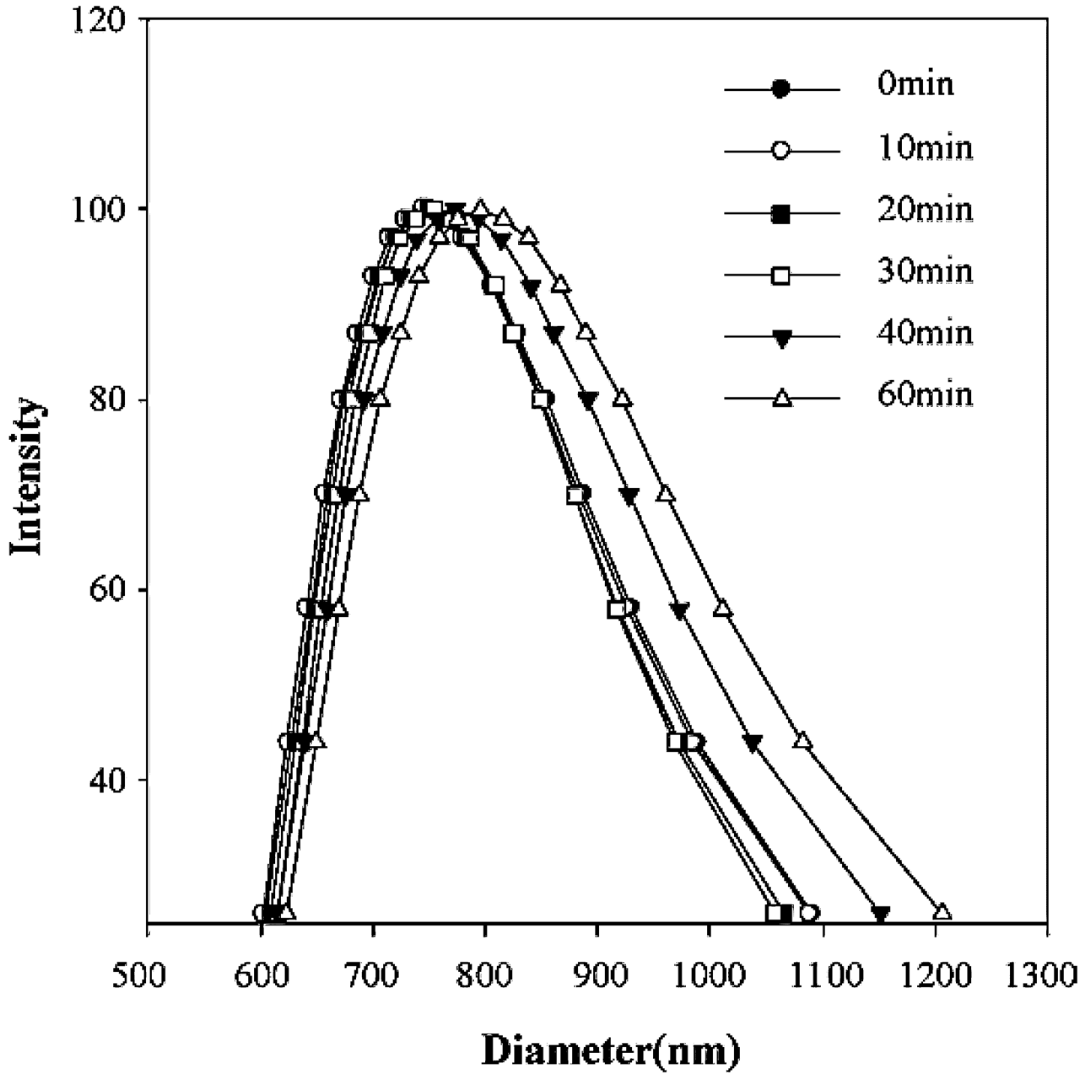

Figure 2-6. Nanobubble size distribution prepared by ultrasound in pure water (Cho et al., 2005).

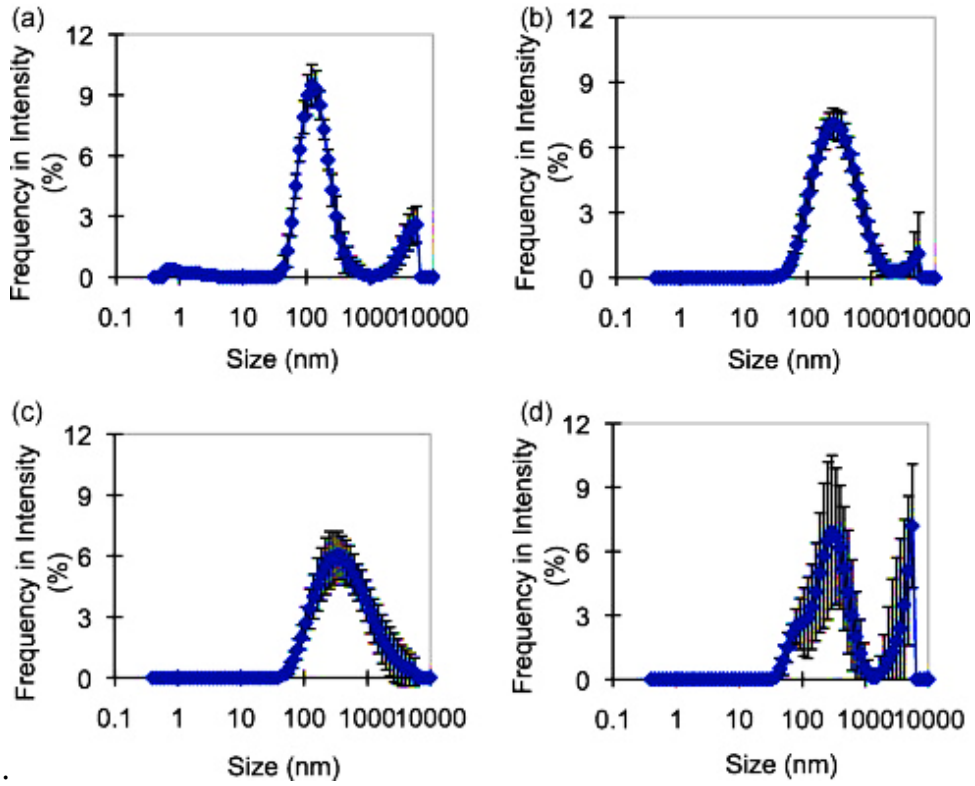

Figure 2-7. Oxygen nanobubble size distribution generated by a nozzle (a) after stopping the gas introduction, (b) 1 day, (c) 3 days and (d) 6 days. The vertical bars represent the standard deviation of the replication data (Ushikubo et al., 2010).

2.2. EFFECT OF NANOBUBBLES ON FROTH FLOTATION

Froth flotation is a particle separation process that exploits the difference in surface hydrophobicity of different particles. Fundamental froth flotation principles are basically the same for all flotation machines. However there are differences in the design depending on the operational restrictions and the requirements for a given mineral.

The recovery in flotation starts with the collision and adhesion of hydrophobic particles to the air bubbles followed by transportation of the hydrophobic particle-bubble

aggregate from the collection zone to the froth zone, drainage and enrichment of the froth, and finally by its overflow removal from the cell top, whereas hydrophilic particles remain in the pulp and are discharged as tailings. The success of effective particle separation by froth flotation relies on the efficient capture of hydrophobic particles by air bubbles in three steps, i.e. collision, attachment and detachment.

2.2.1. Probability of Collision

The probability of collision (P_c) between a particle and a bubble is defined as the fraction of particles of the same size and density in the path of the rising bubble that actually colloid with it. It can be calculated from stream functions for quiescent conditions (Weber and Paddock, 1983; Yoon and Luttrell, 1989) and microturbulence models for well mixed conditions (Schubert and Bischofberger, 1979; Yoon, 2000). One of the mathematical models for P_c is shown in Equation (4) (Yoon and Luttrell, 1989; Yoon, 1993):

$$P_c = \left[\frac{3}{2} + \frac{4\,\mathrm{Re}^{0.72}}{15}\right]\left(\frac{D_p}{D_b}\right)^2 \tag{4}$$

where D_b is the bubble size, D_p is the particle size and Re is the Reynolds number of the bubble.

When a bubble of radius R_b is rising in a slurry as shown in Figure 2-8, streamlines are generated by movement of the liquid around the bubble surface. The streamlines are characterized by a limiting radius R_c which is measured at infinite distance from the bubble surface. The particles within the limiting area of radius (R_c) and limiting polar position of ϕ_c have the chance to colloid with the rising bubble. On the other hand, the particles outside the limiting area follow the streamlines around the bubble surface without touching the bubble. A particle with sufficient size and/or density may penetrate the streamlines and colloids with the bubble.

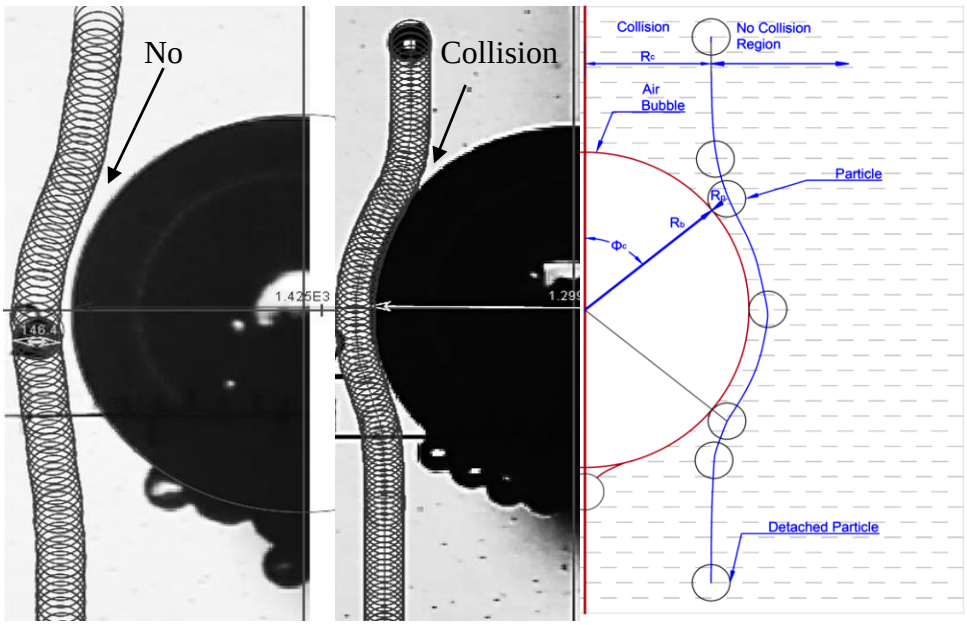

Figure 2-8. Particle-bubble collision in a liquid medium.

Figure 2-9 and Figure 2-10 show the simulation results from Equation (4) by assuming that water density ρ_w =1000 kg/m^3, gas density ρ_g =1290 kg/m^3, particle diameter D_p =1200 µm, gravitational acceleration g = 9.81 m/s^2, fluid viscosity μ_w = 0.001 kg.s/m. , and Re_b was estimated by using the gas slip velocity equations $u_b = \dfrac{g d_b^2 \left(\rho_w - \rho_g\right)}{18\mu_l \left(1 + 0.15\,\mathrm{Re}_b^{0.687}\right)}$ and $u_b = \dfrac{\mathrm{Re}_b\,\mu_l}{D_b \rho_w}$. The results indicate that P_c increases with increasing particle size and decreasing bubble size. Fine particles have a low probability of collision with bubbles and are thus difficult to catch by bubbles, particularly by large size bubbles. This is the main reason for low flotation rate of fine particles. Figure 2-10 shows that the collision probability of the fine particles can be enhanced by reducing the bubble diameter.

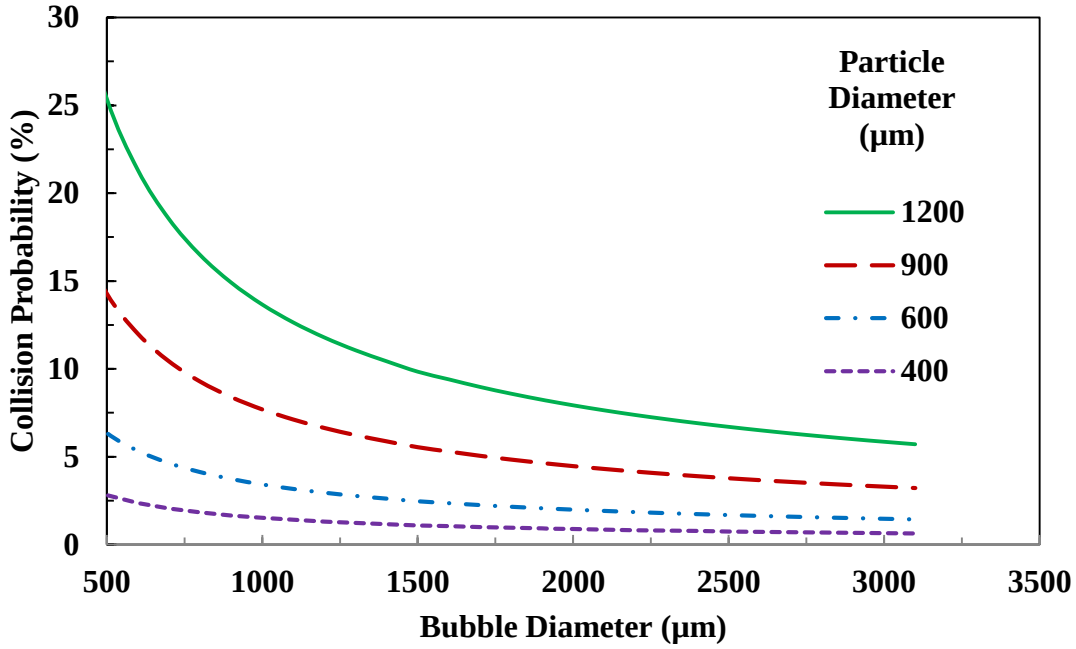

Figure 2-9. Bubble-particle collision probability of 400, 600, 900 and 1200 micron coal particle diameter as a function of bubble diameter: Water density ρ_w =1000 kg/m^3, gas density ρ_g =1290 kg/m^3, particle diameter D_p =1200 µm, gravitational acceleration g = 9.81 m/s^2, fluid viscosity μ_w = 0.001 kg.s/m.

Atomic force microscopy (AFM) images show that the coalescence of nanobubbles as hydrophobic surfaces approach forms a gaseous capillary bridges, and thus a capillary force as illustrated in Figure 2-11 (Hampton and Nguyen, 2010). The resulting concave capillary bridge produces an attractive force that forces the two surfaces into contact.

Nanobubble coated surfaces of very fine particles can lead to particle aggregation and more easily recovered due to an increased collision probability as illustrated in Figure 2-12. Thus nanobubbles increase the lower particle size flotation limitation by increasing the particle size of the fine and ultra-fine particles.

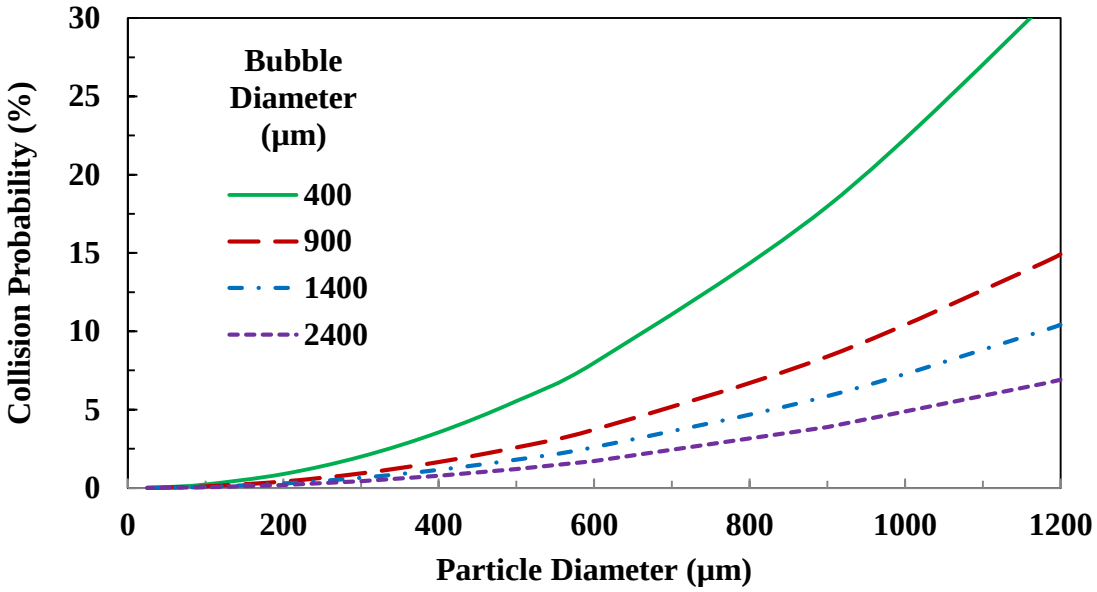

Figure 2-10. Bubble-particle collision probability of 500, 1000, 1500 and 2500 micron bubble diameter as a function of particle diameter: Water density ρ_w =1000 kg/m^3, gas density ρ_g =1290 kg/m^3, particle diameter D_p =1200 µm, gravitational acceleration g = 9.81 m/s^2, fluid viscosity μ_w = 0.001 kg.s/m.

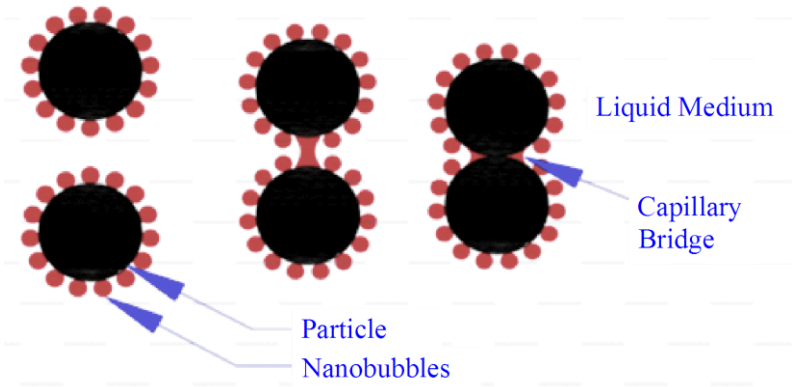

Figure 2-11. Coalescence of nanobubbles as hydrophobic surfaces approach forms a gaseous capillary bridge, and thus a capillary attractive force (Hampton and Nguyen, 2010, Schubert, 2005)

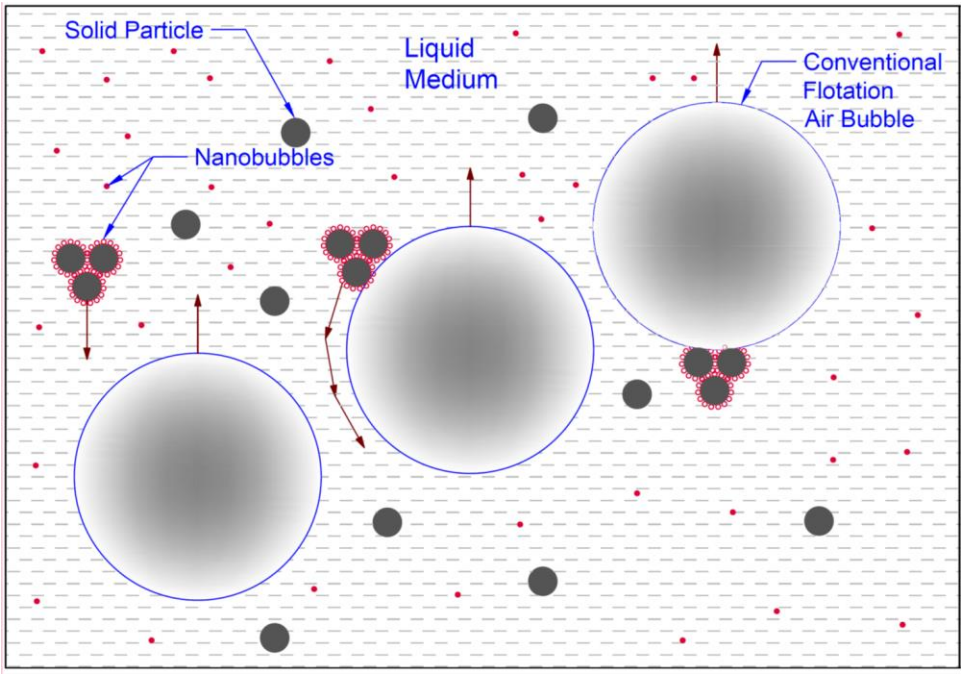

Figure 2-12. Illustration of nanobubble coated surface of very fine particles and increased collision probability

2.2.2. Probability of Attachment

After collision at polar position of ϕ_{cr}, the steps required for particle inside limiting cross section area of radius (R_{cr}) to become attached as illustrated in Figure 2-13 are (Albijanic et al., 2010):

- Thinning of the intervening liquid film to a critical film thickness (h_{cr});
- Rupture of the intervening liquid film and formation of three-phase contact of some critical wetting radius (r_{cr});
- Expansion of the tpc line to form a stable wetting perimeter with certain penetration depth (d) depending on the particle hydrophobicity.

The time of thinning and rupturing of wetting thin films is referred to as the induction time (t_i), whereas the time of the attachment including the three steps is called the attachment time (t_{at}). Under normal conditions, the rupture time (t_r) is not considered which is significantly shorter than both the induction time (t_i) and the time required the three-phase contact line to expand to establish a stable wetting perimeter (t_{tpc}). These four different time scales are described in Equation (5) (Albijanic et al., 2010).

$$t_{at} = t_i + t_r + t_{tpc} \tag{5}$$

All the available predictions of the particle-bubble attachment in the literature are simplified by neglecting the last two time scales (Nguyen, Schulze and Ralston, 1997). The successful attachment occurs only when the induction time (t_i) is less than the sliding time (t_s) which is the time for the particle to slide on the bubble surface.

The probability of attachment (P_a) is related to the energy barrier for the bubble-particle adhesion E_i and the kinetic energy of collision E_k as shown in Equation (6) (Yoon and Luttrell, 1989; Mao and Yoon, 1997):

$$P_a = \exp\left(-\frac{E_i}{E_k}\right) \tag{6}$$

P_a can be calculated using Equation (7) (Yoon, 2000):

$$P_a = \sin^2\left[2\arctan\exp\left(-\frac{(45+8\,\mathrm{Re}^{0.72})u_b t_i}{15D_b\left(\frac{D_b}{D_p}+1\right)}\right)\right] \tag{7}$$

Equation (7) indicates that P_a decreases with increasing D_p, suggesting that coarse particles are more difficult to attach to air bubbles. P_a increases with increasing particle hydrophobicity or decreasing induction time t_i; P_a also increases with decreasing bubble rising velocity U_b and decreasing bubble size D_b, meaning smaller bubble size is favorable for increasing probability of attachment (Ralston and Dukhin, 1999; Yoon 2000).

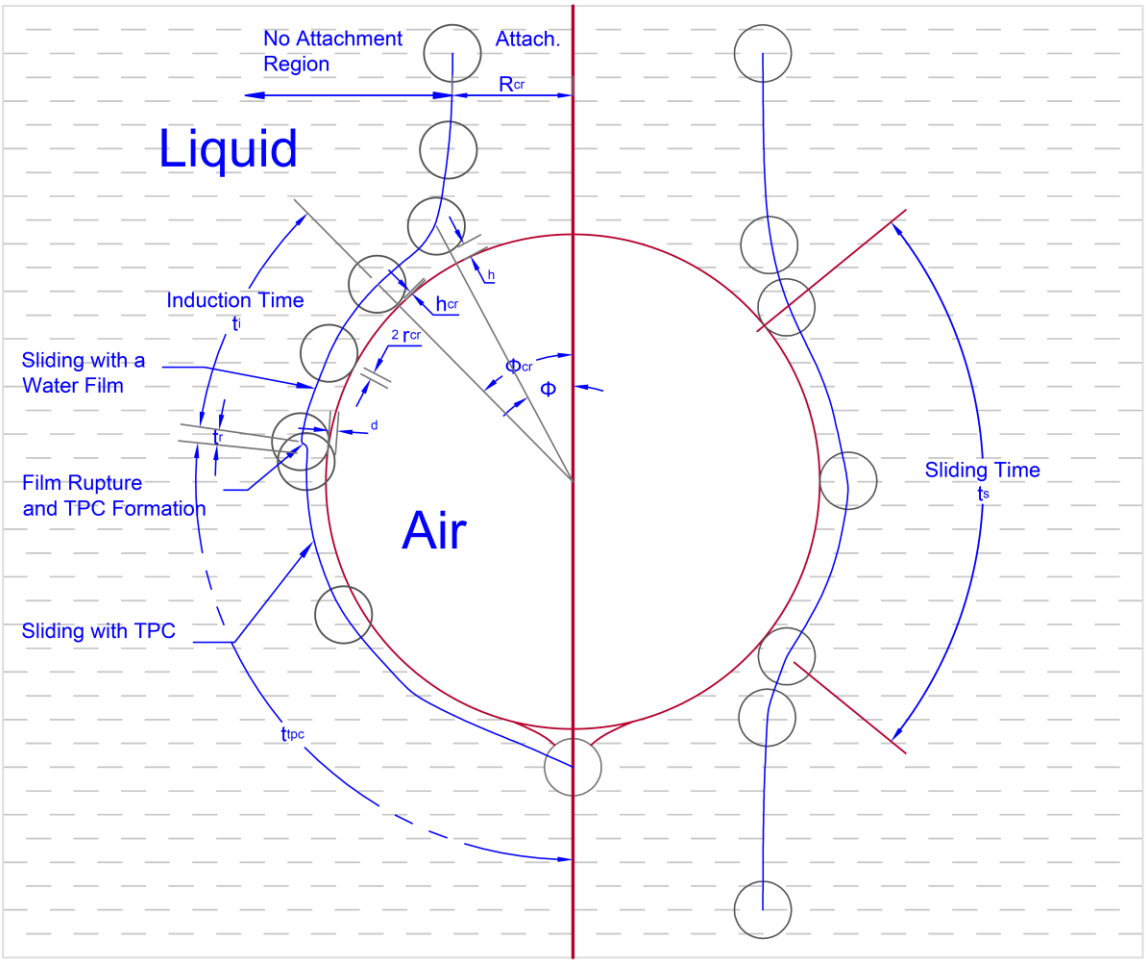

Figure 2-13. Illustration of particle-bubble attachment in a liquid medium (Albijanic et al., 2010; Nguyen, Ralston and Schulze, 1998).

Yoon and Luttrell (1989) showed that P_a increases with decreasing induction time t_i and decreasing particle size D_p; P_a also increases with decreasing bubble size until the bubble size becomes too small because the sliding distance becomes very small and thus the sliding time is smaller than induction time. Using a higher dosage of collector improves hydrophobicity and thus increases P_a but flotation operation cost increases and sometimes the selectivity and separation efficiency decrease. A better approach is to generate nanobubbles on solid surface to increase its hydrophobicity.

Stockelhuber et al. (2004); Simonsen, Hansen, and Klosgen (2004) found that nanobubbles can cause the rupture of the wetting films between mineral particles and conventional-sized bubble which is a basic step in the flotation process. In the process of drainage of the wetting film, the largest nanobubble is almost as thick as the wetting film.

Nanobubbles play no roles in rupture process as shown in Figure 2-14 when the thickness of thick film is greater than the height of bubbles. As the film thickness is close to the bubble height, the surface forces begin to act between the biggest nanobubble and film surface (Figure 2-15). It is noticed in Figure 2-15 that the rupture always happens at the biggest nanobubble, because the thinnest place is the weakest place to break at the same interaction force (Stockelhuber et al., 2004).

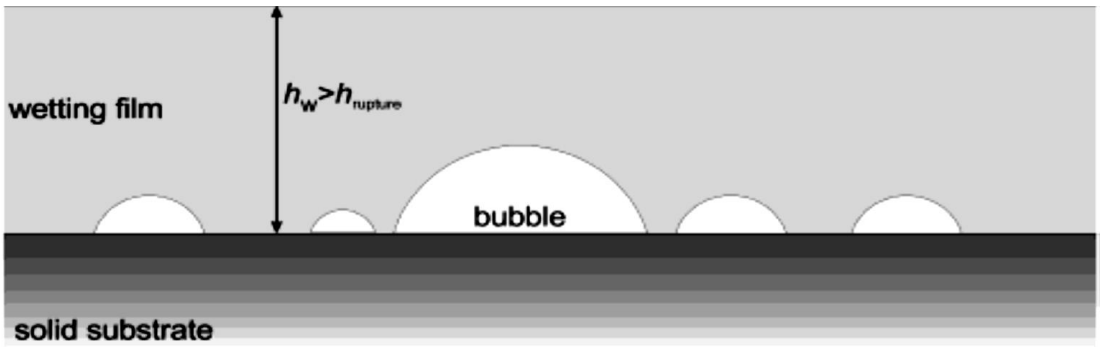

Figure 2-14. AFM image: Wetting film with gas bubbles adhered to the solid substrate. For a large film thickness h_w, where no rupture occurs, nanobubbles play no role in film behavior (Stockelhuber et al., 2004).

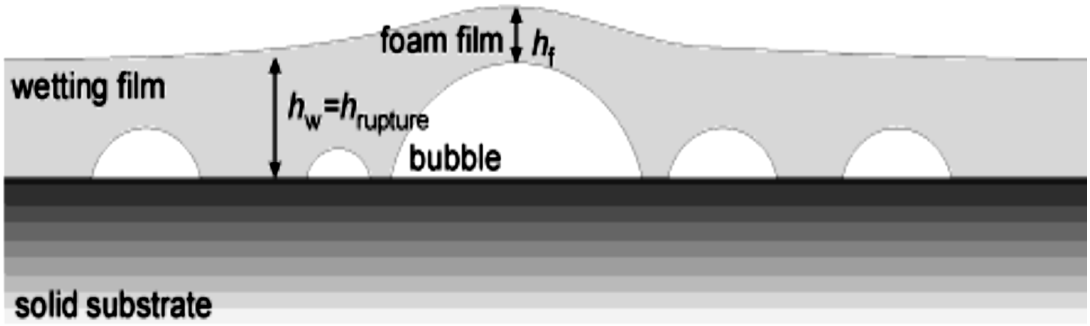

Figure 2-15. AFM image: Beginning of interaction between nanobubble and the surface of the wetting film. Film rupture occurs at a film thickness on the order of the biggest bubble height ($h_w = h_{rupture}$) (Stockelhuber et al., 2004).

2.2.3. Probability of Detachment

After collision and attachment, not all particles attached to air bubbles report to the froth phase. A portion detach from bubble surface and drop back into the pulp phase. Probability of detachment P_d is related to the energy barrier for the bubble-particle detachment $E_i^{'}$, work of adhesion between bubble and particle W_a and kinetic energy of collision E_k in Equation (8) (Mao and Yoon, 1997):

$$P_d = \exp\left(-\frac{E_i^{'} + W_a}{E_k}\right) \tag{8}$$

Particle detachment occurs when detachment forces exceed the maximum adhesive forces. P_d can be calculated using Equation (9) (Tao, 2004):

$$P_d = \left[1 + \left(\frac{3(1-\cos\theta_d)\gamma}{g\left(\rho_b - \rho_w\left(\frac{1}{2} + \frac{3}{4}\cos\frac{\theta_d}{2}\right)\right)}\right)\left(\frac{1+\frac{D_p}{D_b}}{D_p^2}\right)\right]^{-1} \tag{9}$$

Equation (8) shows that P_d increases with increasing particle size D_p and increasing bubble size D_b. Therefore, coarse heavy and less hydrophobic particles are more likely to detach from large air bubbles and use of small bubbles will increase the flotation recovery of coarse particles as shown in Figure 2-16 and Figure 2-17. Assuming ρ_w =1000 kg/m^3, ρ_p =1350 kg/m^3 (coal) and 2650 (ash), θ_d =60^o (coal) and 10^o (ash), D_p =1200 µm, g = 9.81 m/s^2, γ = 0.0728 N/m^3, the effects of bubble size and particle size on the particle detachment probability determined from Equation (9) for coal and ash particles can be simulated as shown in Figure 2-16 and Figure 2-17.

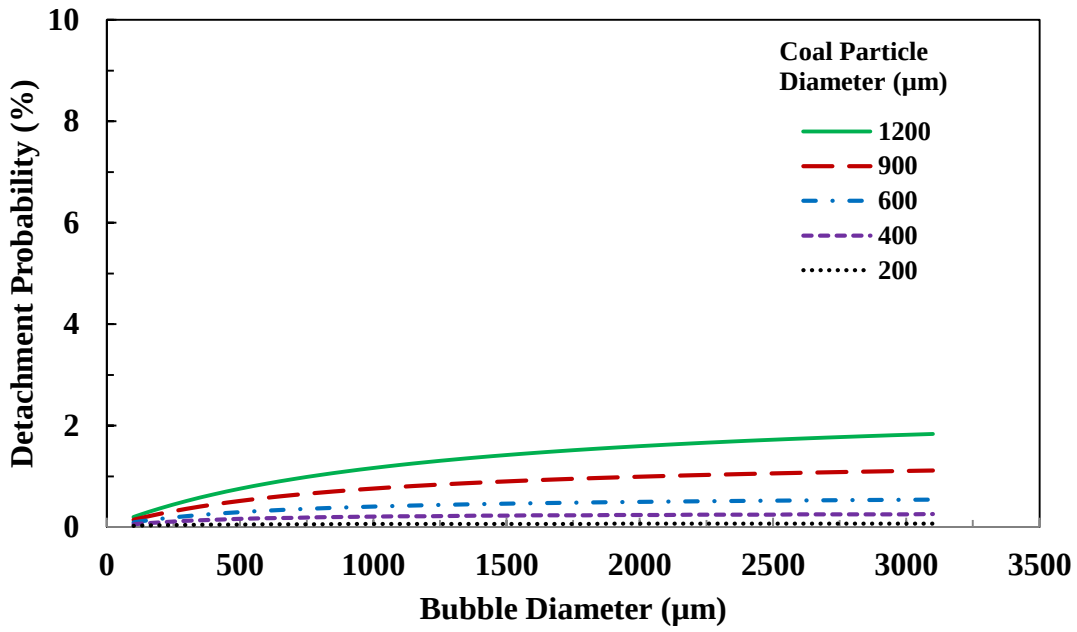

Figure 2-16. Effect of bubble size and particle size on coal particle detachment probability: ρ_w =1000 kg/m^3, ρ_p =1350 kg/m^3 (coal), θ_d =60^o (coal), D_p =1200 µm, g = 9.81 m/s^2, γ = 0.0728 N/m^3.

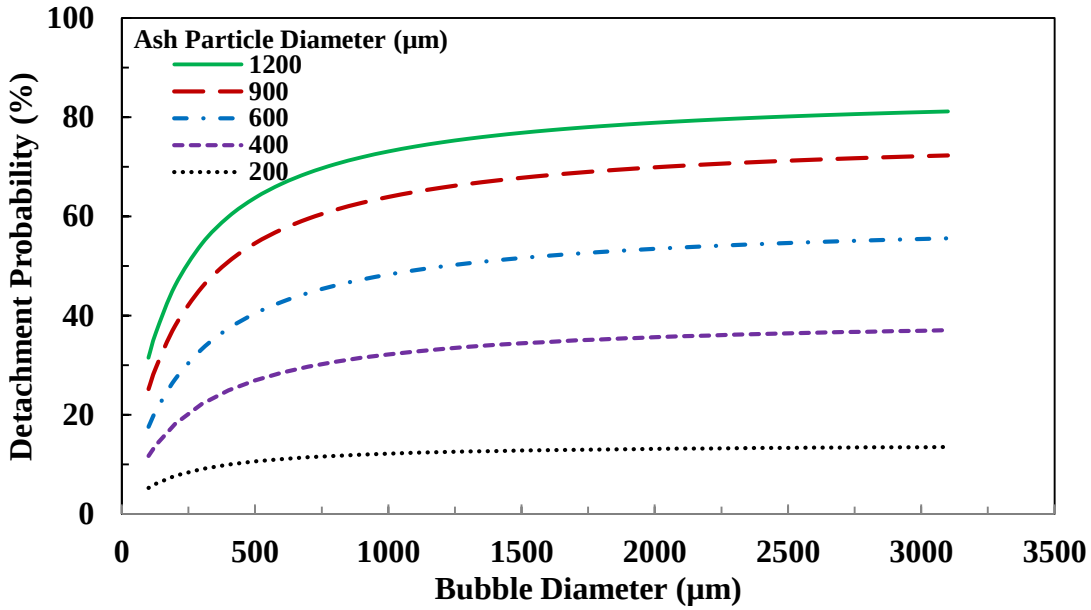

Figure 2-17. Effect of bubble size and particle size on ash particle detachment probability: ρ_w=1000 kg/m^3, ρ_p=2650 kg/m^3 (ash), θ_d=10^o (ash), D_p =1200 μm, g = 9.81 m/s^2, γ = 0.0728 N/m^3

2.2.4. Flotation Particle Size Limits

A high froth flotation efficiency is limited to the narrow particle size range between 50 μm and 600 μm for coal as shown in Figure 2-18 (Jowett, 1980). The coarser the coal the harder it is to stay attached to the air bubble. A finer coal size will lead to a poor particle-air bubble collision.

Nanobubble coated fine particles will lead to particle aggregation and are thus more easily recovered due to an increased collision probability. In addition, nanobubbles can increase the particle hydrophobicity (Fan et al., 2010a; Fan, Zhao and Tao, 2012), and thus increase the bubble-particle attachment probability and decrease the detachment probability. Furthermore, nanobubbles expand the froth flotation particle size limit by enhancing the recovery of fine and relatively coarse particles as a result of increased

probabilities of particle-bubble collision and attachment and reduced probability of detachment (Fan et al., 2010b).

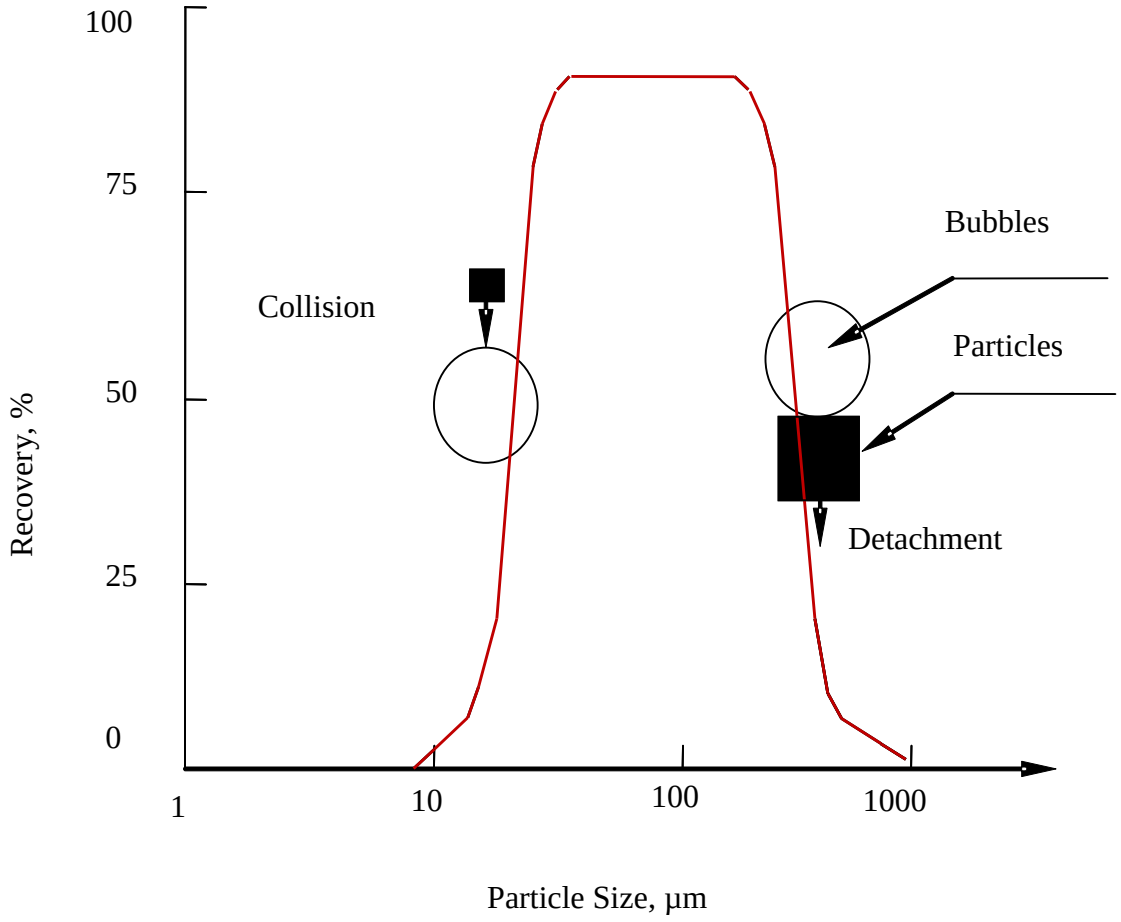

Figure 2-18. Froth flotation particle size limitations (Jowett, 1980)

The improvement by nanobubbles on the hard-to-float particles was more significant than that on the easy-to-float particles, especially at lower collector dosages (Fan et al., 2010c). Tao (2004) found that nanobubbles can extend this size range to a lower limit of a few microns, even submicrons, and an upper limit of 1–2 mm, increasing the process efficiency for ultrafine and relatively coarse particles and expanding applications of flotation.

2.2.5. Froth Flotation Kinetics

The froth flotation performance is dependent on rate constant (k), retention time (τ), and cell mixing (Peclet number Pe).

The retention time (τ) is the time required for the coal particle to stay in the slurry before reporting to the product and it can be determined by the ratio of the active volume of the flotation cell and the feed flow rate to the cell.

Cell mixing (Pe) also affects flotation performance. The best performance can be obtained from a plug flow condition (column flotation) rather than a well-mixed condition (mechanical flotation).

The froth flotation rate constant (k) indicates how fast the coal reports to the concentrate. Equation 10 indicates that the flotation rate constant is dependent on particle hydrophobicity, particle size, solids content, feed rate, froth depth, reagent type, reagent dosage, gas flow rate and bubble diameter (bubble generators) (Kennedy, 2008). The froth flotation first order rate constant (k) is given by Equations (10) and (11) (Yoon et al. 1989; Gorain, Franzidis and Manlapig, 1995 and 1997; Yoon and Mao, 1996; Deglon, Sawyerr and O'Connor, 1999; Heiskanen, 2000):

$$k = \frac{3V_g}{2D_b} P_c P_a (1 - P_d) \tag{10}$$

$$k = \frac{1}{4} S_b P_c P_a (1 - P_d) \tag{11}$$

where V_g is the superficial gas velocity, P_c is the probability of collection, P_a is the probability of attachment, P_d is the probability of detachment, D_b is the bubble diameter and S_b is the bubble surface area flux.

Improved flotation rates have been reported when nanobubbles co-exist with conventional-sized flotation bubbles (Zhou et al., 1997). Two factors that contribute to the increased flotation rate constant are: a) the nanobubbles formed on hydrophobic particles may cause agglomeration by a bubble-bridging mechanism, resulting in increased collision probability with the bubbles; b) particles frosted with nanobubbles may present a surface favorable to attachment to conventional sized bubbles.

2.2.6. Froth Flotation Reagent Consumption

Several chemical reagents are used to enhance the froth flotation performance. Collector is essential in froth flotation to increase the differential flotation rate between different particles. The most common types of collectors for coal flotation are diesel fuel, kerosene and fuel oil.

The frother is required to create a froth capable of carrying the mineral to the float stream. The frother decreases the bubble size in the pulp by reducing the surface tension of water, thus increases the collision probability of the particles with the bubbles.

Many studies have confirmed that nanobubbles generated by hydrodynamic cavitation selectively on the hydrophobic particles change the surface characteristics of minerals (Hampton and Nguyen, 2010), increase the differential flotation rate, increase contact angle of solids, hence attachment force (Fan et al., 2010b; Fan, Zhao and Tao, 2012), bridge fine particles to form aggregates having higher collision and attachment probabilities, minimize slime coating, remove oxidation layers on particle surfaces, and in consequence reduce reagent consumption (Fan and Tao, 2008; Zhou et al., 1997).

2.2.7. Flotation Froth Phase

During flotation, the hydrophobic particles in the slurry are captured selectively by air bubbles and then carried to the top of the slurry zone where they form a froth layer. The froth is collected as it flows over the top of the vessel. Unlike the collection slurry phase, froth phase at the top has quite different behavior. As the bubbles rise, liquid drains back

continuously, decreasing liquid fraction and increasing bubble size with increasing the froth height. In a typical froth, the upper layer can be quite dry while the lower level is wet. If wash water is added, which is a commonly used procedure to reject gangue minerals, it wets the froth. The froth phase is therefore an important part of the flotation process as it further refines the concentrate produced and determines the final recovery.

Bubbles that may have been spherical in shape at the pulp–froth interface become highly distorted in the froth, appearing as polyhedral cells whose surfaces are formed by thin liquid films as shown in Figure 2-19. As the liquid films separating the bubbles become thinner, coalescence of the bubbles occurs. Upon coalescence, particles detach from the bubbles and drop back from the froth zone back into the pulp zone as a result of reduction in bubble surface area and lack of sufficient surface area, as shown in Figure 2-20.

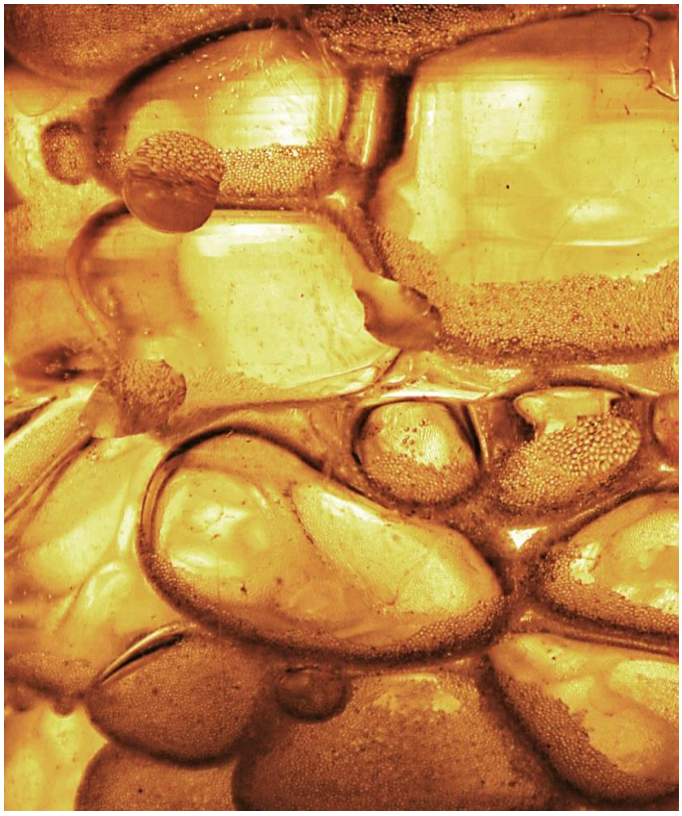

Figure 2-19. Bubbles appearing as polyhedral cells in column froth zone separated by liquid films.

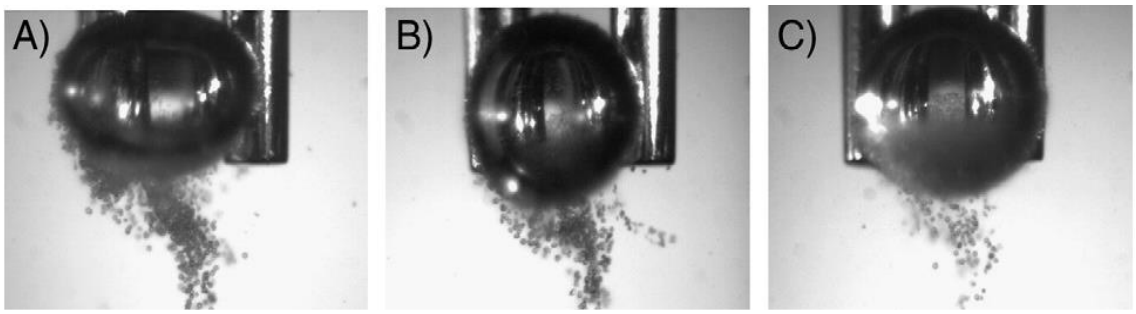

Figure 2-20. Images of detached particles following the coalescence of bubble pairs in various cetyl trimethyl ammonium bromide "CTAB" concentrations: (a) 2.74×10^{-5} M; (b) 5.49×10^{-4} M; (c) 1.65×10^{-3} M (Ata, 2009)

The froth stability is depending not only on the frother type and concentration but also on the particles, associated chemicals and nanobubbles in the froth flotation system. The maximum froth stability is attained when froth contains particles with moderate surface hydrophobicity which are capable of forming stable bridges across the foam film as shown in Figure 2-21A, increasing the rigidity of the froth structure (Johansson and Pugh, 1992; Aveyard et al., 1994; Dippenaar, 1982). Highly hydrophobic and/or irregular particles destabilize froth as a result of the thinning and rupturing of the inter-bubble liquid bridged by the particle (Figure 2-21B).

Furthermore, if the contact angle is less than a critical degree of wetting at which liquid film separating bubbles ruptures, a stable orientation will be attained and the life of the film will be prolonged. But in the case where the bridging particle has a contact angle more than the critical degree of wetting, the particle will easily dewet through both sides of the lamella, resulting in the film rupture. The critical degree of contact angle at which film failure occurs depends on particle size, shape, the number of particles and the separation distance between the particles in the film (Aveyard et al., 1994; Dippenaar, 1982).

In practice, froth destabilization is often caused by using an excessive amount of collector and this is generally reflected in froth dryness and immobility, the factors that significantly affect the mass flow rate of solids flowing over the cell lip (Ata, 2012). The

coalescence time (the time required for the two bubbles to merge) was found to increase with the bubble surface coverage and the bubbles appeared to have more resistance to coalescence at all surface coverage when both are loaded (Ata, 2012).

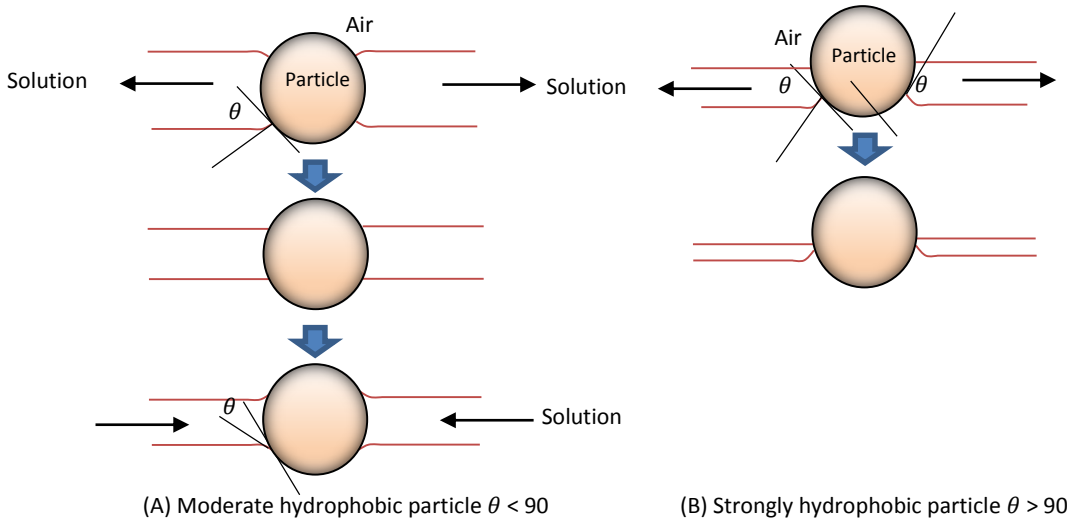

Figure 2-21. Bridging particle behavior in a foam (A) Moderately hydrophobic (B) highly hydrophobic particle (Aveyard et al., 1994).

Particles with low degree of hydrophobicity corresponding to a contact angle of less than 40^{o} were found to stream out into the lamella and did not contribute to the stability of the froth film (Dippenaar, 1982; Ata, Ahmed and Jameson, 2003). Particles with a strong level of floatability exhibit the highest flotation recovery probably as a result of particle reattachment in the froth. Thus, high bubble coalescence rate in the froth zone is not necessarily associated with low flotation recovery (Ata, Ahmed and Jameson, 2003). The entrained solids in the froth considerably reduce bubble coalescence, probably by increasing the slurry viscosity between the bubble films, reducing the drainage rate of liquid films, and possibly by mechanical blocking (Ata, Ahmed and Jameson, 2003). Selectivity and recovery of coarse particles decrease with increasing froth height. Transferring of particles from the collection zone to the froth zone in a flotation column decreases drastically with increasing particle size. Higher flotation recovery of coarse particles can be achieved by use of nanobubbles and high air holdup (Wiegel and

Lawver, 1986; Contini, Wilson and Dobby, 1988; Tao, 2004; Tao, Luttrell and Yoon, 2000). Furthermore, large bubbles deform and form a typical foam polyhedral structure while nanobubbles created via hydrodynamic cavitation can move freely in the froth films and in Gibbs Plateau borders, behaving as particle dispersions as shown in Figure 2-22 (Raut et al., 2012) to stabilize the froth zone.

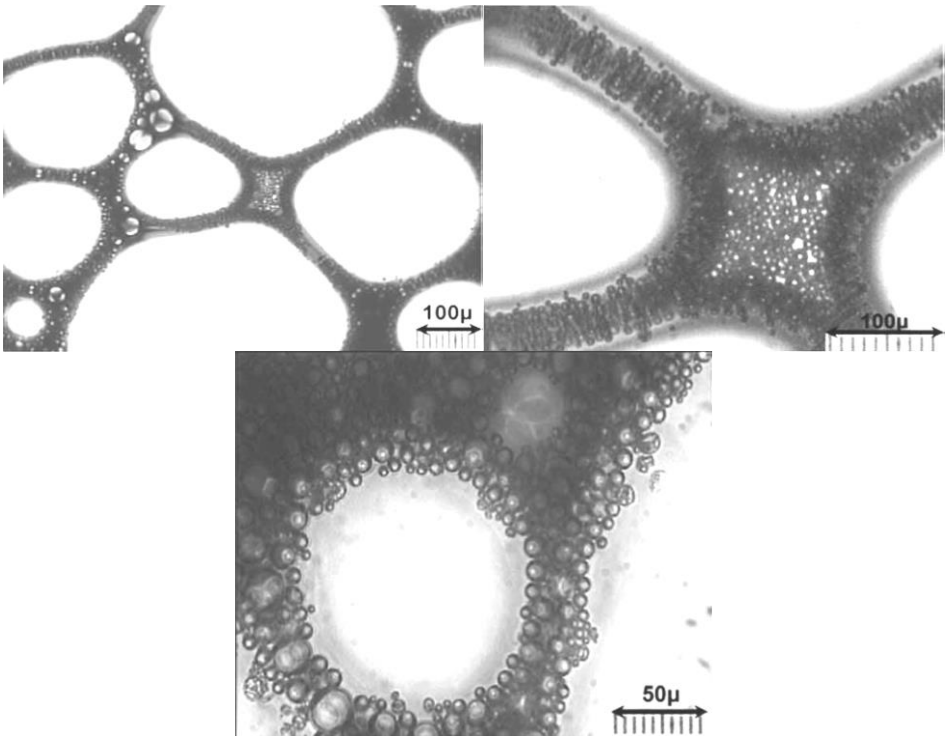

Figure 2-22. Images of co-existence of large (>100 mm) and small bubbles (<10 mm) in froth zone (Raut et al., 2012).

2.3. ATOMIC FORCE MICROSCOPY STUDIES OF NANOBUBBLES

2.3.1. Nanobubble at Solid-Liquid Interface

The formation, stability, density and shape of gaseous nanobubbles accumulated at the hydrophobic surface-liquid interface has been studied extensively by atomic force microscopy (AFM).

Changing the temperature is one of the important physical and chemical factors that have been linked to the generation process of nanobubbles at the solid-water interface. Increasing the temperature of water reduces the gas solubility and heat diffusion, which is larger than gas diffusion. Thus, water becomes oversaturated with air, and that favors the formation of the nanobubbles at the solid-water interface as shown in Figure 2-23 (Yang et al., 2007; Zhang et al., 2004). Yang et al (2007) and Zhang et al. (2004) found that when the temperature increased to 30 ^{o}C, the nanobubbles density increased very slowly and increased sharply when the temperature increased further. It is noticed that the nanobubbles do not disappear when the water cools down to ambient conditions and they are remarkably stable.

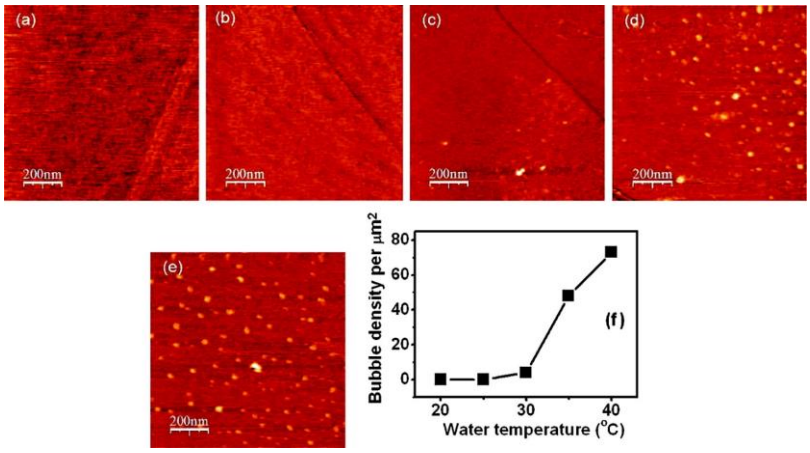

Figure 2-23. Tapping mode AFM topography images at diffrent water temperature in interval of 5 ^{o}C from 20 ^{o}C (a) to 40 ^{o}C (e). (f) the nanobubbles density as a function of water temperature (Yang et al., 2007).

Alcohol-water exchange is another method to generate the nanobubbles at the solid-liquid interface. In pure alcohol, there are hardly any nanobubbles formed at the solid-liquid interface as a result of the high solubility of the air in the alcohol. However, flushing away the alcohol with water increased sharply the density of the nanobubbles as shown in Figure 2-24 and Figure 2-25. The formation of the nanobubbles is stimulated when the substrate is first immersed in alcohol which is then flushed away by water (Zang, Maeda and Craig, 2006; Zhang et al., 2004; Agrawal and Mckinley, 2006; Yang et al., 2007). In

terms of nanobubble density, ethanol gives better results than propanol as a result of the large gas solubility in the ethanol more than the propanol. Also, the higher exothermic mixing of the ethanol and water increase the liquid temperature which increases the nanobubble density (Yang et al., 2007).

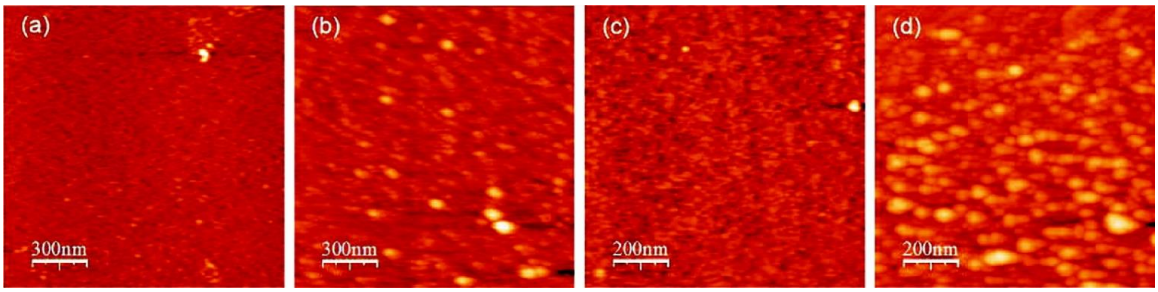

Figure 2-24. Tapping mode AFM topography images substrate immersed in (a) propanol, (b) water after propanol, (c) ethanol, (d) water after ethanol (Yang et al., 2007).

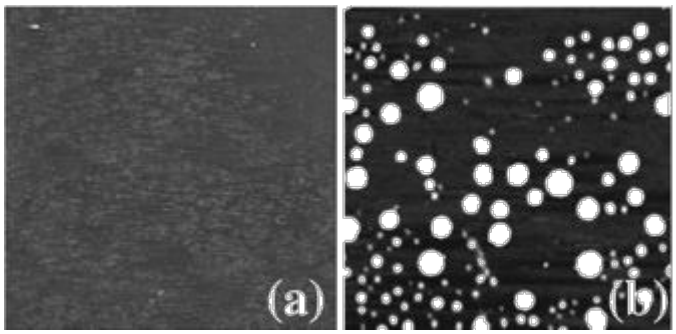

Figure 2-25. Tapping mode AFM topography images of the hydrophobic surface in water before (a) and after (b) ethanol-water exchange (Zhang et al., 2006a).

Water electrolysis can be used as an alternative method to generate surface nanobubbles (Zhang et al., 2006b; Yang et al., 2009). Hydrogen (oxygen) nanobubbles are produced at hydrophobic surface-water interface when the surface acts as a negative (positive) electrode. The formation, growth and size of the nanobubbles can be controlled by tuning either the applied voltage or the reaction time (Zhang et al., 2006b). Figure 2-26 shows that the hydrogen nanobubbles produce at the solid-water interface with varying density

at different voltage when the solid surface is the cathode. The nanobubbles formation increases significantly with increasing the voltage from 1.5 to 2 V. Figure 2-26e confirms that the nanobubbles remain stable even when the voltage has been turned off from 2.5 V. At a higher voltage the nanobubbles covers the whole surface with larger individual size (Figure 2-26f-h) (Yang et al., 2009).

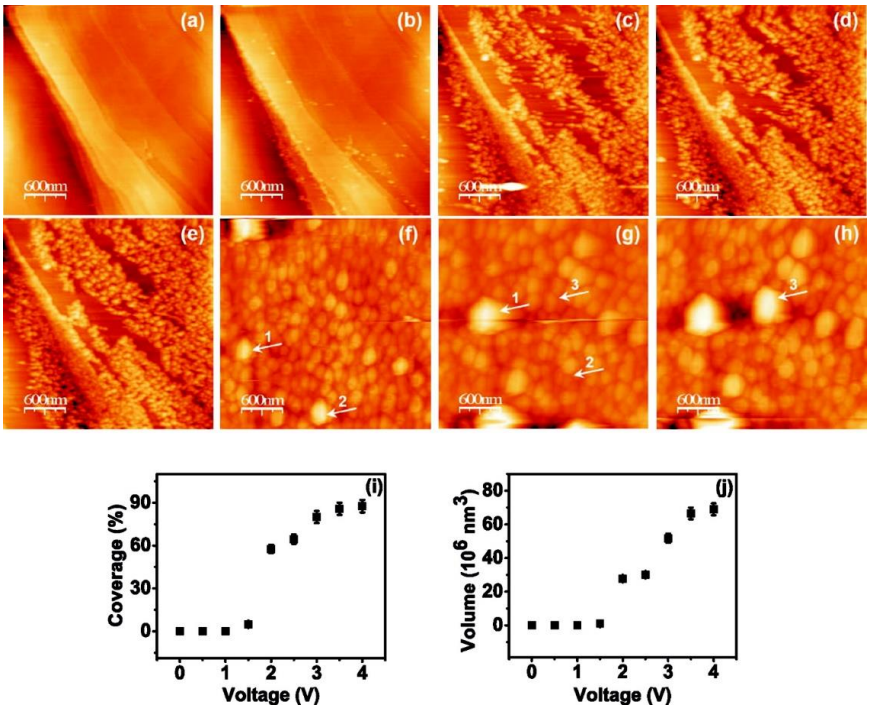

Figure 2-26. Tapping mode AFM topography images of the hydrophobic surface as the cathode at different voltages: (a) 1 V, (b) 1.5 V, (c) 2, (d) 2.5 V, (e) 0 V, (f) 3 V, (g) 3.5, (h) 4 V. Nanobubble height range: (a,b) 42 nm, (c-e) 50.6 nm, (g,h) 115.5 nm (Yang et al., 2009).

Figure 2-27 shows that the oxygen nanobubbles produced at the solid-water interface with varying density at different voltage when the solid surface is the anode. It was noticed that the numbers of oxygen nanobubbles produced (Figure 2-27) is much smaller than the that of hydrogen nanobubbles (Figure 2-26) which is due to the solubility of the oxygen in water is approximately two times the solubility of the hydrogen as well as the production rate during the electrolysis process, H_2:O_2 = 2:1.

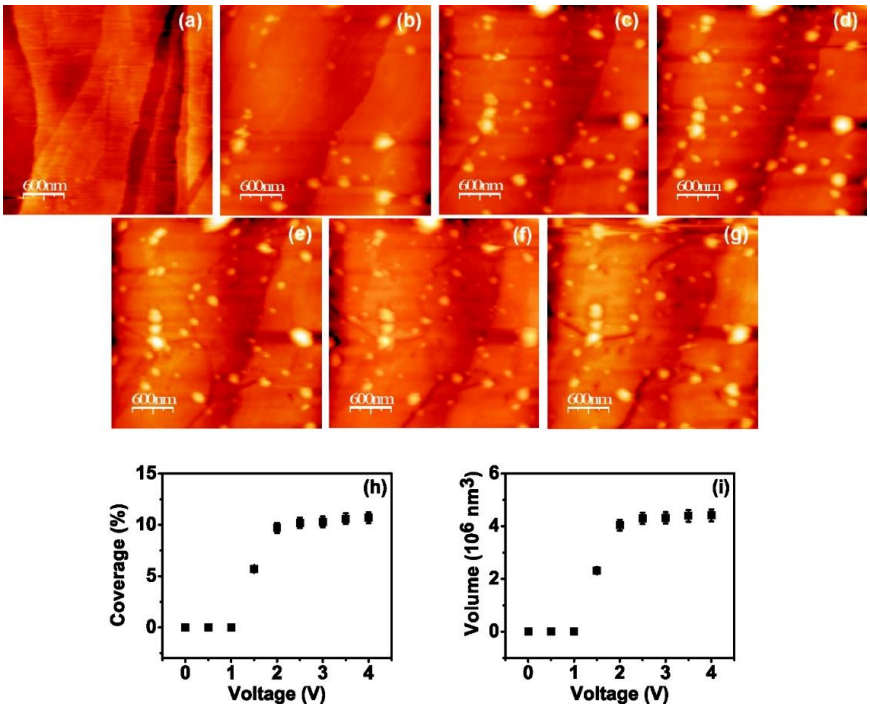

Figure 2-27. Tapping mode AFM topography images of the hydrophobic surface as the anode at different voltages: (a) 1 V, (b) 1.5 V, (c) 2, (d) 2.5 V, (e) 3 V, (f) 3.5 V, (g) 4. Nanobubble height range: (a) 12 nm, (b-e) 35 nm (Yang et al., 2009).

The nanobubbles are nanoscopic in height with a large radius of curvature, which creates a very large nanoscopic contact angle (Figure 2-28). The nanoscopic contact angle is defined as the angle subtended by the liquid phase at the solid surface adjacent to the nanobubble. The nanoscopic contact angle is more than twice the measured macroscopic contact angle of a water droplet deposited on the same surface as illustrated in Figure 2-29 (Borkent et al., 2010, Walczyk, Schon and Schonherr, 2013). The three-phase line of the nanobubbles is usually circular but some irregular shaped (non-circular) has been reported as a result of the types of the hydrophobic surfaces such as octadecyltrichlorosilane (OTS) silicon and highly ordered pyrolytic graphite (HOPG) (Zhang et al., 2006a).

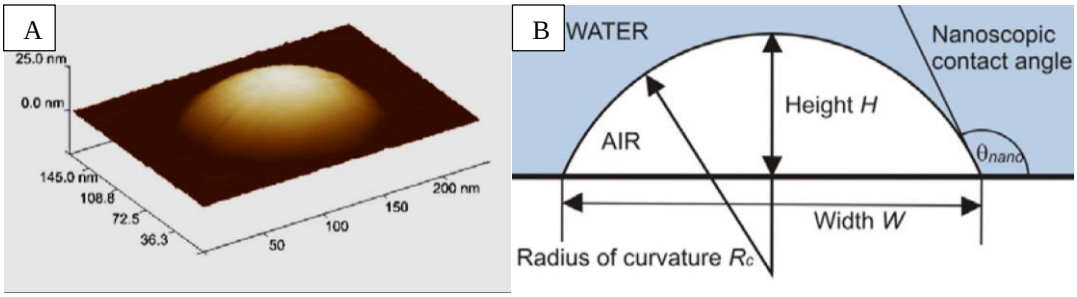

Figure 2-28. AFM image of a nanobubble (A) with a schematic cross-section (B) (Walczyk, Schon and Schonherr, 2013)

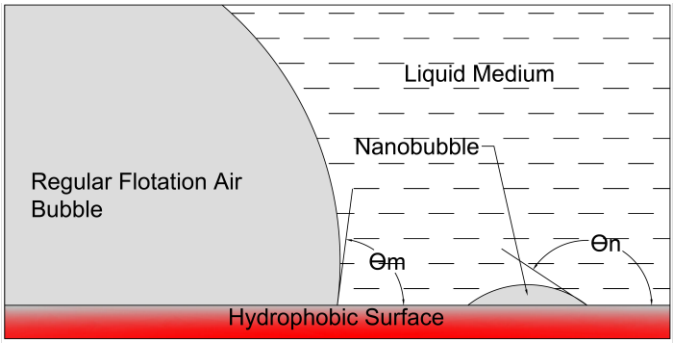

Figure 2-29. Illustration of the difference between the nanoscopic contact angle and macroscopic contact angle (Zhang et al., 2006a).

2.3.2. Nanobubble Effect on Hydrophobic Solid Surfaces Interaction

The interaction between the hydrophobic surfaces has long fascinated many researchers. Many studies for several years have failed to successfully explain and clarify the origin of the strong interaction, which depends on the hydrophobic surfaces employed to measure the force (Ishida, Kusaka and Ushijima, 2012). It is recently clear that in many cases the hydrophobic attractive force measured was due to the presence of nanobubbles at the hydrophobic solid–liquid interface (Hampton and Nguyen, 2010). Thus, what was thought to be a hydrophobic force was actually a capillary bridging force resulting from the gaseous bridging formed from nanobubbles coalescence (Hampton and Nguyen, 2010). Recent studies found that there are two types of hydrophobic force, a short range

(< 20 nm) reproducible force and a long range (up to 500 nm) variable force (Figure 2-30) (Hampton, Donose and Nguyen, 2008; Ishida, Kusaka and Ushijima, 2012).

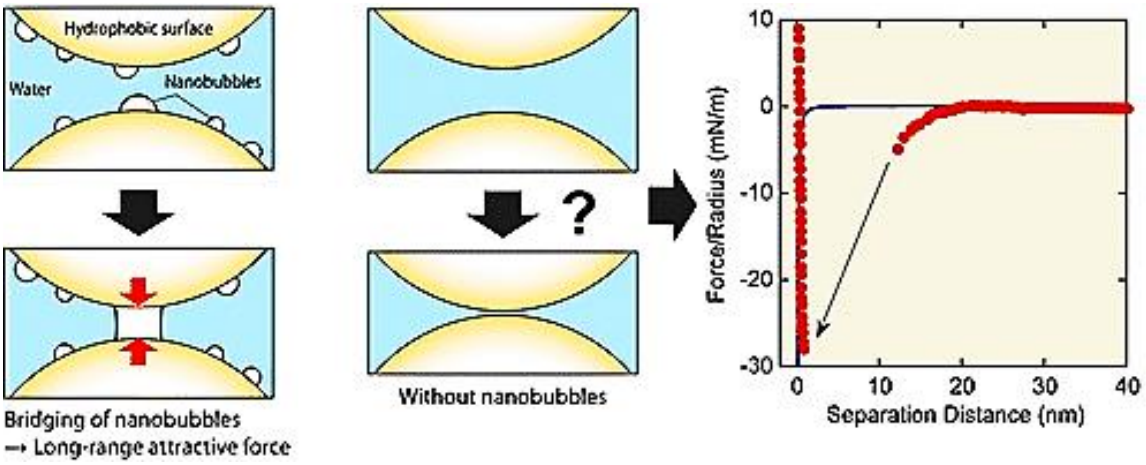

Figure 2-30. Hydrophobic attraction between hydrophobic surfaces in presence and absence of nanobubbles (Ishida, Kusaka and Ushijima, 2012).

Ishida, Kusaka and Ushijima (2012) found that nanobubbles are responsible for the long-range attractive force. On the other hand, in absence of nanobubbles the short-range force, which is stronger than the van der Waals force, is the true hydrophobic force as shown in Figure 2-31 (Ishida, Kusaka and Ushijima, 2012).

The type of alcohol used in the solvent exchange impacts the range of the force, with 1-propanol exchange showing the longest-range force followed by ethanol and methanol as shown in Figure 2-32 (Hampton, Donose and Nguyen, 2008). In addition, an increase in the height or the volume of the nanobubbles results in a nanobubble interaction at larger separation distances between the hydrophobic surfaces, thus the interaction between surfaces treated with 1-propanol will be larger than with methanol, as supported by the force curves in Figure 2-32 (Hampton, Donose and Nguyen, 2008).

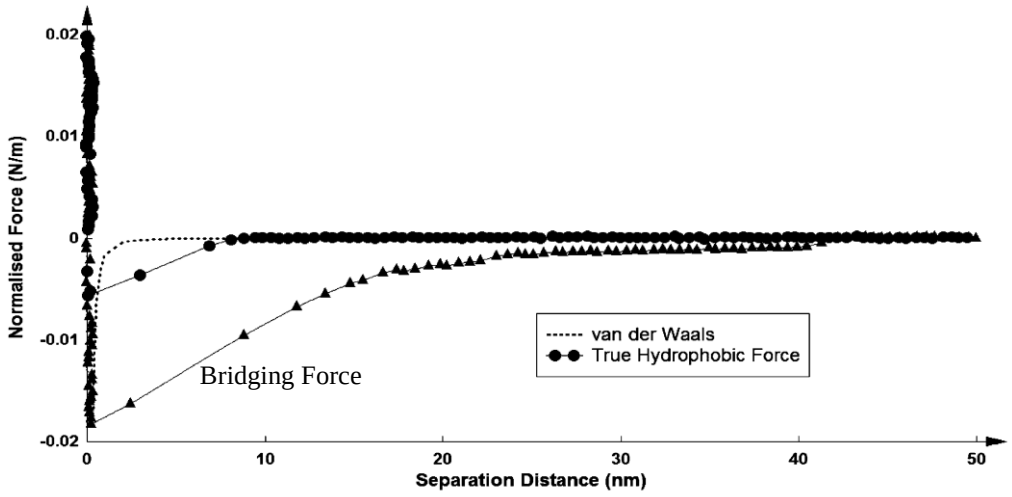

Figure 2-31. The van der Walls force and the hydrophobic attractive force between hydrophobized glass spheres in water at two different condition. One created a short-range (true) hydrophobic force and another produced a long-range nanobubbles bridging force (Hampton, Donose and Nguyen, 2008).

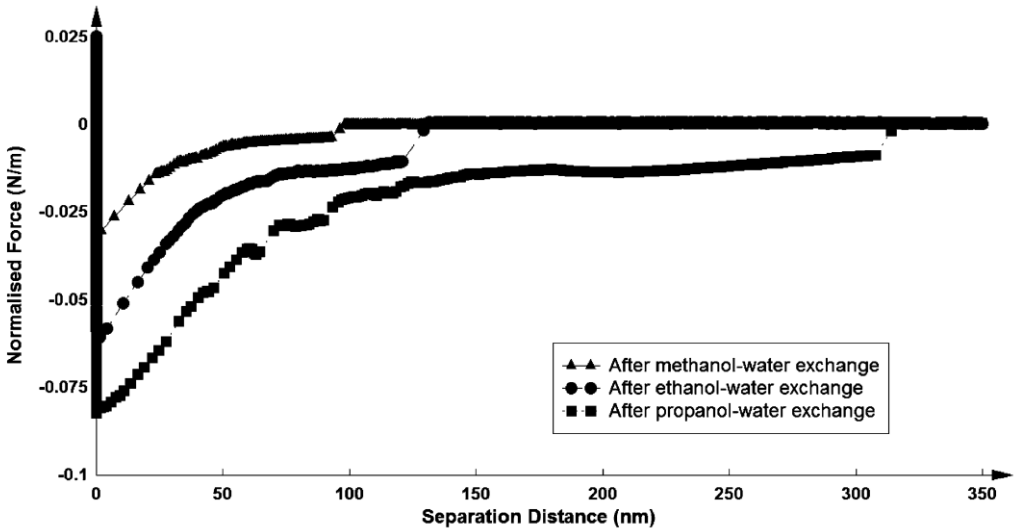

Figure 2-32. Long range hydrophobic force in presence of nanobubbles generated by different alcohol solvents-water exchange (Hampton, Donose and Nguyen, 2008).

2.3.3. Nanobubble and the Regular Bubble – Particle Interaction

The attachment of a hydrophobic particle to air bubble in aqueous solution plays a vital role in froth flotation.

Figure 2-33 shows the particle –bubble interaction process in presence of nanobubbles. Stöckelhuber et al. (2004) found that as the particle approaches the bubble surface, the nanobubbles rupture the aqueous wetting film between the particle and the bubble surfaces. Stöckelhuber et al. (2004) also explained how the subprocesses of this rupture mechanism take place: During the drainage of the wetting film, the apex of the largest nanobubble gets closer to the bubble surface where surface forces are acting. A foam film is formed and in this foam film different Derjaguin-Landau-Verwey-Overbeek (DLVO) forces are acting than in the surrounding wetting film. In the wetting film, all DLVO forces are repulsive, whereas in the foam film the van der Walls force becomes attractive (Figure 2-34). Then the DLVO forces at the apex of the largest nanobubbles deform the water film surfaces, which creates an additional capillary pressure that destabilizes the foam film and leads to rupture of the foam film. Nanobubbles near the hydrophobic surfaces change the van der Waals interaction from repulsive into attractive. Figure 2-34 shows that the interaction between the particles and the bubble greatly depends on the size of the nanobubbles or gas segments along the particle surfaces (Mishchuk, 2004).

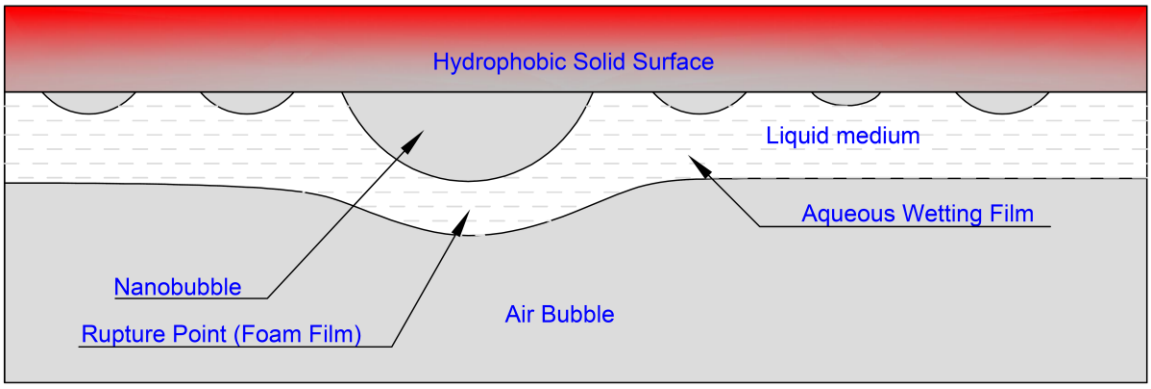

Figure 2-33. Hydrophobic particle - bubble interaction in the presence of nanobubbles (Stöckelhuber et al., 2004).

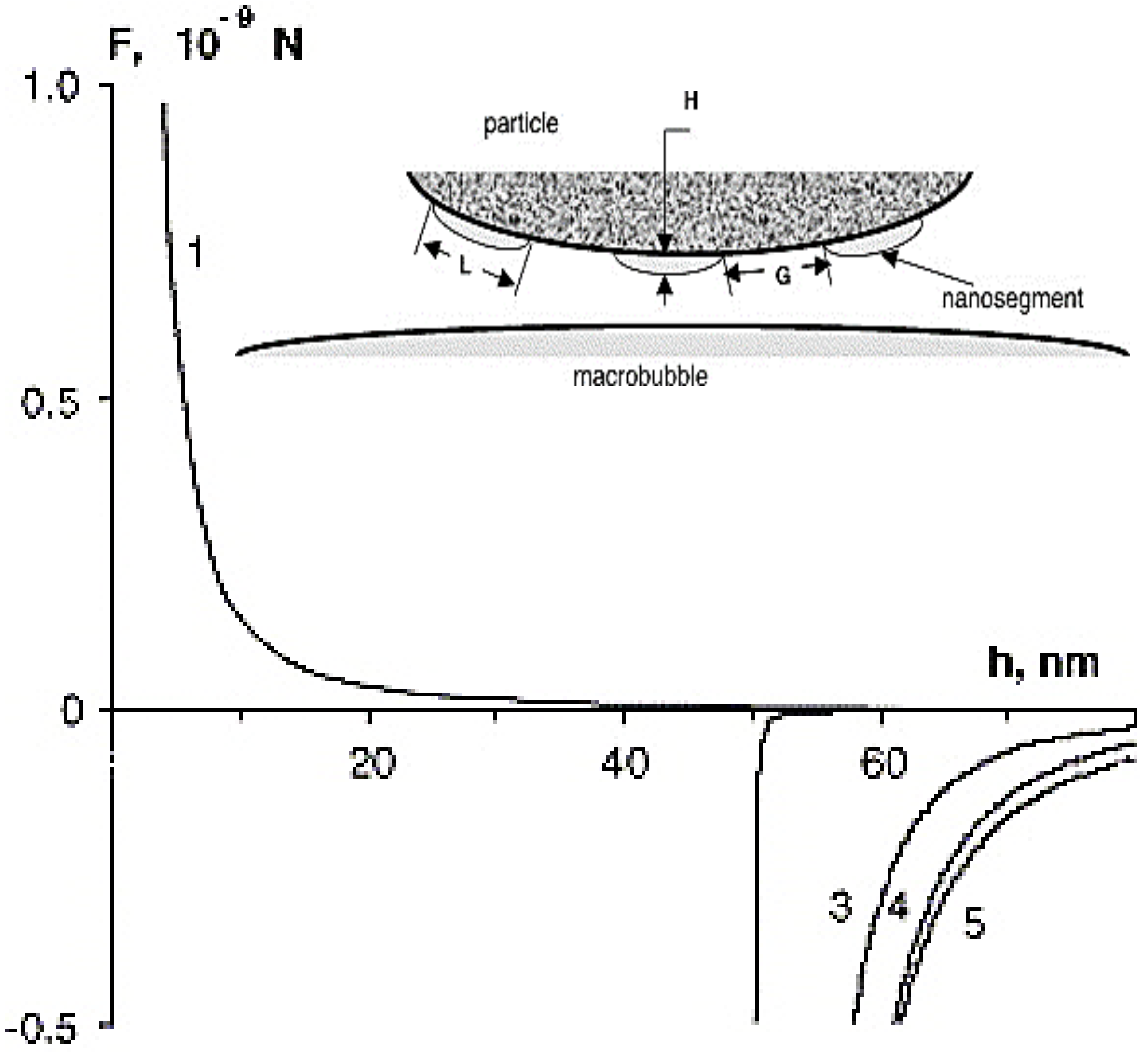

Figure 2-34. Van der Waals forces for particle/bubble interaction: (1) without gas (2) in the presence of a single nanobubbles with radius 50 nm, (3) in the presence of layer of gas segments with thickness 50 nm, (4) in the presence of homogeneous layer of gas segments with thickness 50 nm, (5) In the case when the particle is replaced with an air bubble (Mishchuk, 2004).

CHAPTER 3. EXPERIMENTAL WORK

The following tasks were performed to achieve the above stated objectives.

3.1. SAMPLE ACQUISITION AND CHARACTERIZATION

A total of four 55-gallon drums of coal slurry were acquired from a mine in Illinois. Upon arrival at the lab, the slurry was thoroughly mixed and then split into 5 gallon buckets and sealed for storage and later usage. A representative sample was collected for detailed characterization study.

3.1.1. Size, Ash and Sulfur Distribution Analysis

The particle size distribution of the coal sample was measured by wet sieve analysis using the following U.S. standard sieves: 300, 150, 75, 45 and 25 µm. The different size fractions were filtered, dried, and weighed.

Different size fractions were analyzed for ash content by using LECO TGA-701 (Figure 3-1) and for sulfur content by using LECO S632 sulfur analyzer (Figure 3-2).

Figure 3-1. LECO Thermogravimetric analyzer (LECO TGA-701).

3.1.2. Proximate Analysis

A proximate analysis for each size fraction of the coal sample was determined by conducting experiments using LECO thermogravimetric analyzer (LECO TGA-701) (Figure 3-1). TGA-701 complies with ASTM D 3172 – 89 R02 standard methodology used for the determination of moisture, volatile matter, and ash and the calculation of fixed carbon on coals samples.

Figure 3-2. LECO S632 sulfur analyzer

3.1.3. Flotation Release Analysis

The flotation release analysis illustrated in Figure 3-3 is a procedure used to obtain the best possible separation performance achievable by any froth flotation process, which is analogous to the gravity-based washability analysis. The release analysis was carried out in a conventional laboratory flotation cell and its data was used as a yardstick for performance evaluation of the nanobubble flotation technology.

The first stage of the release analysis separates the hydrophobic material away from the hydrophilic material by doing multiple cleaning phases for the original coal feed slurry. The second stage has the goal of separating particles into fractions of different degrees of surface hydrophobicity by controlling air flow rate and rotator revolutions per minute under starvation reagent conditions.

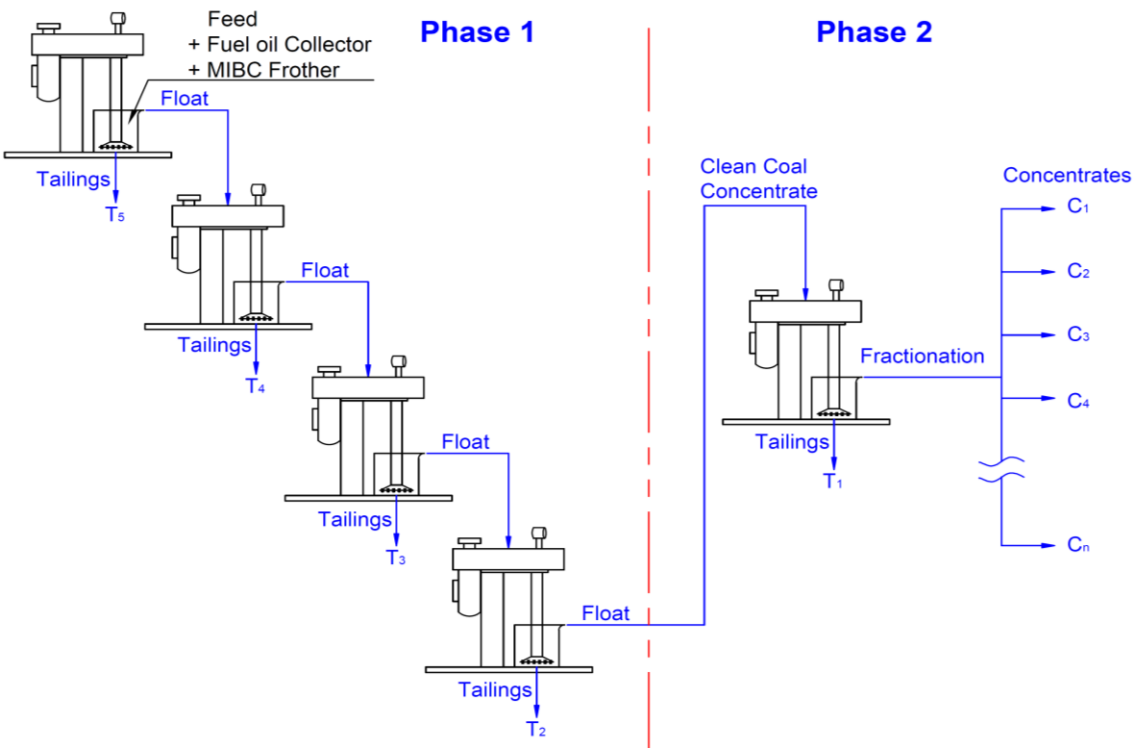

Figure 3-3. Flotation release analysis method using a laboratory conventional Denver flotation cell.

3.1.4. Flotation Kinetic Tests

Kinetic flotation tests were conducted to show the effect of nanobubbles on flotation rate constants. The flotation performance data from these tests in the presence and absence of nanobubbles by conducting Denver batch flotation cell were compared to the release analysis data for a better understanding of effects of nanobubbles.

3.1.5. Zeta Potential of Coal Particles

A fine clean coal (4.5% ash) was obtained from release analysis test of the flotation feed. The sample was thoroughly washed with deionized water and dried in an oven at 100^{o}C for 3 hours. Fuel oil as a collector and MIBC as a frother from Fisher Scientific were used as received. Reagent grade HCl and NaOH were used for pH adjustment. Pure KCl was used as supporting electrolytes for zeta potential measurements. All the experiments

were taken place in deionized water at different collector dosage and different frother concentration. The nanobubbles were generated by conduction an ultrasonic for 5 minutes to measure he zeta potential in presence of the nanobubbles.

Figure 3-4. ZetaPlus zeta potential analyzer

A suspension of 0.05-0.1 g of fine pure coal sample was prepared in the 1 mM KCl solution. The sample was added to 80 ml deionized water in a 100 ml ground flask. KCl was added to produce 1 mM. NaOH and HCl were used to adjust the pH value to a certain value between 2 and 12. The flask was filled with deionized water to the mark to produce the final volume of 100 ml suspension. The suspension was agitated for 15 minutes. After settling for 10 min, the upper portion of the dilute fine particles suspension was taken for zeta potential measurement. Zeta potential measurement was carried out using a ZetaPlus (Model 21401, Brookhaven Instruments Co., Holtsville, New York) (Figure 3-4). At least five measurements of zeta potential were carried out for the mean value. Slurry with a high zeta potential (negative or positive) is electrically stabilized while slurry with a low zeta potential tends to coagulate or flocculate.

3.2. SPECIALLY DESIGNED LABORATORY FLOTATION COLUMN

3.2.1. Design and Fabrication of a Laboratory Flotation Column

A flotation column made of Plexiglas with a 5.08 cm diameter and 2.4 m adjustable height was featured with a Venturi cavitation tube and a static mixer to generate nanobubbles and conventional sized bubbles (microbubbles), respectively as shown in Figure 3-5.

The typical lengths of collection and froth zones used in the tests were 210 cm and 30 cm, respectively. With a diameter of 5.08 cm, the length-to-diameter ratio of the column was around 41:1, which provided near plug-flow conditions. Wash water was added in the froth zone at a depth of 1/3 of the froth zone height below the overflow lip. Feed slurry enters the column in the upper pulp zone, 45 cm below the overflow lip.

The bottom of the froth flotation column was specially designed as two concentric cyclones with one tangential inlet. The outer cyclone was utilized to reject the heavier, coarser, and hydrophilic ash particles from the bottom to the tailing stream. The inner cyclone underflow stream, which consists of the unrecovered hydrophobic coal particles, was recycled and pumped through the static mixer and/or the cavitation tube for further recovery. The hydrophobic particle/bubble aggregates were move inward and upward in the column due to their lower effective density and overflow into the flotation column concentrate.

The total recycling flow rate of slurry through the static mixer is 11 L/min, which splits at a two-way connector into the cavitation tube and a pipe. As a result, the flow rate distribution (flow rate in cavitation tube/total flow rate in static mixer) can be adjusted to be 6.6 L/11.0 L = 60% (with nanobubble) or 0 L/11.0 L = 0% (without nanobubble).

A microprocessor (Series 2600 Love Controls) receives signals from a pressure transducer located at the bottom of the column. The signal adjusts a Miniflex pinch valve that controls the underflow flow rate and the desired froth level.

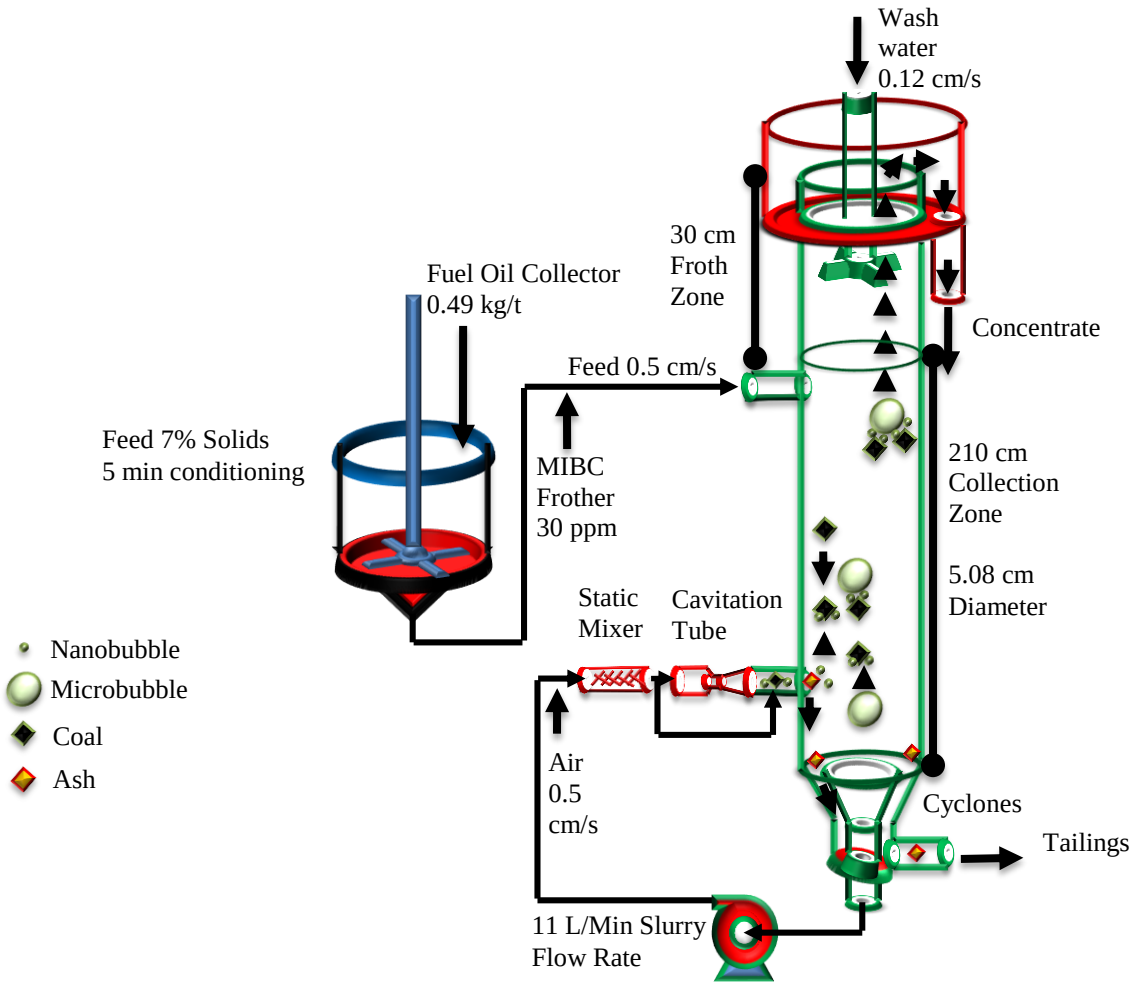

Figure 3-5. Specially designed flotation column with two concentric cyclones

3.2.2. Specially Designed Column Flotation Experiments

Column flotation experiments were performed to demonstrate the effectiveness of nanobubble flotation technology. Major process parameters such as feed size distribution, superficial gas velocity, superficial feed flow rate, superficial wash water flow rate, collector dosage, frother dosage, etc. were examined individually to investigate their effects on flotation performance in the presence or absence of nanobubbles with the specially designed column.

Prior to each test, the feed slurry was conditioned for 5 min with fuel oil to enhance the hydrophobicity of coal particle surfaces. Conditioning was conducted in a sump that was equipped with a mixer and four baffles placed vertically and separated by an equal distance along the circumference of the sump. The slurry was fed from a feed tank, which utilized a recirculating line to ensure suspension of all solids, to the flotation column by a peristaltic pump at a predetermined rate. Frother was pumped into the feed stream while air was injected into the stream prior to the static mixer. Unless otherwise specified, all column flotation tests were performed under the following conditions: froth depth of 30 cm; superficial gas flow rate of 0.5 cm/s; fuel oil collector dosage of 0.49 kg/ton; MIBC frother concentration of 30 ppm; superficial wash water flow rate of 0.12 cm/s; superficial feed slurry flow rate of 0.5 cm/s; as-received feed slurry solids concentration of 7%. A period of time equivalent to three particle retention times was allowed to achieve steady-state conditions. After reaching the steady state, samples of feed, product, and tailing streams were collected simultaneously. These samples were filtered, dried, weighed, and analyzed for ash content.

3.2.3. A Size-By-Size Analysis

A size-by-size analysis of the flotation concentrate and tailings was conducted to determine flotation recovery and separation efficiency for each size fraction. The data from this analysis were used to demonstrate how the nanobubbles affect the flotation recovery and separation efficiency of different particle sizes, which can be further used for process simulation and performance prediction for different coal samples.

3.3. MECHANICAL FLOTATION EXPERIMENTS

Flotation experiments were conducted with a bank of three 10-liters mechanical cells as shown in Figure 3-6 to assess the impact of use of nanobubbles in a mechanical flotation process on coal separation performance at different operating variables. The most significant operation parameters such as collector dosage, frother concentration, feed flow rate, flow rate to nanobubble generator and feed solid concentration were studied

individually. During the tests with nanobubbles, part of the slurry in the third flotation cell was pumped through a nanobubble generator with 3 mm inner neck diameter and 12 mm inner pipe diameter, and then fed back to the first flotation cell. The nanobubbles generated selectively on the hydrophobic particles enhance the flotation separation efficiency as explained earlier.

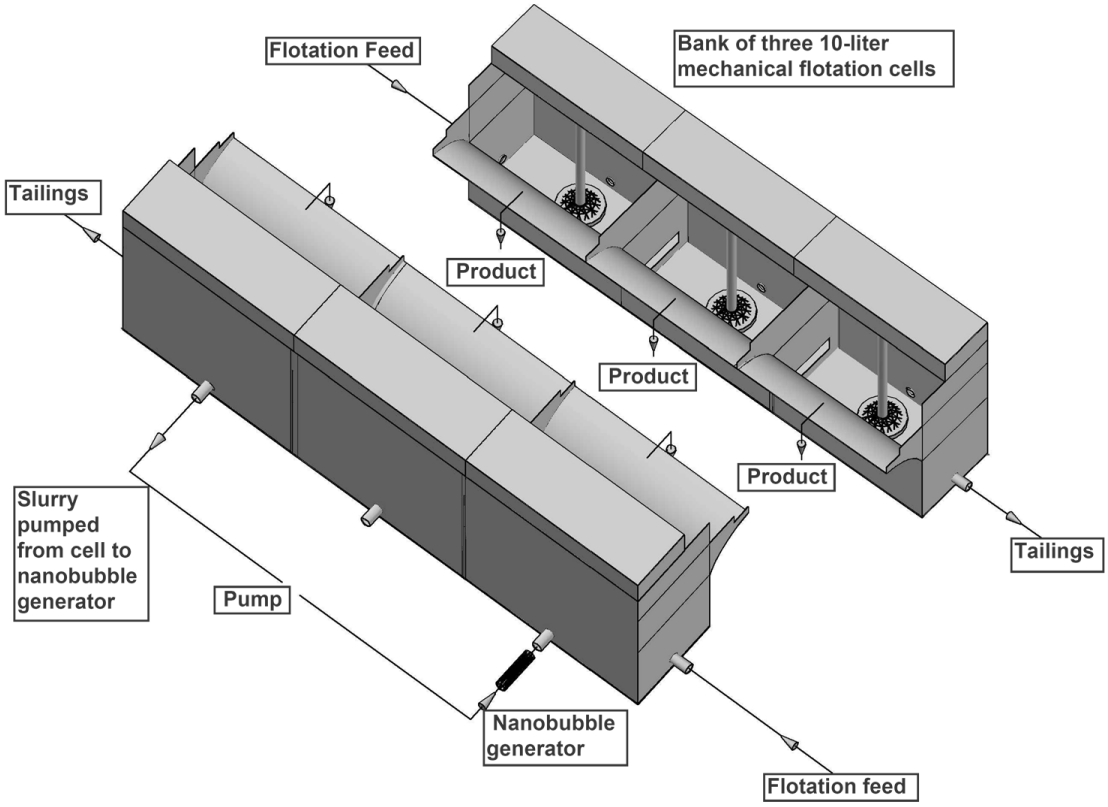

Figure 3-6. Front and back views of a bank of three 10-liters mechanical flotation cells

3.4. FUNDAMENTAL CHARACTERIZATION OF NANOBUBBLES

3.4.1. Nanobubble Formation, Size Distribution and Stability

Nanobubbles were generated in deionized water from dissolved gas by using a special designed apparatus as illustrated in Figure 3-7. In this system, the water with 10 ppm MIBC frother was pumped and circulated through a cavitation tube for about 5 minutes at

the room temperature. The hydrodynamic cavitation process led to the nucleation of the nanobubbles in the water.

The bubbles size distribution was measure using a Cilas 1064 laser particle size analyzer. The range of the size that can be detected is from 0.04 µm to 500 µm. The sampling system for measuring the size distribution of the bubbles is illustrated in Figure 3-7. The bubble size distribution was replicated at least three times before stopping the nanobubble generation process.

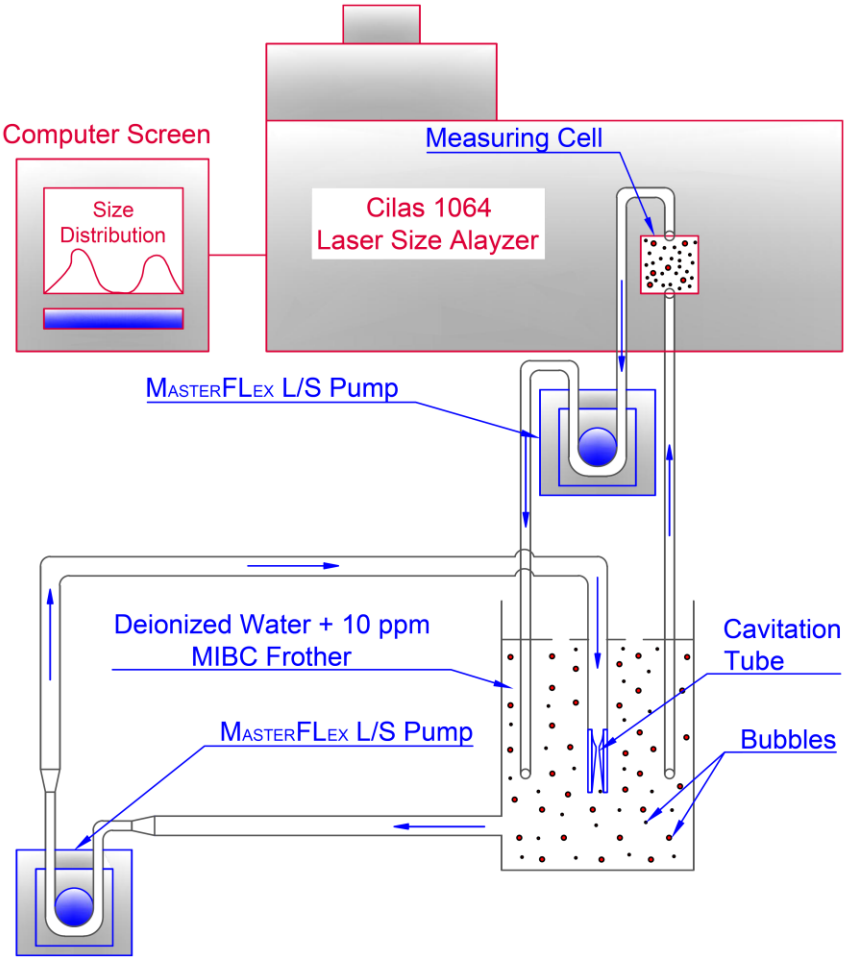

Figure 3-7. Schematic diagram of nanobubbles formation and characterization.

To estimate the stability of the nanobubbles in the liquid, the bubble size distribution was measured as a function of the time for at least 20 minutes after stopping the generation process of the nanobubbles.

3.5. FUNDAMENTAL STUDIES OF ROLE OF NANOBUBBLES

The fundamental studies of the particle-bubble interaction, flotation froth stability, and surface area flux were carried out with "ballontini" glass spheres acquired from Grainger. These spherical particles were microscopically smooth and perfectly hydrophilic with diameter of 110-180 µm. Hydrophobicity of the particles was controlled precisely by a silanation process (Blake and Ralson, 1985; Johansson, Pugh and Alexandrova, 2000; Koh et al., 2009).

A 10 kg sample was treated with acid (2.5% v/v H_2SO_4) for 15 minutes at 60 ^oC. The sample was washed with de-ionized water. The sample was treated again with alkali (2.5% w/v NaOH) and washed with de-ionized water. A 20% w/w glass sphere slurry with de-ionized water in 5 L glass bottle was rolled gently at 180 rpm for 24 hours using a roller mill. The sample was then rinsed with ethanol and dried at 110 ^oC in an oven overnight.

Sub-samples (1.2 kg) of the glass spheres were hydrophobized under different conditions. Analytical grade trimethylchlorosillane (TMCS) and cyclohexane were purchased from Aldrich and used as received without further purification. The sub-samples were treated by partial methylation with TMCS to achieve different degree of hydrophobicity. The sub-samples (1.2 kg) with 1 L of diluted TMCS in cyclohexane (less than 5%) in a 5 L glass bottle were rolled gently (180 rpm) for 24 h for the following reaction to occur (Koh et al., 2009):

$$-Si-OH\ (Surface)+(CH_3)_3SiCl\ (TMCS)\rightarrow -Si-O-Si(CH_3)_3\ (Surface)+HCl\ (Vapour)$$

The slurry was then filtered and rinsed with toluene. The filter cake was tried at 110 ^oC in an oven overnight.

The equilibrium contact angle of the prepared hydrophobic glass spheres were measured by microscopic technique using a pendant drop (Figure 3-8). Solid particles were placed in de-ionized water and left for 1 h to reach the equilibrium state. Then a small tube with a radius of 2 mm was dipped into the suspension. The tube was then pulled out to form a pendant drop and the glass spheres were left to settle on the lower liquid-air interface where they produce a three-phase contact. A microscope was used to observe the settled particle at the most convex part of the pendant drop in the tube. The equilibrium receding contact angle of the particles was estimated according to this formula ($D_{TPC} / D \approx \sin\theta$), where D_{TPC} is the stable diameter of the wetting perimeter and D is the particle diameter (Johansson, Pugh and Alexandrova, 2000).

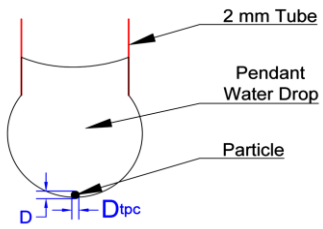

Figure 3-8. Illustration of a microscopic technique using a pendant drop to measure the equilibrium contact angle of the prepared hydrophobic glass spheres (Johansson, Pugh and Alexandrova, 2000).

3.5.1. Particle-Bubble Interaction

A particle-bubble interaction plays a vital role in froth flotation, which is widely used in the recovery of the valuable minerals from gangue minerals. In froth flotation, the bubbles capture and carry the hydrophobic particles selectively to the product stream. There are several significant factors controlling particle-bubble interaction such as bubble diameter, particle diameter, particle density and particle hydrophobicity. In addition to that, this fundamental analysis has shown that nanobubbles generated on particle surface enhance the particle-bubble interaction process and therefore the froth flotation efficiency (Mishchuk, Ralston and Fomasiero, 2006).

The bubble-particle interaction was observed by conducting a high-speed (1200 fps) video microscope technique on a system in which 110-180 µm glass spheres of different hydrophobicity were dropped freely onto a 1.0-1.4 mm bubble formed in water within a glass cell as shown in Figure 3-9. A Tracker 4.80 software, which is a video analysis and modeling tool, was used to analyze the data of the particle-bubble interaction. The radial distance between the particle and the bubble was plotted as a function of time and polar position and the angular speed as a function of polar position.

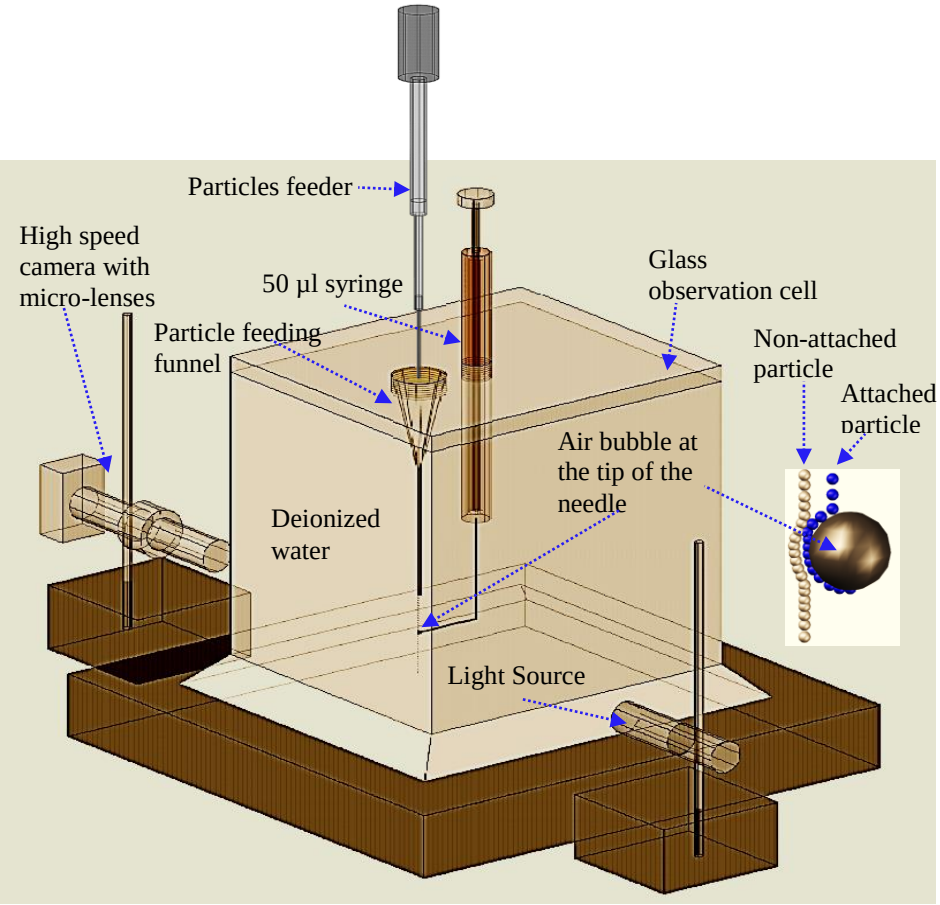

Figure 3-9. Schematic showing a design of particle-bubble interaction method in deionized water with and without nanobubbles on the particle surface and particles trajectory around a bubble surface.

To study effects of nanobubbles, particles were introduced into a small beaker of ethanol to be replaced with deionized water to generate nanobubbles on the particles surfaces prior the experimentation.

During experiments it was observed that some particles showed sudden jumping-in actions toward the bubble after a period of sliding, and were subsequently found to have attached to the air bubble. This jump is interpreted as a result of water film rupture. The induction times determined at the jump were estimated.

The experimental configuration described above is suitable for the task of observing attachment and estimating induction time (Verrelli, Koh and Nguyen, 2011) while the Hallimond tube flotation tests allow only efficiencies or probabilities to be calculated, but do not permit direct estimation of sliding time or induction time.

3.5.2. Flotation Froth Stability

Froth stability plays an important role in determine the mineral quality and recovery accomplished by a froth flotation process. There is no specific criterion to estimate froth stability although a number of parameters are used as indicators for froth stability such as Sauter-mean bubble diameter. Froth stability is dependent not only on the frother type and concentration but also on the particle characteristics, associated chemicals and nanobubbles. Bubble coalescence is governed not only by film thinning or gravity drainage but also by particles.

Bubbles size distribution was measured by a photographic technique at different froth depth in the froth zone after the concentrate reached a steady state in the absence and presence of nanobubbles to better understand how nanobubbles enhance froth flotation of particles with different degree of hydrophobicity.

A high speed camera with micro-lens illustrated in Figure 3-10 was used. Marked distances on the column wall in the field of view of the camera were used so that the bubble size could be estimated. About five images per run were captured and transferred

to a computer and approximately 100 bubbles were used for size measurements in each case by using suitable imaging software such as Digimizer, which is a flexible imaging analysis software package that allows precise manual measurements of the size of the bubbles.

Five degrees of hydrophobicity were investigated, i.e. very strong, strong, intermediate, weak and very weak corresponding to a contact angle of 110º, 85º, 70º, 50º, 20º, respectively. The experiments were conducted using a specially designed flotation column at 0.36 cm/s superficial gas velocity; 0.88 cm/s superficial slurry feed velocity; 0.58 cm/s superficial wash water velocity; 30 mm froth depth; 30 ppm MIBC frother concentration; 5% solids concentration and 12 L/min slurry recycling rate through static mixer. With nanobubbles, 60% of the slurry ejecting from the static mixer flows through the cavitation tube.

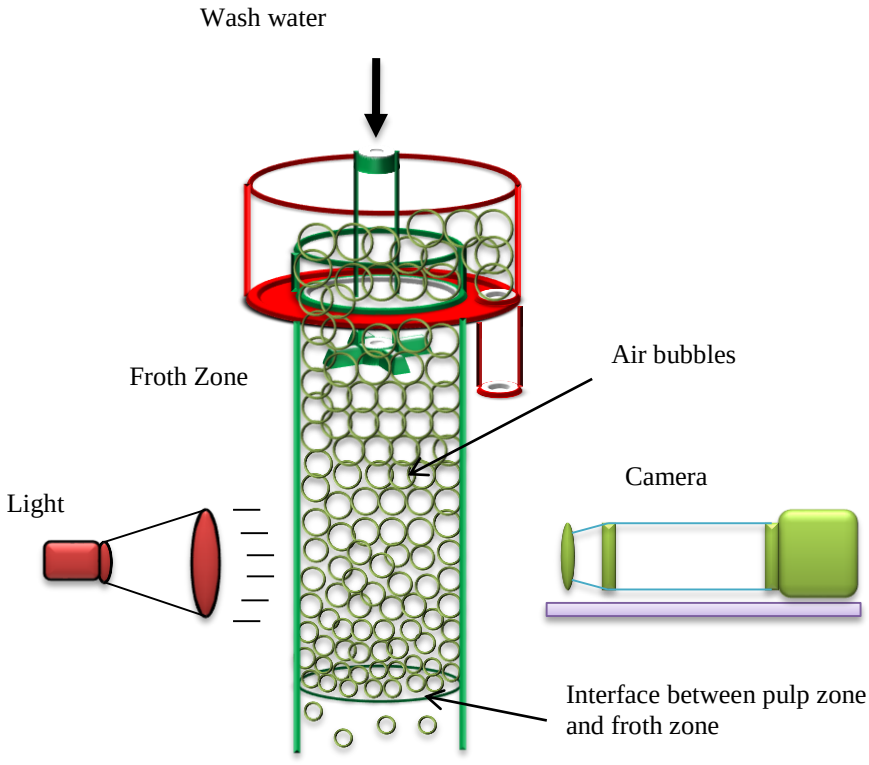

Figure 3-10. Bubbles size measurement and bubbles coalescence in flotation froth.

Bubble coalescence or bubble stability was studied in terms of the Sauter-mean bubble diameter which is used as a representative size for the bubble size distribution in the froth zone. The Sauter-mean bubble diameter (d_{32}) is defined as the volume-to-surface mean bubble diameter as shown in Equation (12):

$$d_{32} = \sum n_i d_i^3 \Big/ \sum n_i d_i^2 \qquad (12)$$

where n_i is the number of bubbles with diameter d_i.

Variation of bubble size distribution and Sauter-mean bubble diameter as a function of column height in froth zone for glass spheres of various degree of hydrophobicity in the presence and absence of nanobubbles was evaluated and plotted.

3.5.3. Surface Area Flux

The surface area of conventional sized bubbles in the flotation slurry was measured to quantify the impact of nanobubbles on the total bubble area flux S_b which is formally defined as the surface area of bubbles per unit cross sectional area of flotation cell per unit time as illustrated in Figure 3-11. The S_b is the available bubble area for transporting particles to the product.

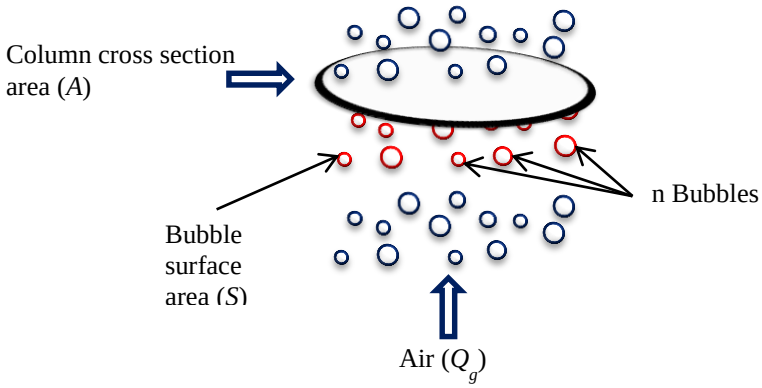

Figure 3-11. Bubble surface area flux schematic derivation diagram (Zhang, 2009).

From superficial gas flow rate V_g and bubble size D_b data in froth zone, the bubble surface area flux was plotted as a function of the distance from the pulp-froth interface where ($S_b = 6\frac{V_g}{D_b}$).

3.6. ECONOMIC EVALUATION OF NANOBUBBLE ENHANCED COAL FLOTATION

A detailed technical performance and economic feasibility evaluation was performed using the data generated from sections 3.2 and 3.3. Feed throughput, product ash, yield, combustible recovery, separation efficiency, capital and operating costs were used to perform evaluation.

CHAPTER 4. EXPERIMENTAL RESULTS, OBSERVATIONS & DISCUSSIONS

4.1. SAMPLE CHARACTERIZATION

4.1.1. Particle Size, Ash and Sulfur Distribution

The ash and sulfur contents for each size fraction of the coal sample are shown in Table 4.1 and Figure 4-1. It can be clearly seen that ash content of the sample decreases as the particle size increases. Figure 4-1 indicates that the majority of coal particles (about 82.97%) were smaller than 150 µm and 40.70% of coal particles were smaller than 25 µm. The overall feed ash content was 38.51%. In addition, the sulfur content decreases as the particle size increases.

Table 4.1. Size analysis data for tested coal sample.

Particle size (µm)	Elemental			Cumulative Passing			Cumulative Retained		
	Wt (%)	Ash (%)	Sulfur (%)	Wt. (%)	Ash (%)	Sulfur (%)	Wt. (%)	Ash (%)	Sulfur (%)
+300	1.58	4.62	2.39	100.00	38.51	2.99	1.58	4.62	2.39
-300+150	15.44	5.97	2.47	98.42	39.05	3.00	17.03	5.84	2.46
-150+75	19.96	9.78	2.65	82.97	45.21	3.10	36.99	7.97	2.56
-75+45	16.59	24.19	3.58	63.01	56.43	3.25	53.58	12.99	2.88
-45+25	5.72	33.05	4.23	46.42	67.96	3.13	59.30	14.93	3.01
-25	40.70	72.87	2.97	40.70	72.87	2.97	100.00	38.51	2.99
Total	100.00	38.51	2.99						

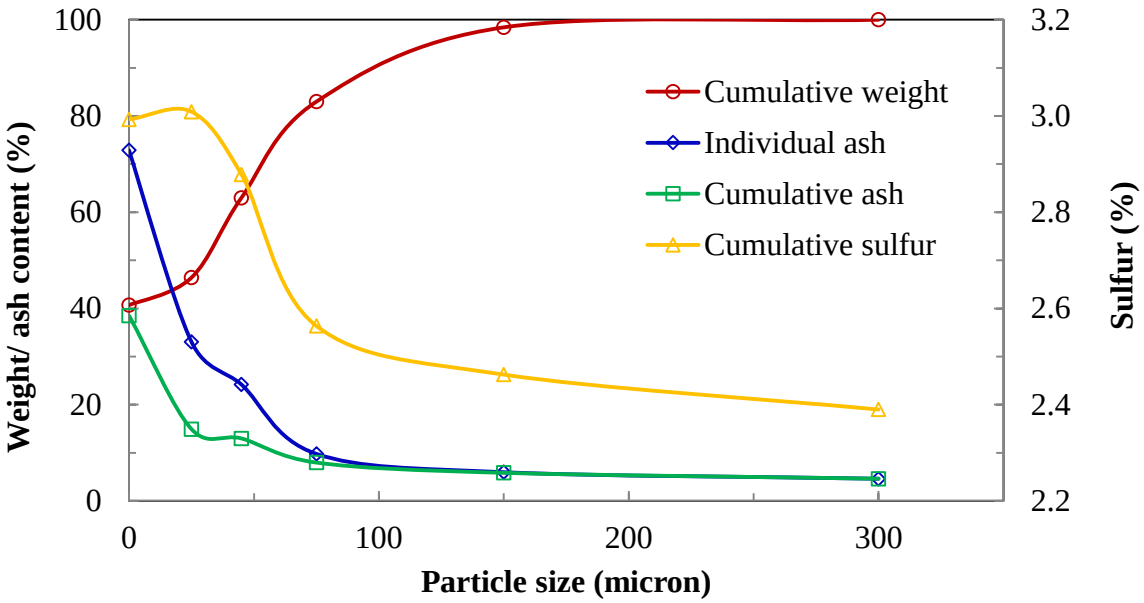

Figure 4-1. Particle size, ash and sulfur distribution of tested coal sample.

4.1.2. Proximate Analysis

The proximate analysis for each size fraction of the feed coal sample is shown in Table 4.2. The moisture, ash, volatile matter and fixed carbon contents of the sample decrease as the particle size increases. This is the result of the concentration of fine clay particles in smaller size ranges.

Table 4.2. Proximate analysis of different size fractions of feed coal sample

Particle size (µm)	Wt (%)	Moisture (%)	Ash (%)	Volatile Matter (%)	Fixed Carbon (%)
+300	1.58	3.51	4.62	35.72	56.15
-300+150	15.44	3.57	5.97	34.87	55.59
-150+75	19.96	3.34	9.78	33.18	53.70
-75+45	16.59	2.80	24.19	29.42	43.59
-45+25	5.72	2.48	33.05	25.19	39.28
-25	40.70	1.87	72.87	12.93	12.33
Total	100.00	2.64	38.51	24.16	34.69

4.1.3. Flotation Release Analysis

Figure 4-2 shows the flotation product ash of the coal sample versus the combustible recovery and product yield. Figure 4-3 shows the ash rejection versus the combustible recovery. It can be seen from the figure that at the product ash content of 7.7% the product yield is 61.64%. The flotation combustible recovery and ash rejection at this product ash content are 93.37% and 87.86%, respectively while the ash content in the tailing is 89.46%.

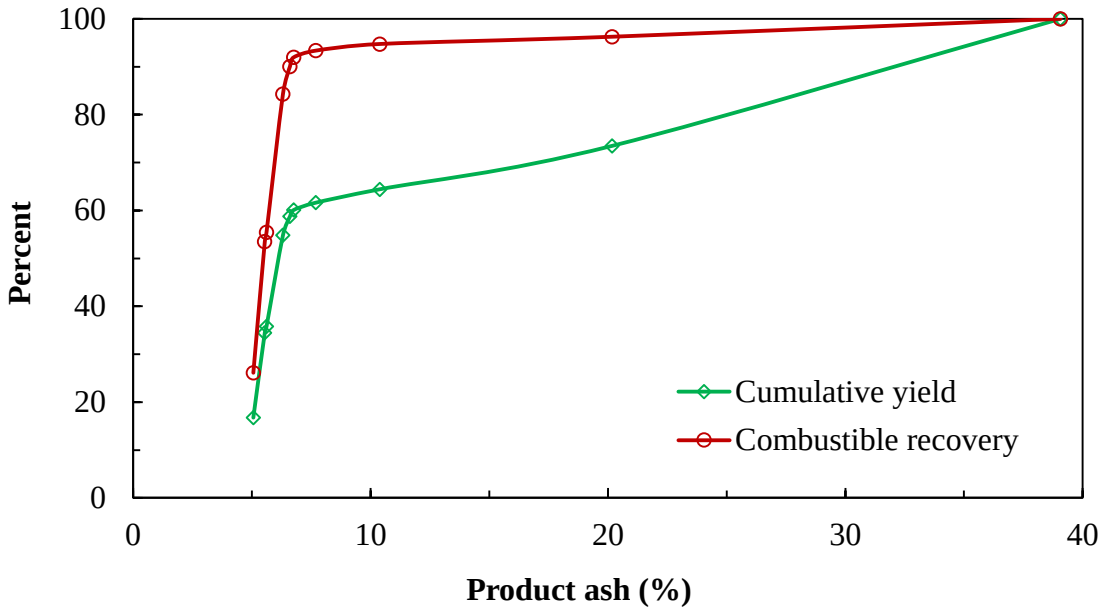

Figure 4-2. Release analysis result of tested coal sample. Cumulative yield and combustible recovery vs. product ash.

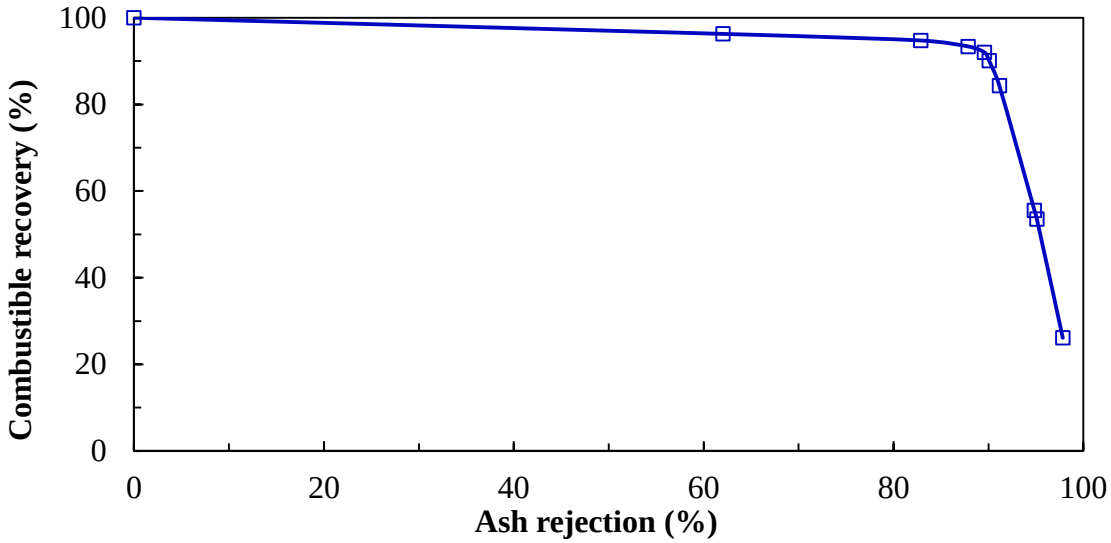

Figure 4-3. Release analysis result of tested coal sample. Combustible recovery vs. ash rejection.

4.1.4. Flotation Kinetic Tests

Batch flotation tests were conducted with a Denver flotation cell and kinetic flotation rates were calculated to show the effect of nanobubble application. The flotation product was collected after 15, 30, 45, 60, 120, 240 and 480 seconds and samples were measured for their weight and ash content from which the recovery was calculated and the results are plotted in Figure 4-4. These test results proved that flotation in the presence of nanobubbles had a much higher combustible recovery and yield in a shorter time than flotation in the absence of nanobubbles. The rate constant increased from 2.12 min^{-1} to 2.99 min^{-1} in the presence of nanobubbles. In other words, nanobubble application increased the flotation rate constant by 41%. Also, it is clear that the product ash is lower in the presence of nanobubbles than in their absence.

The kinetic flotation test results with nanobubbles were much closer to the release analysis curve than those without nanobubbles as shown in Figure 4-5. The curve closer to the upper left corner represents higher flotation selectivity for coal particles, which can be achieved by increasing the collision and adhesion probabilities and reducing the

detachment probability during flotation. In a previous work, improved flotation rate has been reported when nanobubbles co-exist with conventional-sized flotation bubbles (Zhou et al., 1997).

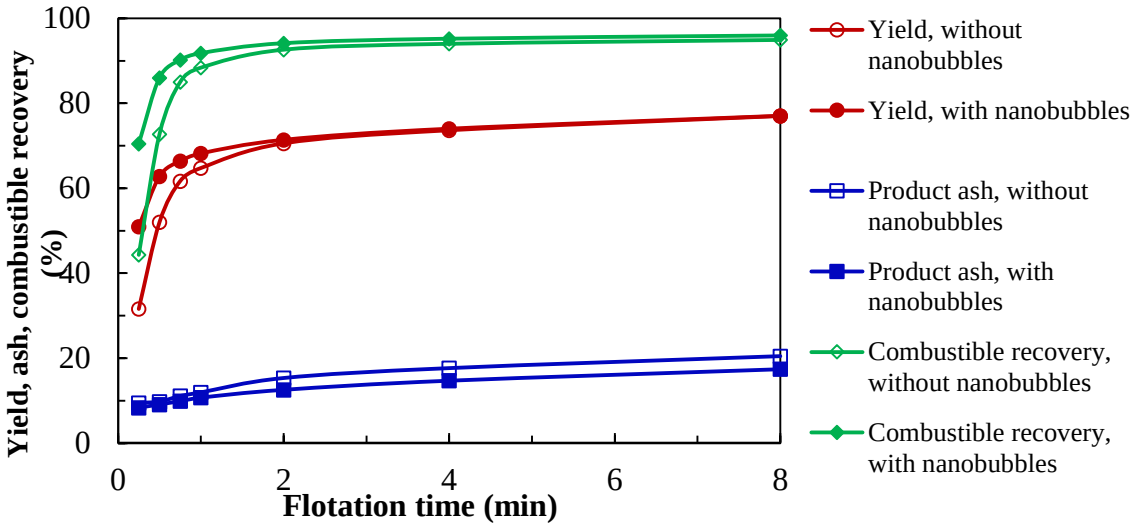

Figure 4-4.Kinetic rate tests of batch flotation in Denver cell with and without nanobubbles.

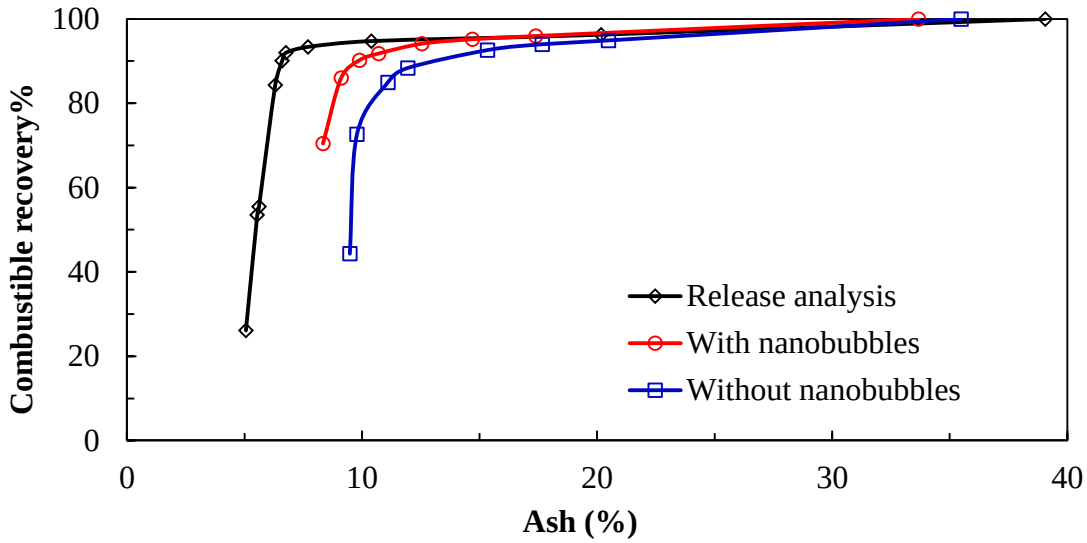

Figure 4-5. Comparing kinetic flotation tests with and without nanobubbles to release analysis.

4.1.5. Zeta Potential of Coal Particles

The zeta potential of clean coal (4.5% ash), in the absence of frother and collector, is negative over the pH range 6-12 as shown in Figure 4-6, with the potential becoming more negative as the pH increases, due to the increased [OH^-]. Figure 4-6 shows that the coal sample possesses -40 mV zeta potential value at pH 7. At least five measurements were performed for the mean value at each pH. The standard deviation as well as the mean value is shown in Figure 4-6. The slurry with a high zeta potential at high pH value is electrically stabilized while slurry with a low zeta potential at low pH tends to coagulate or flocculate as shown in Figure 4-7.

Figure 4-8 shows the zeta potential of pure coal in the absence and presence of nanobubbles at a pH 7.5 and at different fuel oil concentrations. In the absence of the nanobubbles, adding the fuel oil to a suspension of pure coal changed the zeta potential from -23 mV to -40 mV and then to -67 mV.

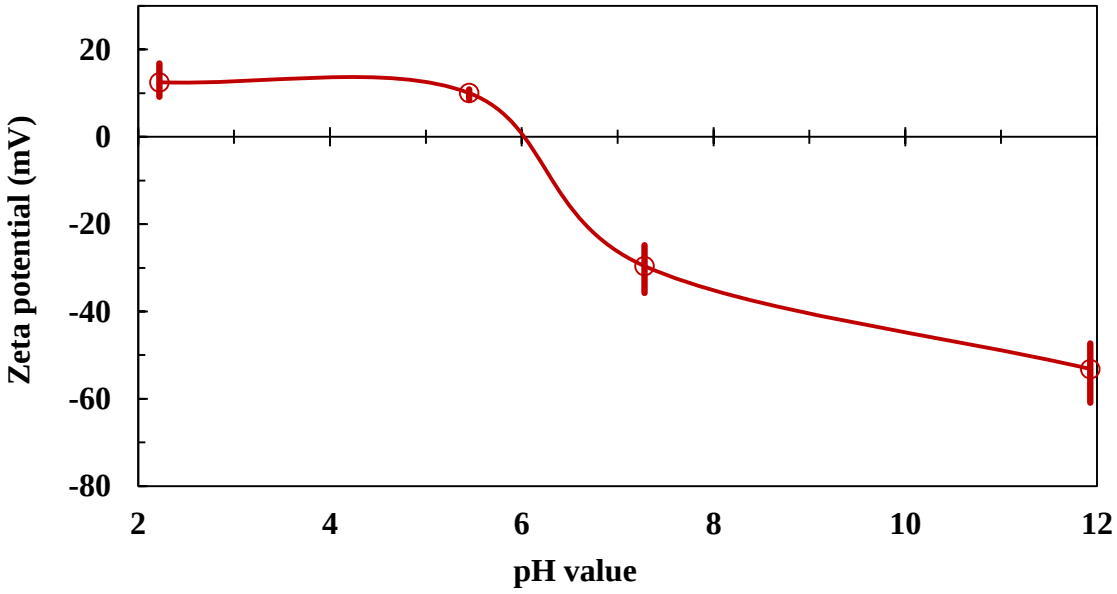

Figure 4-6. Zeta potential of clean coal (4.5% ash) as a function of solution pH value (10^{-3} M KCl).

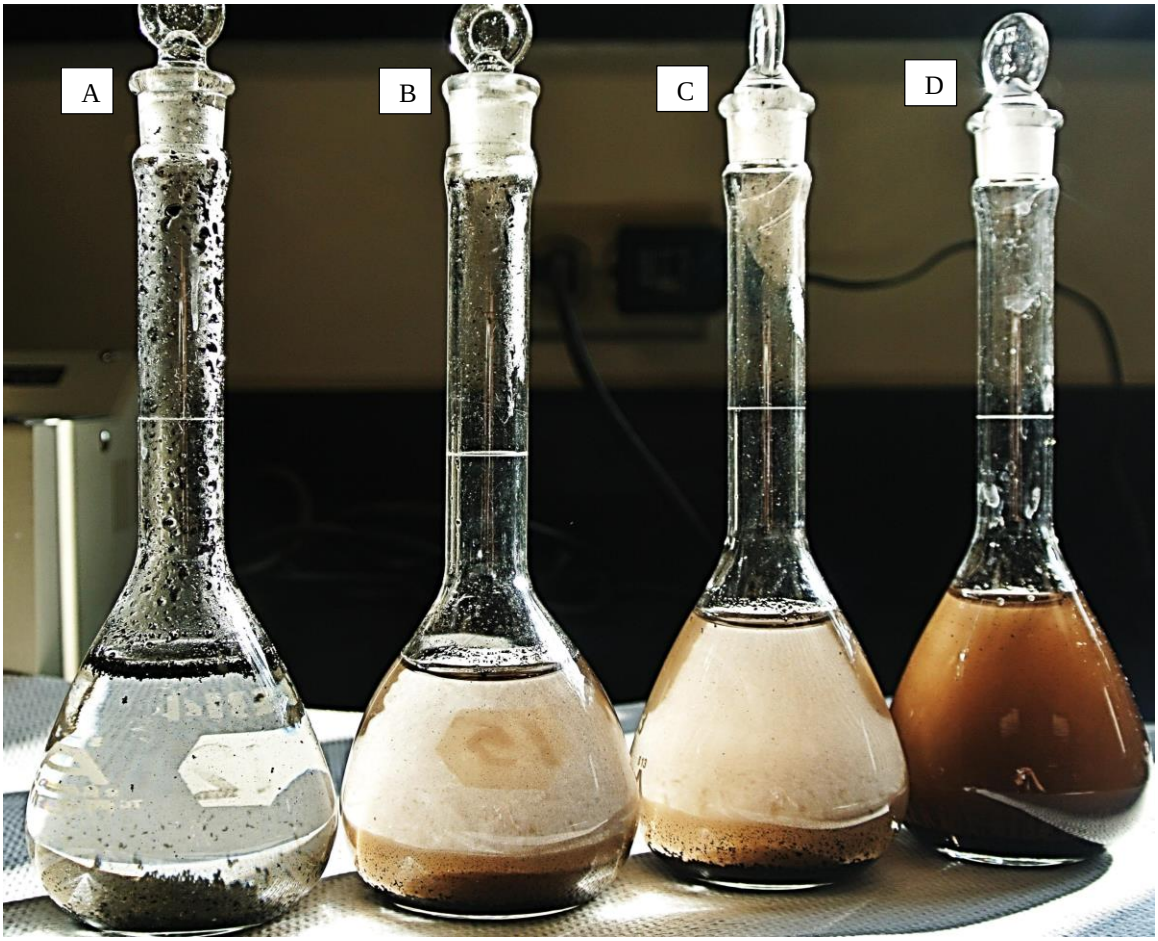

Figure 4-7. Clean coal slurry at different pH values; (A) pH 2.22 (B) pH 5.45 (C) pH 7.28 (D) pH 11.93.

The presence of the nanobubbles changed the zeta potential from -40 mV to -65 mV as a result of adding 100 ppm fuel oil to the suspension of pure coal (Figure 4-8). Increasing the fuel concentration from 100 ppm to 1000 ppm reduced the negative zeta potential from -65 mV to -47 mV. This may be mainly because fuel oil competes with nanobubbles to attach to the surface of the coal particles, and nanobubbles work as a secondary collector which reduces the fuel oil (collector) consumption by up to one half, as will be shown in Section 4.1.2. Figure 4-9, Figure 4-10 and Figure 4-11 show the suspensions of pure coal with and without nanobubbles at different fuel oil concentrations.

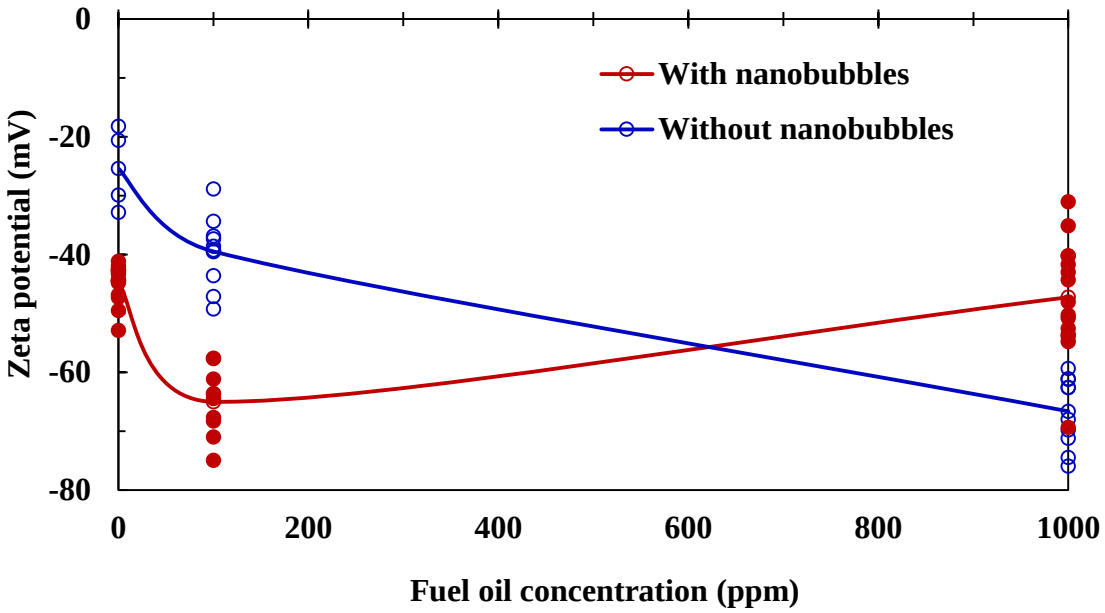

Figure 4-8. The zeta potential of pure coal in the absence and presence of nanobubbles as a function of fuel oil concentration in deionized water of 10^{-3} M KCl ionic strength at a pH value of 7.5.

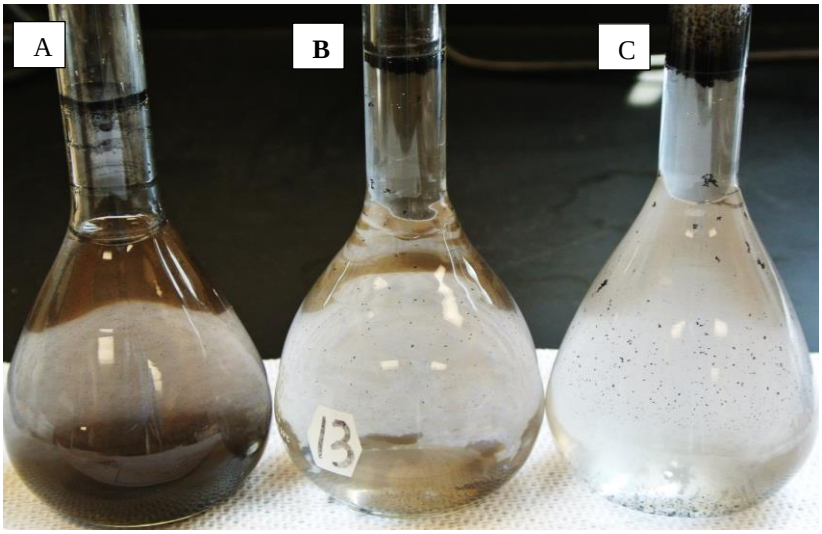

Figure 4-9. Pure coal suspension of 10^{-3} M KCl without nanobubbles at a pH value of 7.5 and different fuel oil concentrations; (A) 0 ppm (B) 100 ppm (C) 1000 ppm.

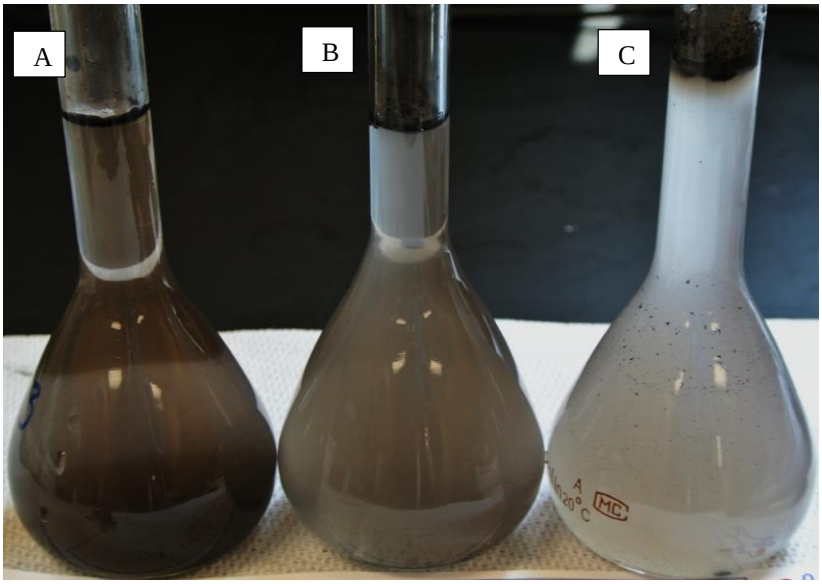

Figure 4-10. Pure coal suspension of 10^{-3} M KCl with nanobubbles at a pH value of 7.5 and different fuel oil concentrations; (A) 0 ppm (B) 100 ppm (C) 1000 ppm.

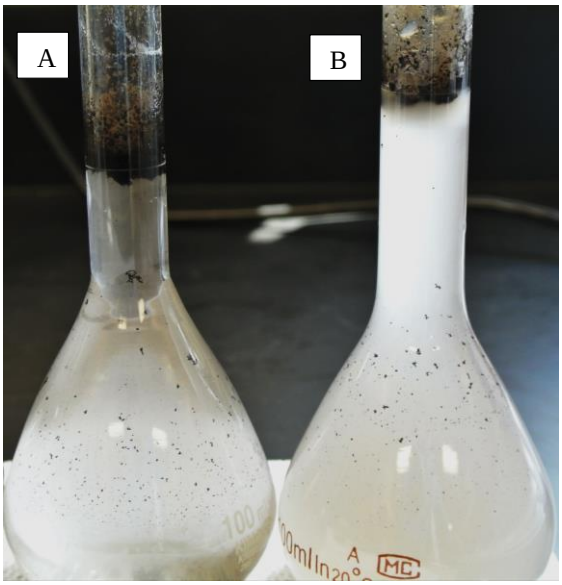

Figure 4-11. Pure coal suspension of 10^{-3} M KCl at pH 7.5 and 1000 ppm fuel oil concentration without nanobubbles (A) and with nanobubbles (B).

Figure 4-12 shows the zeta potential of pure coal in the absence and presence of nanobubbles at a pH value of 7.5 and at different MIBC frother concentrations. In the absence of nanobubbles, adding MIBC to a suspension of pure coal changed the zeta potential from -23 mV to -42 mV. Figure 4-12 shows that in the presence of nanobubbles the zeta potential kept constant at -42 mV even with increasing the MIBC concentration from 0 ppm to 500 ppm. It is unclear why the frother changed the zeta potential of the pure coal sample only in the absence of the nanobubbles. This may be because in the presence of the nanobubbles the zeta meter is detecting the charge of the nanobubbles generated on coal particles instead of detecting the charge of the coal particles.

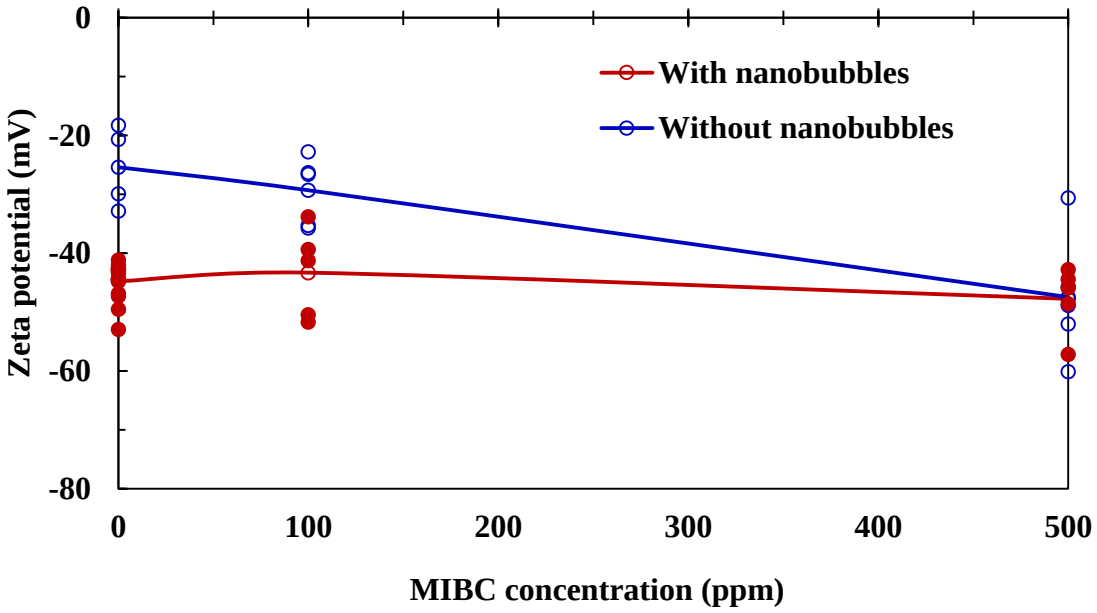

Figure 4-12. The zeta potential of pure coal in the absence and presence of nanobubbles as a function of MIBC frother concentration in deionized water of 10^{-3} M KCl ionic strength at a pH value of 7.5.

4.2. SPECIALLY DESIGNED LABORATORY COLUMN FLOTATION

A detailed evaluation of the effects of nanobubbles on coal flotation performance was carried out in a specially designed laboratory-scale flotation column shown in Figure 3-5 at different operation parameters. Unless otherwise specified, all column flotation tests were performed under the following conditions: froth depth of 30 cm; superficial gas flow rate of 0.5 cm/s; fuel oil collector dosage of 0.49 kg/ton; MIBC frother concentration of 30 ppm; superficial wash water flow rate of 0.12 cm/s; superficial feed slurry flow rate of 0.5 cm/s; as-received feed slurry solids concentration of 7%.

4.2.1. Nanobubble Enhanced Laboratory Column Flotation

Figure 4-13 shows the effect of nanobubbles on combustible recovery and product ash at varying collector dosages of 0.07, 0.23, 0.49 and 0.80 kg/ton. It can be seen that nanobubbles increased flotation recovery by about 5 to 10 percentage points. Also, without nanobubbles the maximum combustible recovery was about 90% achieved at 0.5 kg/ton collector; with nanobubbles a 90% combustible recovery was obtained at 0.25 kg/ton. In other words, nanobubbles reduced collector dosage by one-half to achieve the same recovery. This is due to the fact that nanobubbles generated by hydrodynamic cavitation preferentially appear on hydrophobic particle surfaces and act as a secondary collector. This advantage is particularly important for ultrafine and oxidized coal samples since they normally require high dosages of reagents in conventional flotation processes. Figure 4-13 indicates that increasing collector dosage to 0.8 kg/ton further increased combustible recovery to about 94% in the presence of nanobubbles but combustible recovery decreased to 84% in the absence of nanobubbles. Product ash content was lower at 0.25 kg/ton collector dosage and higher at higher collector dosages in the presence of nanobubbles than in their absence, as a result of more coal particles recovered.

Figure 4-14 depicts the effect of nanobubbles on coal flotation separation efficiency defined as the difference between combustible recovery and ash recovery at varying

collector dosages. It is clear from Figure 4-14 that the separation efficiency of froth flotation was almost higher with nanobubbles present in the system. Figure 4-14 also indicates that the highest efficiency was obtained at 0.25 kg/ton in the presence of nanobubbles and 0.5 kg/ton in the absence of nanobubbles. This confirms that the optimum collector dosage was reduced 50% by use of nanobubbles.

The results are consistent with previous studies that have shown that nanobubbles generated by hydrodynamic cavitation change surface characteristics of minerals (Hampton and Nguyen, 2010), increase contact angle of solids and hence attachment force (Fan et al, 2010b), bridge fine particles to form aggregates, and in consequence reduce reagent consumption (Zhou et al., 1997; Fan and Tao, 2008). A higher dosage of oily collector such as fuel oil used in this study improves coal hydrophobicity and thus increases the particle-bubble attachment probability but it increases flotation operation costs and reduces flotation selectivity and separation efficiency. A better approach to increase flotation recovery is to generate nanobubbles on solid surface, as shown above.

Figure 4-15 shows the combustible recovery and clean coal ash as a function of frother concentration with and without nanobubbles. Similar to the collector effect, nanobubbles reduced frother concentration by one-third. For example, without nanobubbles, maximum combustible recovery was about 89% at 55 ppm frother concentration, but with nanobubbles 92.5% combustible recovery was obtained at 35 ppm frother concentration. Figure 4-15 shows that the product ash content was higher in the presence of nanobubbles than in its absence. This is primarily a result of higher combustible recovery when nanobubbles were utilized. The separation efficiency, defined as the difference between combustible recovery and ash recovery, vs. frother concentration curve shown in Figure 4-16 indicates that use of nanobubbles significantly improved the flotation separation efficiency of coal particles. The improved separation efficiency by nanobubbles observed in Figure 4-16 is a result of selectivity of nanobubble generation discussed earlier.

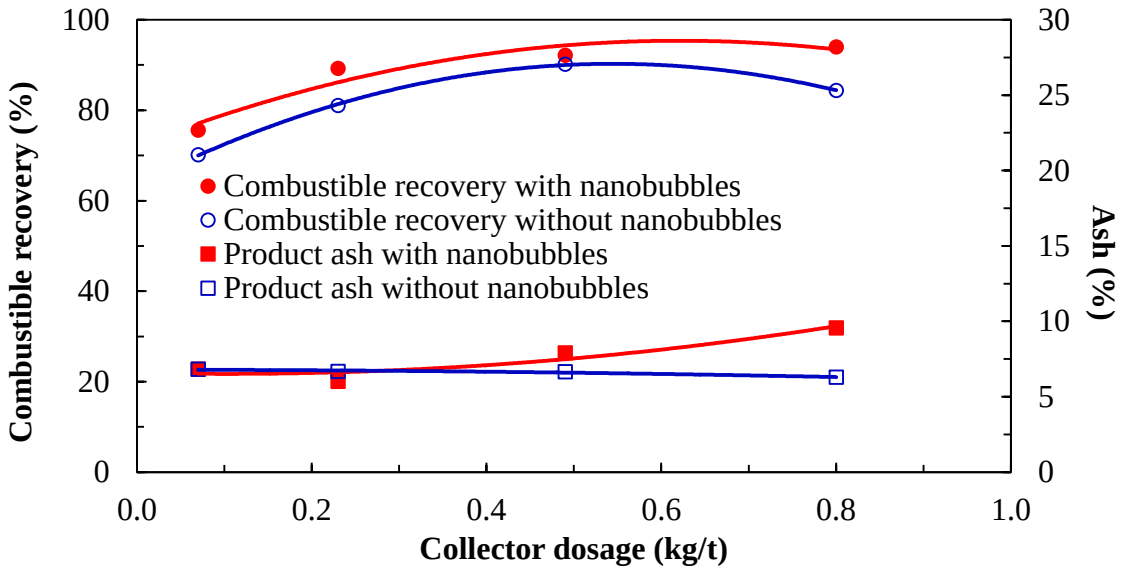

Figure 4-13. Effect of nanobubbles on the combustible recovery at varying collector dosages in specially designed laboratory flotation column of 5.08 cm diameter.

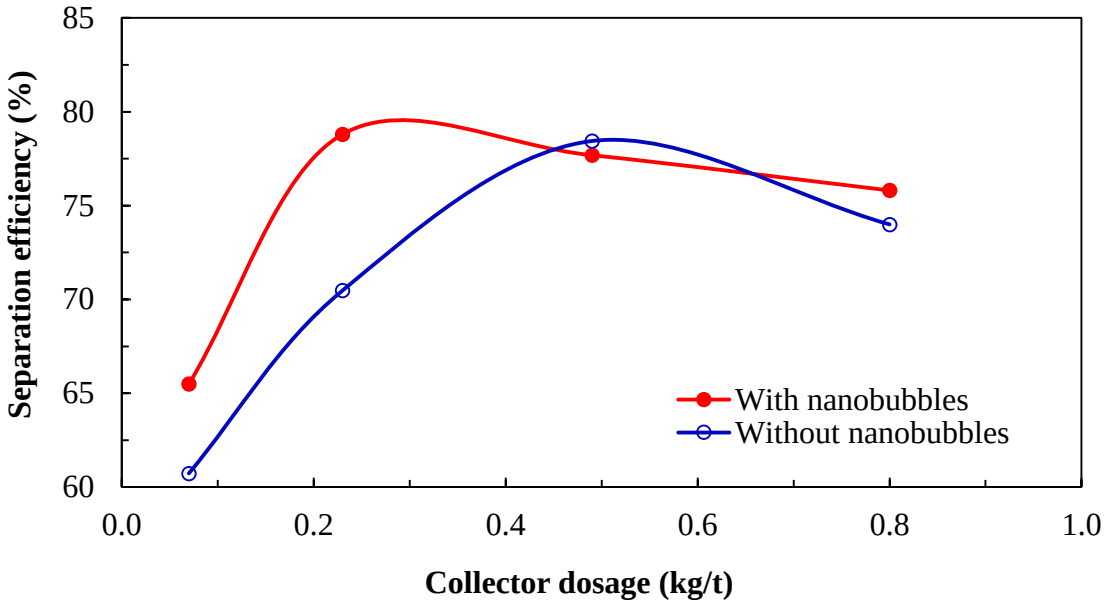

Figure 4-14. Separation efficiency vs. collector dosage with and without nanobubbles in specially designed laboratory flotation column of 5.08 cm diameter.

Higher frother concentration decreased the microbubbles and nanobubbles sizes and increased their concentrations in liquid, which increased the probability of collision. In addition, nanobubble coated surfaces of very fine particles can lead to particle aggregation and thus more easily recovered due to an increased collision probability.

To investigate the influence of the feed flow rate on flotation performance, different feed flow rates of 0.25, 0.50, 0.75 and 1.00 cm/s were examined. Nanobubbles increased flotation recovery, particularly at higher superficial feed velocities, as shown in Figure 4-17. For example, an increase of approximately 28%, i.e., from 56% to almost 84%, in combustible recovery was obtained at a superficial feed velocity of 0.75 cm/s in the presence of nanobubbles, while an increase of approximately 14%, i.e., from 33% to almost 47%, in combustible recovery was obtained at a superficial feed velocity of 1.0 cm/s in the presence of nanobubbles. Although combustible recovery decreased from 94% to 47% when superficial feed velocity increased from 0.25 to 1.0 cm/s, it was still much higher in the presence of nanobubbles than in their absence.

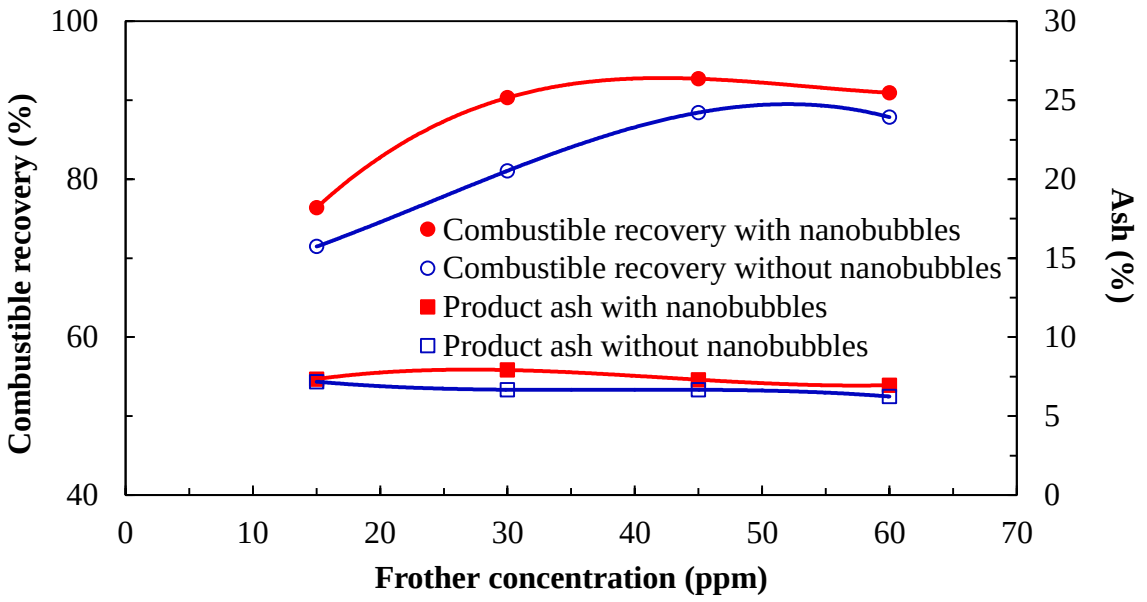

Figure 4-15. Effect of nanobubbles on the combustible recovery at varying frother concentrations in specially designed laboratory flotation column of 5.08 cm diameter.

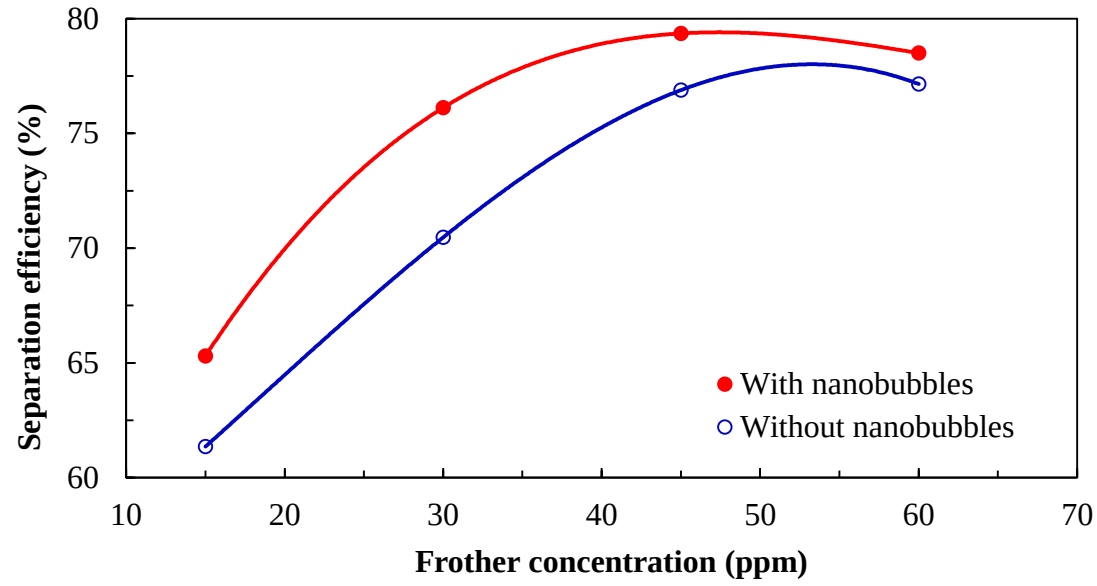

Figure 4-16. Separation efficiency vs. frother concentration with and without nanobubbles in specially designed laboratory flotation column of 5.08 cm diameter.

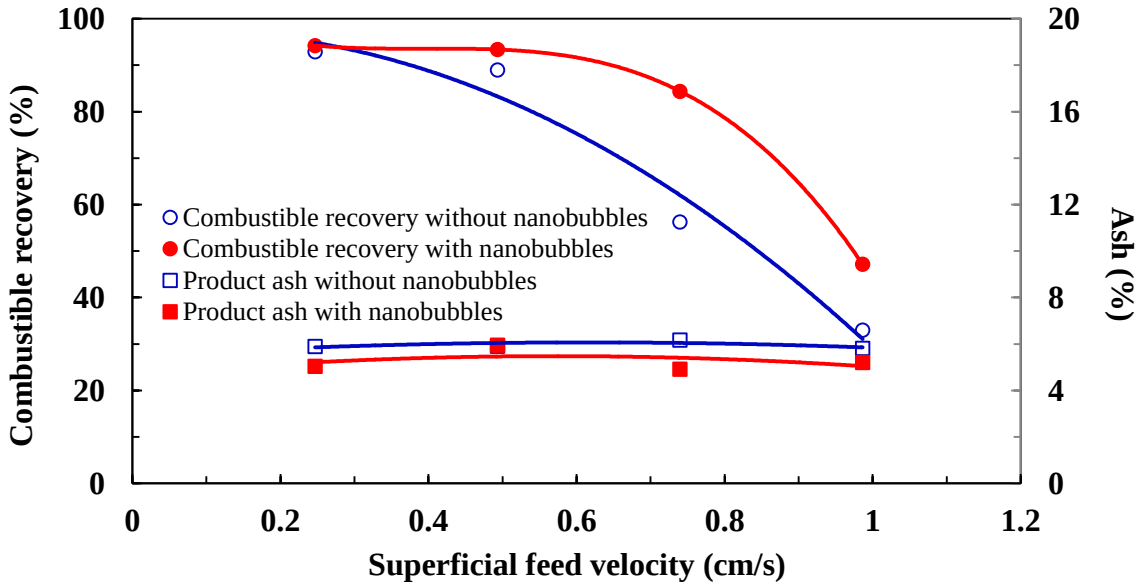

Figure 4-17. Effect of nanobubbles on the combustible recovery at varying superficial feed velocities in specially designed laboratory flotation column of 5.08 cm diameter.

The product ash content was lower or almost the same in the presence of nanobubbles than in its absence. The separation efficiency curve shown in Figure 4-18 indicates that the use of nanobubbles significantly improved the separation performance at superficial feed velocity larger than 0.5 cm/s. This is because nanobubbles reduced the probability of detachment of the attached hydrophobic particles from bubbles. Furthermore, after collision and attachment, particles attached to air bubbles do not all report to the froth phase and some of them detach from bubble surface and drop back into the pulp phase when superficial feed rate was very high.

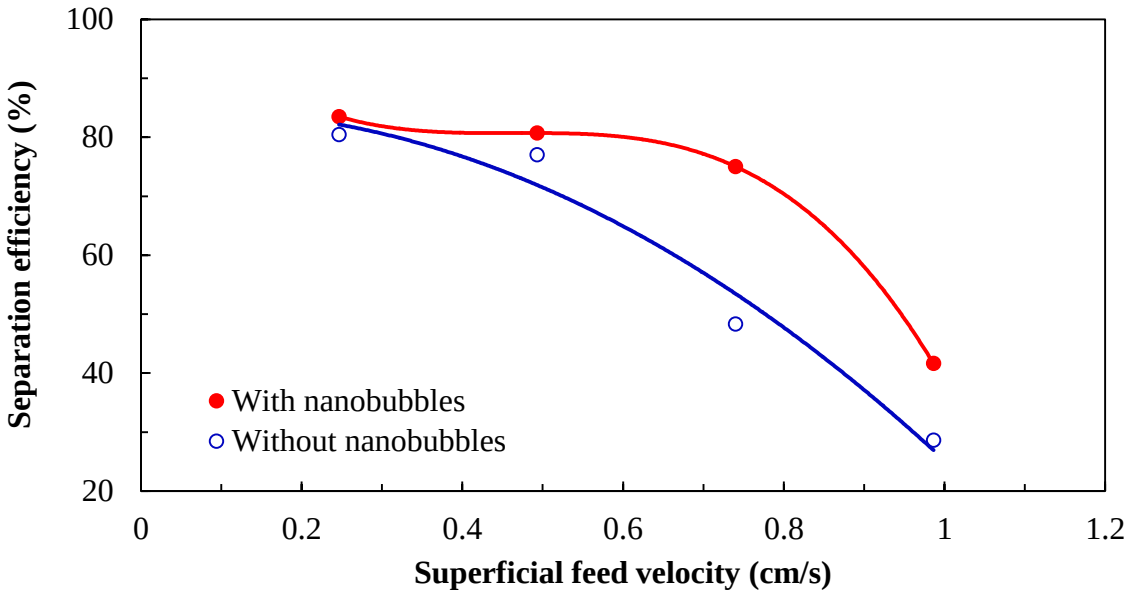

Figure 4-18. Separation efficiency vs. superficial feed velocity with and without nanobubbles in specially designed laboratory flotation column of 5.08 cm diameter.

Different superficial air velocities of 0.4, 0.8, 1.2, and 1.6 cm/s were used to investigate the influence of the superficial air velocity on flotation performance in the presence and absence of nanobubbles and the results are shown in Figure 4-19 and Figure 4-20. The flotation recovery remained essentially unchanged at a high level of approximately 95% in the presence of nanobubbles when the superficial air velocity decreased from 1.6 to 0.4

m/s. Product ash increased from 6.0% to 9.1% as superficial air velocity increased from 0.4 to 0.8 cm/s, remained unchanged as superficial air velocity increased to 1.2 cm/s, and then increased another 3% as superficial air velocity increased to 1.6 cm/s. The greater separation associated with high recovery and low product ash observed at lower superficial air velocity was believed to be the result of good selectivity of cavitation-generated nanobubbles attaching to coal particles.

Combustible recovery was much higher in the presence of nanobubbles at all superficial air velocities examined, as shown in Figure 4-19. For example, use of nanobubbles increased combustible recovery by about 50% at a superficial air velocity of 0.8 or 1.2 cm/s. The separation efficiency vs. superficial air velocity curve shown in Figure 4-20 clearly indicates that use of nanobubbles greatly improved separation performance of flotation.

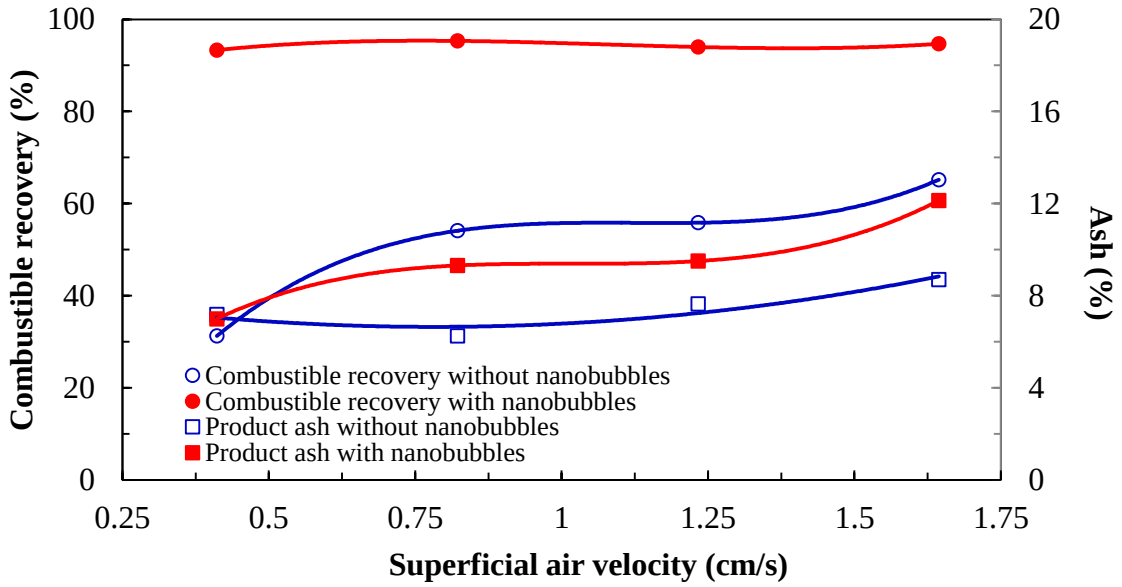

Figure 4-19. Effect of nanobubbles on the combustible recovery at varying superficial air velocities in specially designed laboratory flotation column of 5.08 cm diameter.

Figure 4-20 shows that the separation efficiency in presence of nanobubbles decreased from 80% to about 65% as superficial air velocity increased from 0.4 to 1.6 cm/s. This is because nanobubbles increased the attachment probability of the weakly hydrophobic particles by increasing their hydrophobicity, which increased the clean coal ash content from 5% to about 12% whereas combustible recovery remained essentially unchanged. The data clearly indicates that a lower superficial air velocity is preferred in the presence of nanobubbles, which reduces the air consumption and thus operating cost. The lower requirement for external air consumption in the presence of nanobubbles is a direct result of the fact that nanobubbles are produced from air naturally dissolved in water.

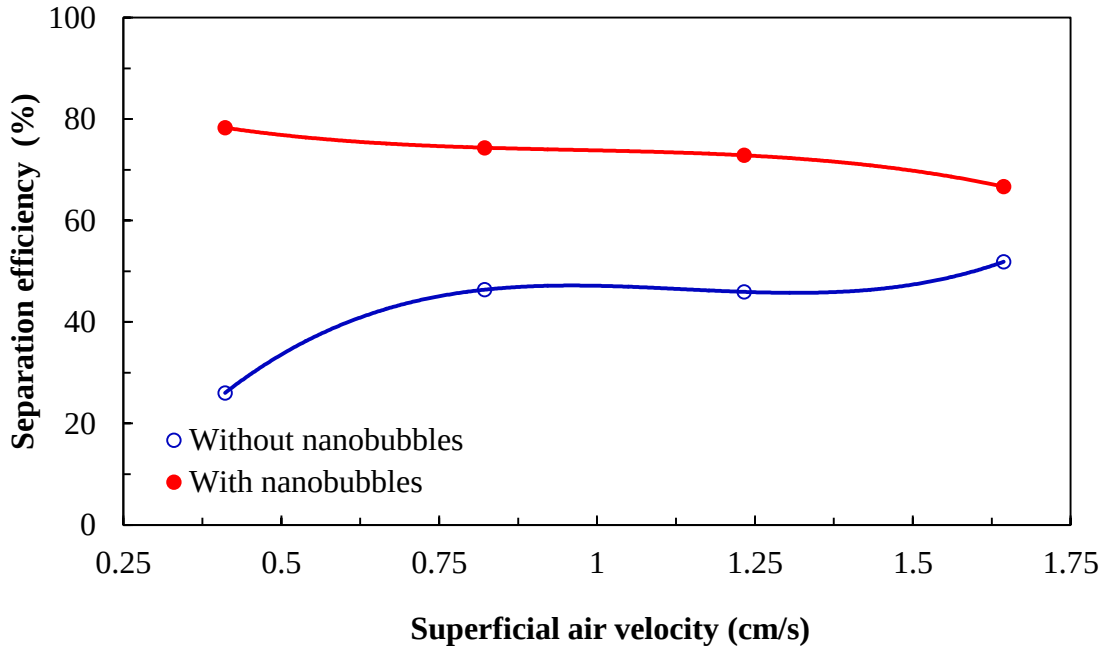

Figure 4-20. Separation efficiency vs. superficial air velocity with and without nanobubbles in specially designed laboratory flotation column of 5.08 cm diameter.

Figure 4-21 and Figure 4-22 show the influence of wash water flow rate on column flotation performance. The wash water flow rate was set at 0, 0.08, 0.16, 0.25, and 0.33 cm/s. Wash water reduced both product ash content and combustible recovery as shown

in Figure 4-21. At all superficial wash water velocities, combustible recovery was substantially higher in the presence of nanobubbles than in their absence while product ash was lower or essentially the same, which indicates once again that use of nanobubbles, improved the separation efficiency of column flotation, as confirmed in Figure 4-22, which shows that use of nanobubbles substantially increased separation efficiency.

Figure 4-23 and Figure 4-24 show flotation results obtained at 0.4 cm/s and 1.2 cm/s superficial air velocity with nanobubbles at different wash water rates. Obviously, increasing air flow rate from 0.4 cm/s to 1.2 cm/s improved combustible recovery without compromising product quality, as shown in Figure 4-23. Figure 4-24 suggests that high superficial air velocity of 1.2 cm/s improved separation efficiency at 0.16 cm/s wash water flow rate.

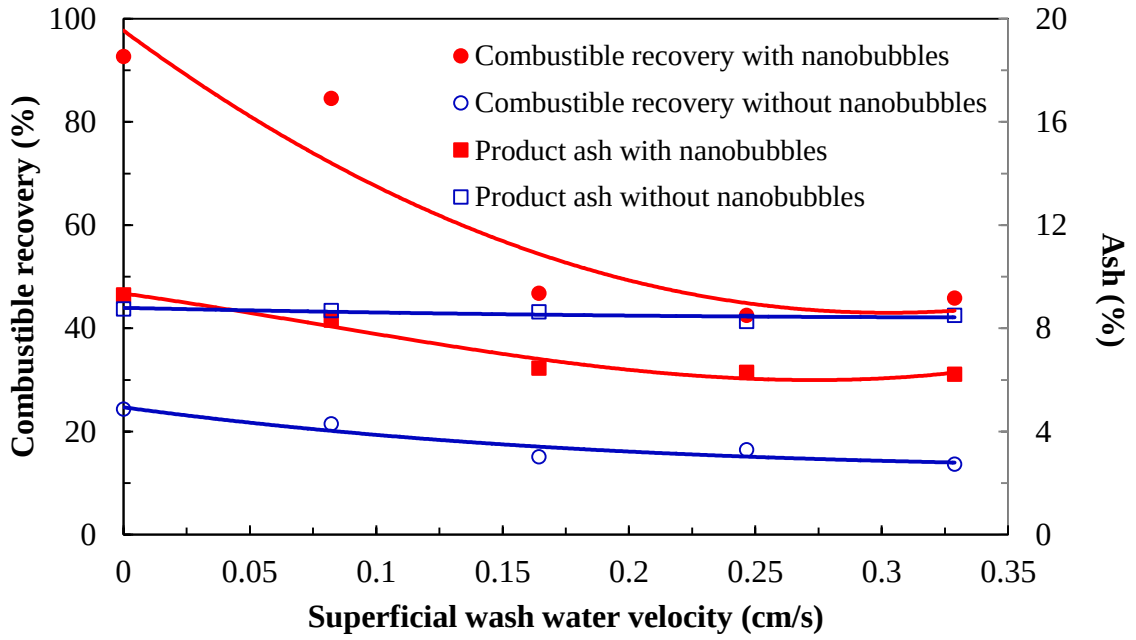

Figure 4-21. Effect of nanobubbles on the combustible recovery at varying superficial wash water velocities in specially designed laboratory flotation column of 5.08 cm diameter.

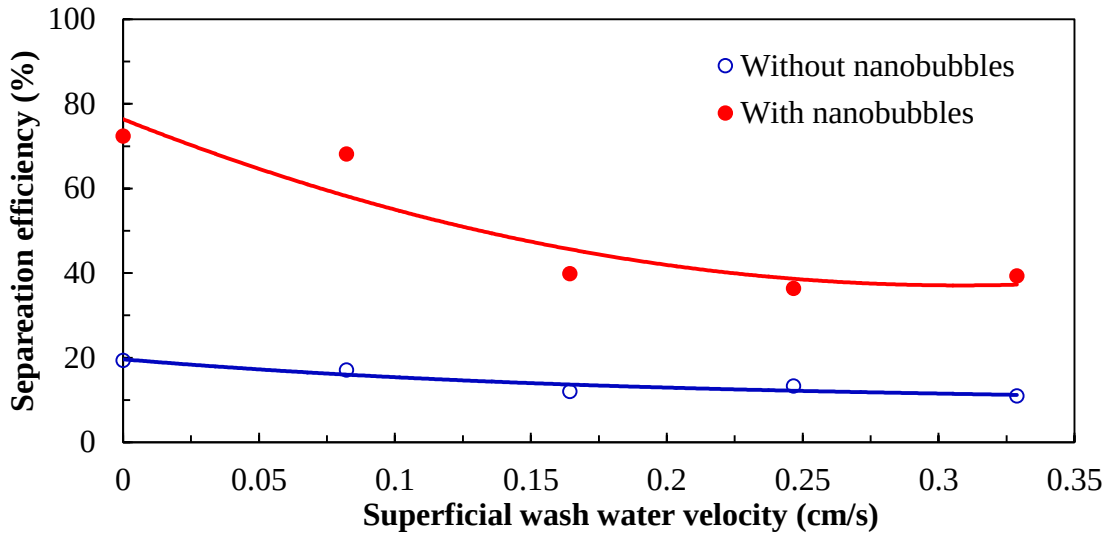

Figure 4-22. Separation efficiency vs. superficial wash water velocity with and without nanobubbles in specially designed laboratory flotation column of 5.08 cm diameter.

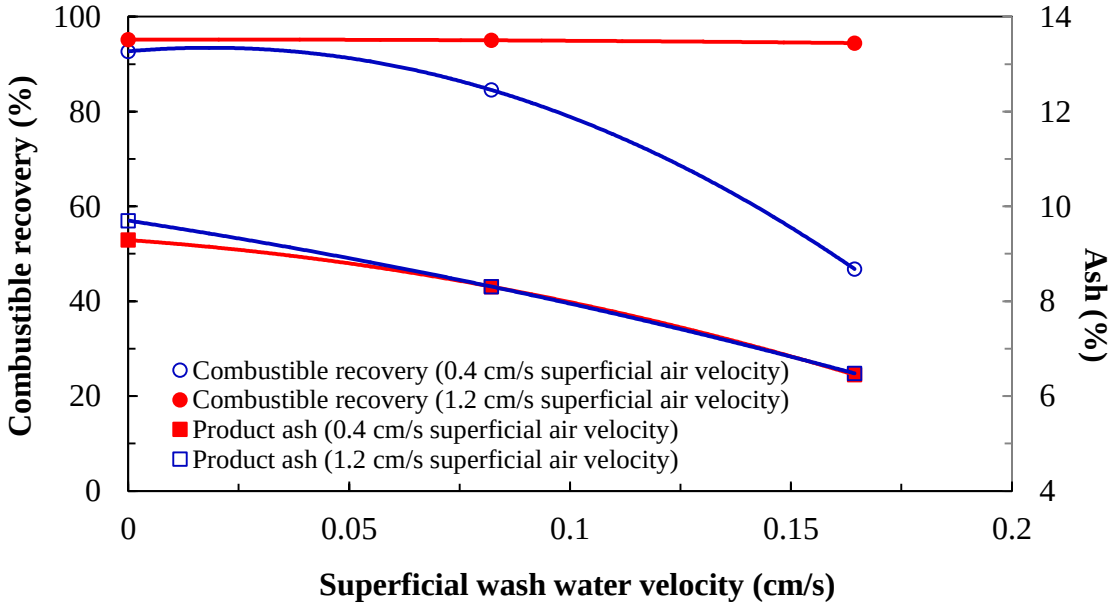

Figure 4-23. Combustible recovery and product ash vs. superficial wash water velocity with nanobubbles at 0.4 and 1.2cm/s superficial air velocity in specially designed laboratory flotation column of 5.08 cm diameter.

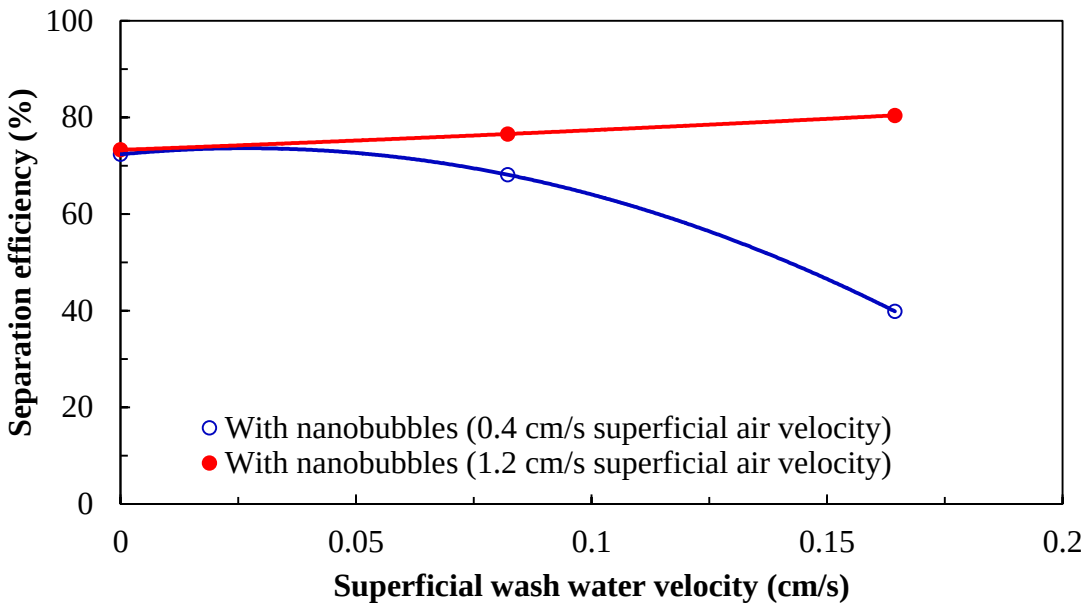

Figure 4-24. Separation efficiency vs. superficial air velocity with and without nanobubbles at 0.4 and 1.2 cm/s superficial air velocity in specially designed laboratory flotation column of 5.08 cm diameter.

4.2.2. A Size-by-Size Study of Flotation Products

A size-by-size analysis of flotation products was conducted to assess the effect of nanobubbles on coal flotation performance during laboratory nanobubble enhanced coal flotation tests. The results are shown in Figure 4-25, Figure 4-26, and Figure 4-27 for four different frother concentrations as a function of mean particle size.

Figure 4-25 shows product ash as a function of mean particle size at different frother concentrations. It can be seen that the presence of nanobubbles slightly increased the product ash content. The highest product ash content of about 11% was obtained in the finer size fraction finer than 25 µm (12.5 µm arithmetic mean particle size) in the clean coal. This is mainly because feed ash in the finer size fraction was higher (60% ash). The flotation process reduced the ash content in the size fraction of -300+75 µm (187.5 µm mean particle size) from 8% to less than 5.5% at all frother dosages. It reduced the ash

content in the size fraction of -75+25 µm (50 µm mean particle size) from about 12% to less than 6.5%.

Results shown in Figure 4-26 indicate that combustible recovery for the -25 µm and the -300+75 µm size fractions increased by 15% in the presence of nanobubbles at 30 ppm frother concentration. For the -75+25 µm size fraction, nanobubbles had minimal effects on combustible recovery, which was already very high (more than 95%) even in the absence of nanobubbles. The overall recovery was improved by about 10% at 30 ppm frother concentration and by 5% at the other frother concentrations.

Combustible recovery was higher than 95% for the -75+25 µm size fraction at all frother concentrations indicating this size fraction of coal was easy to clean even with a low concentration of frother present in the slurry. However, for the coarser size fraction, combustible recovery increased sharply as frother concentration increased from 15 ppm to about 60 ppm. For the finer -25 µm size fraction, combustible recovery increased as the frother concentration increased from 15 ppm to 30 ppm then decreased sharply as the frother concentration increased from 30 ppm to about 60 ppm.

The presence of nanobubbles significantly increased combustible recovery for the coarser (-300+75 µm) and the finer (-25 µm) particle size fractions. This may be partly because the presence of nanobubbles improved the flotation selectivity of coal particles by increasing the probability of collision and the probability of attachment and by decreasing the probability of detachment of coal particles.

Figure 4-27 shows separation efficiency curves for different size fractions at different frother concentrations. The figure indicates once again that use of nanobubbles improved significantly the separation efficiency of the flotation process of relatively coarse and fine size fractions. This means that the presence of nanobubbles increased the flotation particle size range by increasing the upper size limit and by reducing the lower particle size limit.

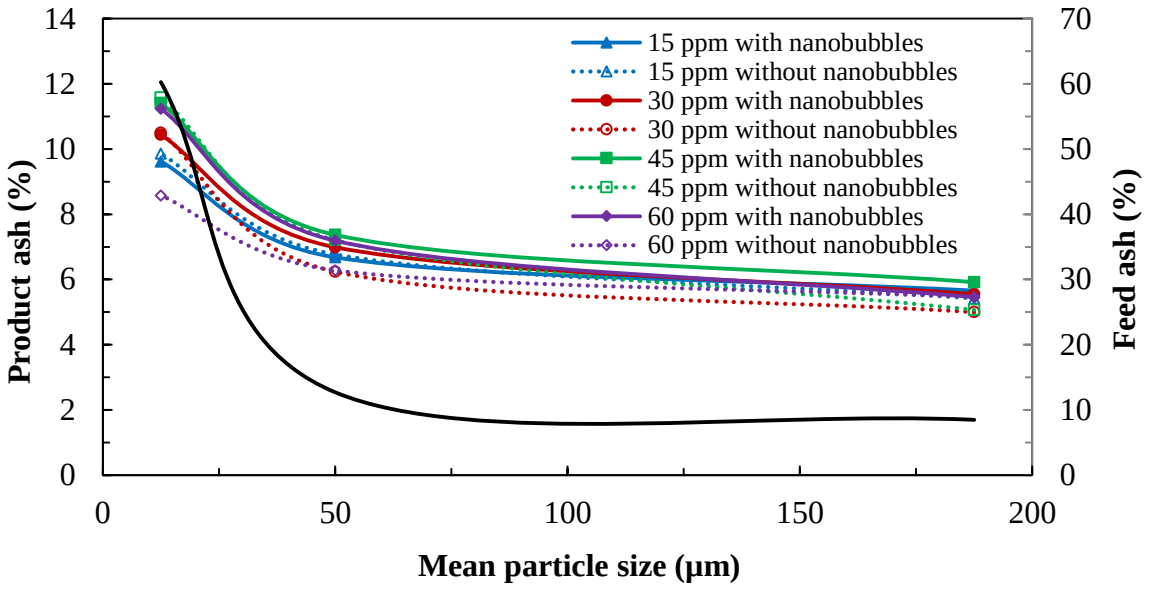

Figure 4-25. Product ash vs. mean particle size with and without nanobubbles for different frother concentrations in specially designed laboratory flotation column of 5.08 cm diameter.

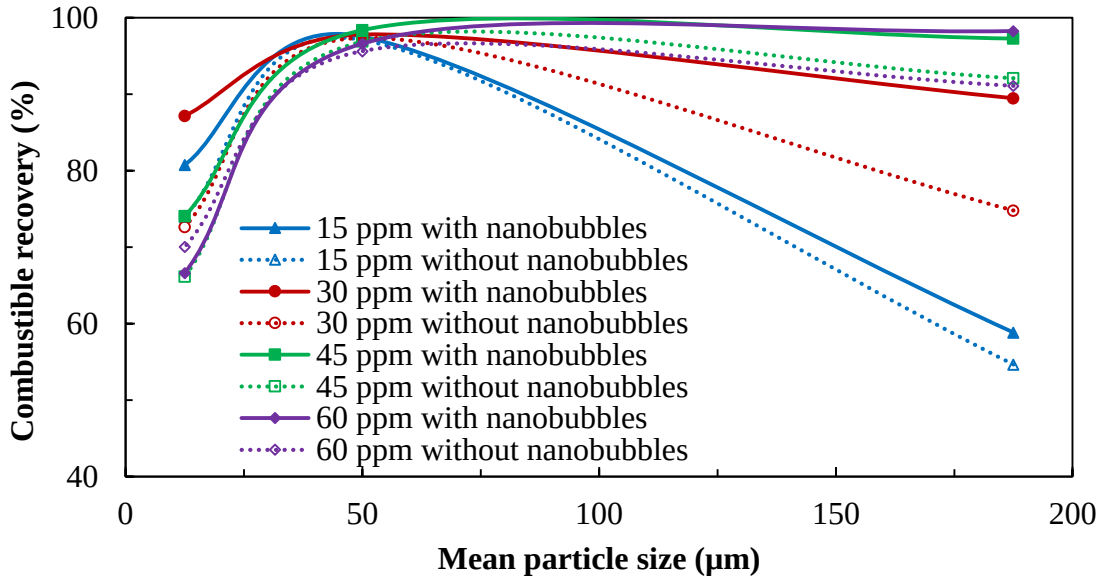

Figure 4-26. Combustible recovery vs. mean particle size with and without nanobubbles for different frother concentrations in specially designed laboratory flotation column of 5.08 cm diameter.

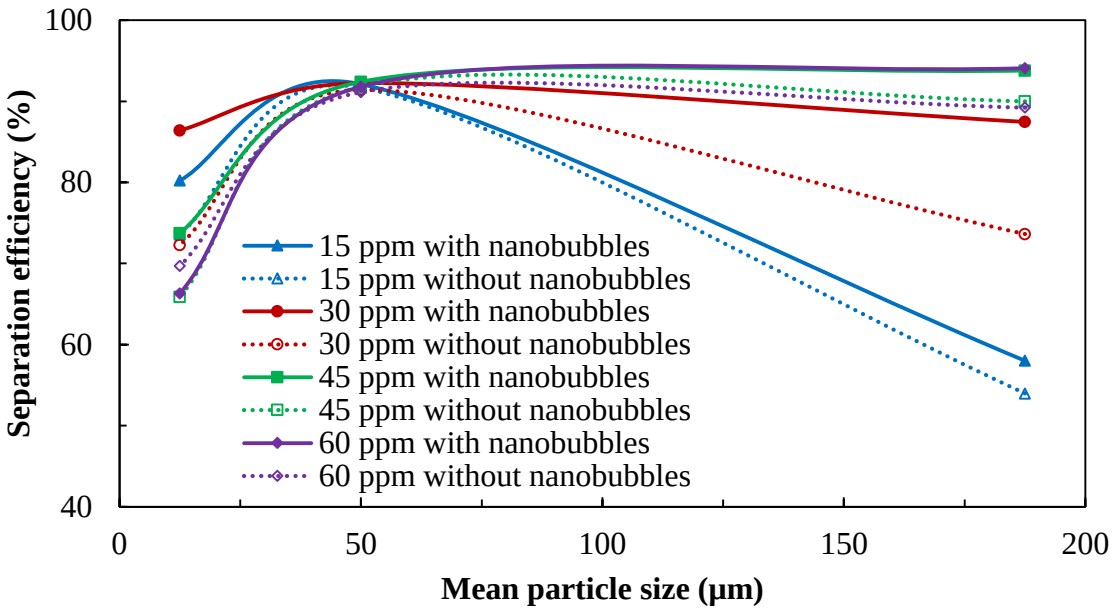

Figure 4-27. Separation efficiency vs. mean particle size with and without nanobubbles for different frother concentrations in specially designed laboratory flotation column of 5.08 cm diameter.

4.2.3. Comparison of Column Flotation Performance with Release Analysis

Figure 4-28 and Figure 4-29 show the effect of nanobubbles on combustible recovery as a function of ash rejection at a collector dosage of 0.49 kg/ton, frother concentration of 30 ppm, superficial wash water flow rate of 0.41 cm/s, and feed slurry solids concentration of 7%. The results in Figure 4-28 were generated by changing superficial slurry feed velocities from 0.25 cm/s to 1.23 cm/s while data for Figure 4-29 were generated by changing superficial gas velocities from 0.4 cm/s to 1.6 cm/s. By comparing these combustible recovery data generated in the presence and absence of nanobubbles with the release analysis curve, it can be clearly seen that the flotation combustible recovery produced with nanobubbles was much higher than without nanobubbles and in general the data points generated in the presence of nanobubbles were closer to the release analysis curve.

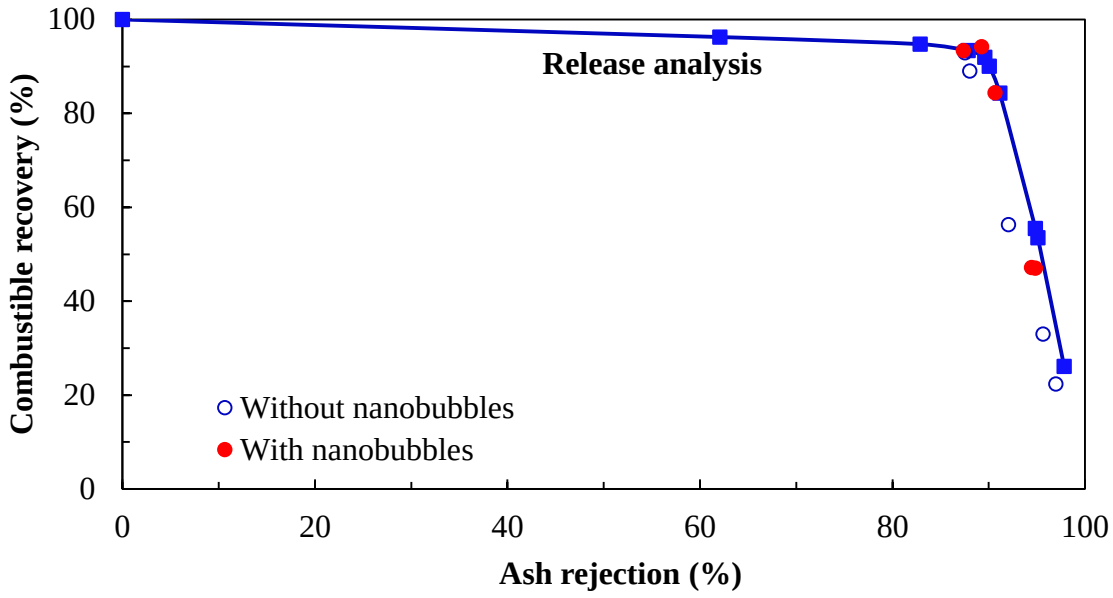

Figure 4-28. Performance comparison of specially designed laboratory flotation column of 5.08 cm diameter with and without nanobubbles at different superficial feed slurry velocities to release analysis curve.

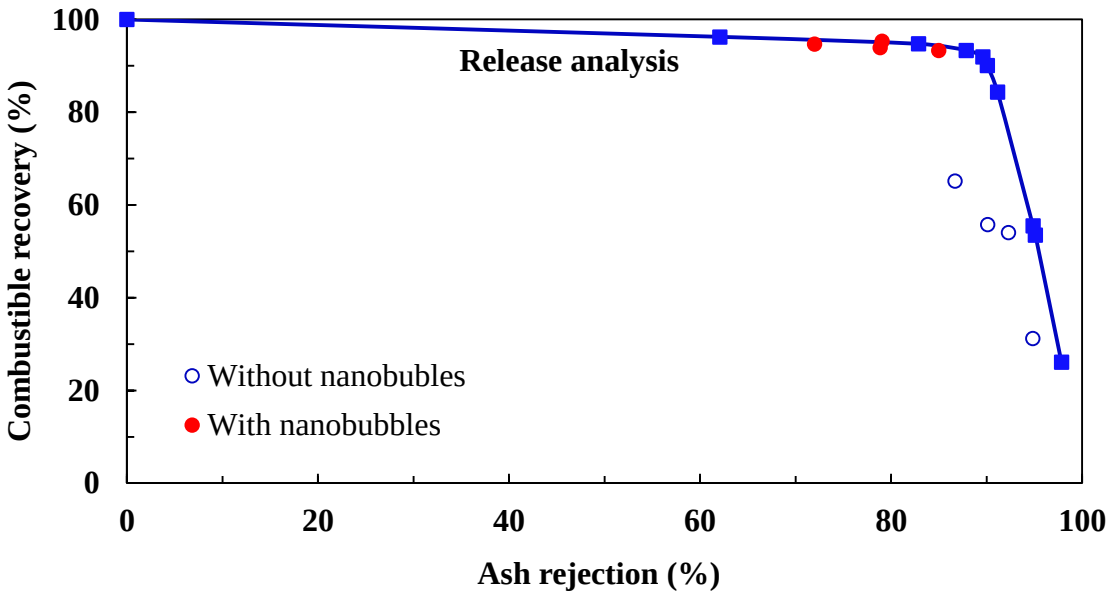

Figure 4-29. Performance comparison of specially designed laboratory flotation column of 5.08 cm diameter with and without nanobubbles at different superficial air velocities to release analysis curve.

4.3. MECHANICAL FLOTATION EXPERIMENTS

A three compartment Hazen Quinn (H-Q) conventional flotation cell with cavitation tube was used to investigate the benefit of nanobubbles on the conventional mechanical flotation process. The total volume of the H-Q conventional flotation cell is 31 liters. The effect of nanobubbles on mechanical flotation was investigated under the following different process parameters: frother concentration, collector dosage, flow rate to cavitation tube, feed solid concentration, and feed flow rate. Baseline data were established from a kinetic flotation test using a 5-liter Denver flotation cell.

Frother concentration had a positive and significant effect on combustible recovery as shown in Figure 4-30 while the product ash was stable at 9%. Combustible recovery increased from 50% to 75% as frother concentration increased from 10 ppm to 40 ppm. The combustible recovery vs. product ash curve with nanobubbles is compared to the baseline data curve without nanobubbles in Figure 4-31. The separation efficiency vs. frother concentration relationship is shown in Figure 4-32 which shows that the highest separation efficiency was at 40 ppm frother concentration.

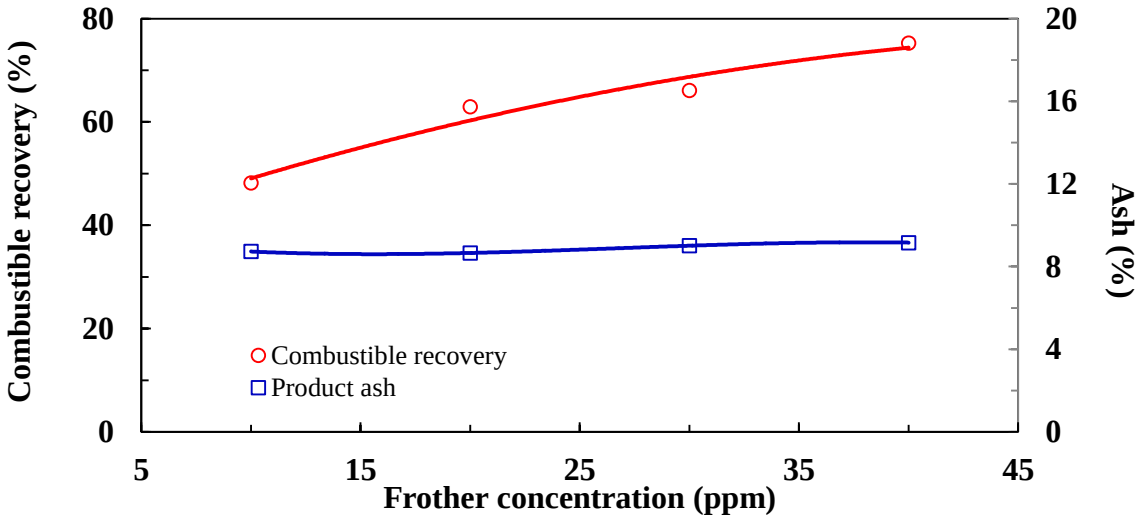

Figure 4-30. Effect of frother concentration on combustible recovery and product ash content in a bank of three compartment Hazen Quinn (H-Q) conventional flotation cells with nanobubbles.

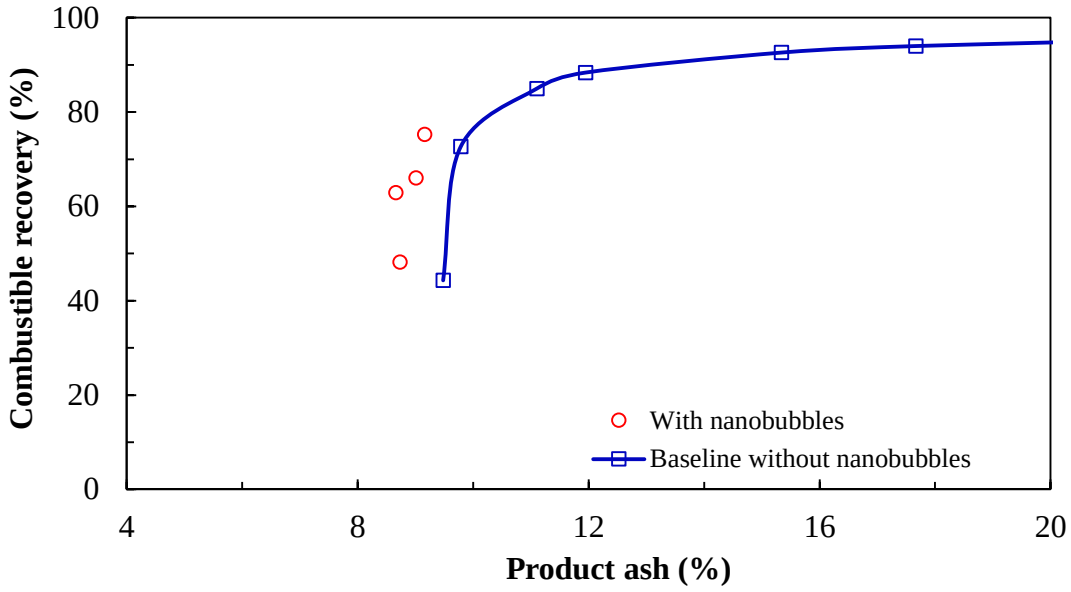

Figure 4-31. Performance Comparison of a bank of three compartment Hazen Quinn (H-Q) conventional flotation cells with nanobubbles at different frother concentrations to baseline data established from a kinetic flotation test using a 5-liter Denver flotation cell.

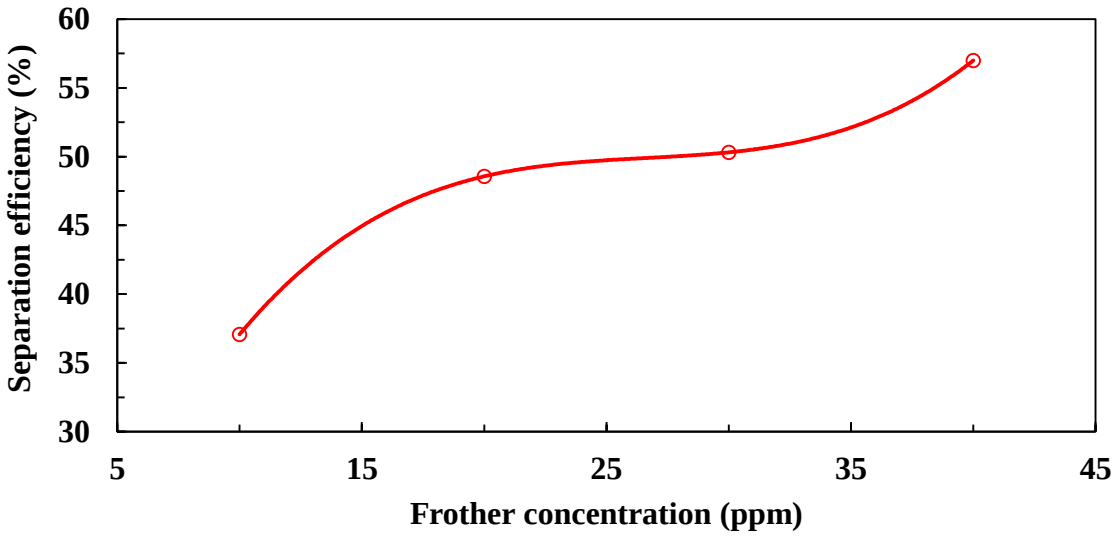

Figure 4-32. Effect of frother concentration on separation efficiency of a bank of three compartment Hazen Quinn (H-Q) conventional flotation cells with nanobubbles.

As collector dosage increased from 0.1 kg/ton to 0.9 kg/ton, combustible recovery increased from 45% to 70% as shown in Figure 4-33. Figure 4-34 shows the separation efficiency curve at different collector dosages. Figure 4-35 compares the combustible recovery vs. product ash curve with nanobubbles to the base line data without nanobubbles.

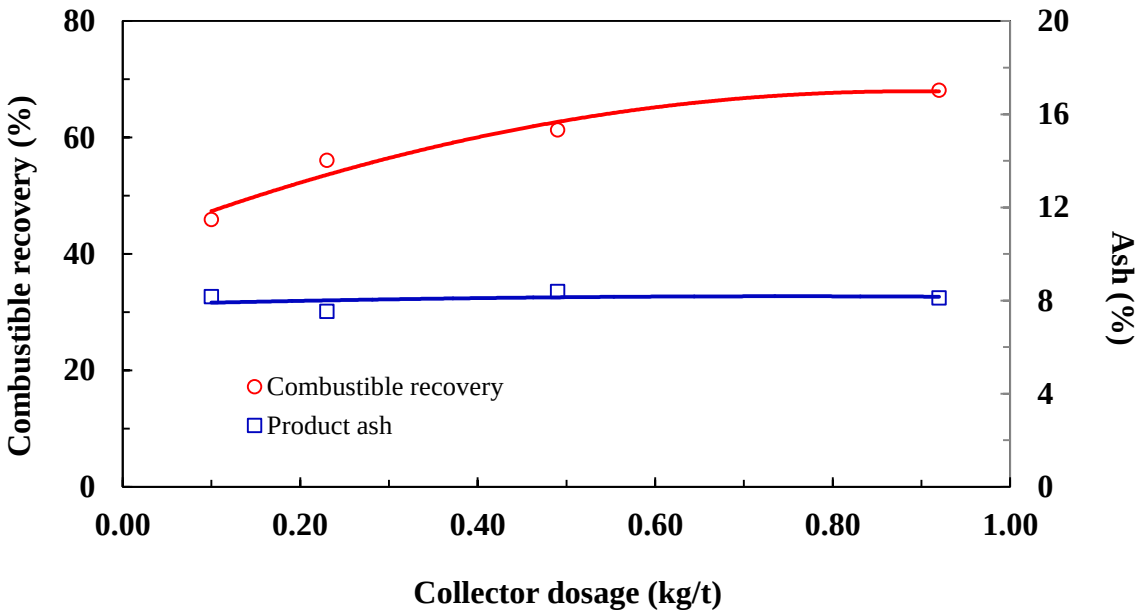

Figure 4-33. Effect of collector dosage on combustible recovery and product ash content in a bank of three compartment Hazen Quinn (H-Q) conventional flotation cells with nanobubbles.

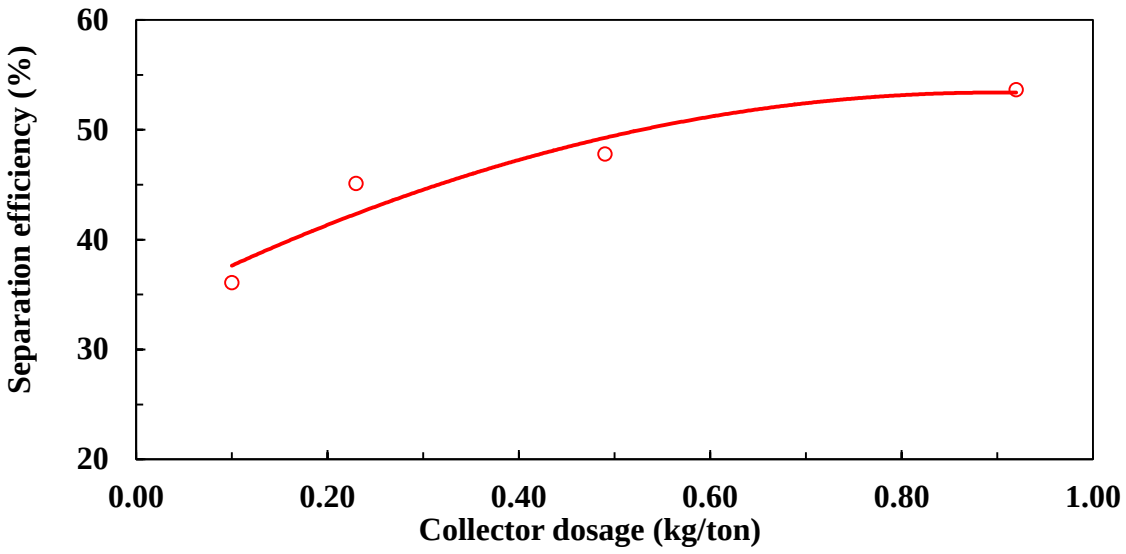

Figure 4-34. Effect of collector dosage on separation efficiency of a bank of three compartment Hazen Quinn (H-Q) conventional flotation cells with nanobubbles.

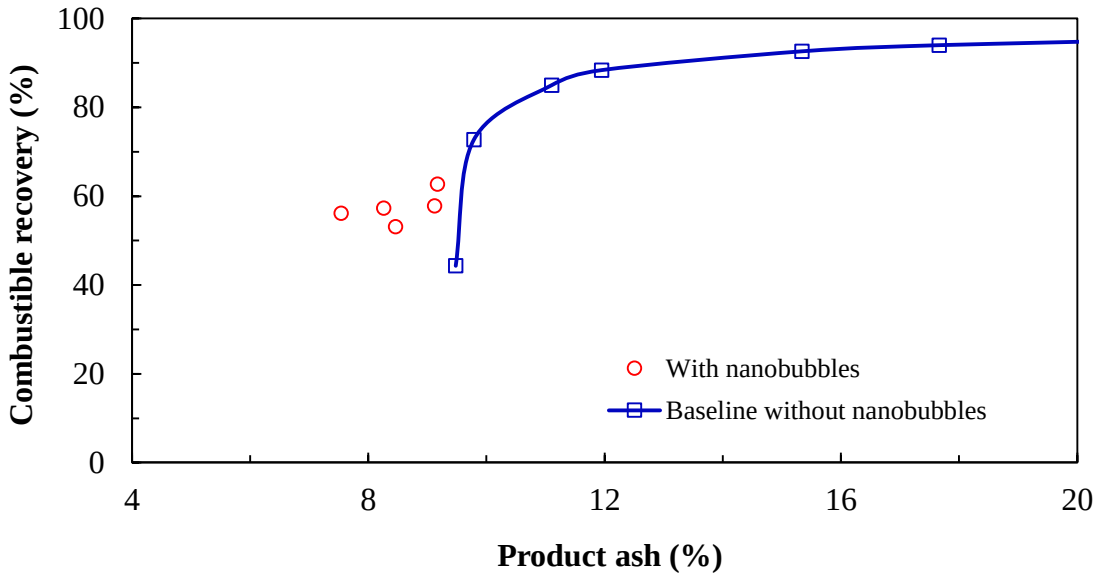

Figure 4-35. Performance Comparison of a bank of three compartment Hazen Quinn (H-Q) conventional flotation cells with nanobubbles at different collector dosages to baseline data established from a kinetic flotation test using a 5-liter Denver flotation cell.

To investigate the influence flow rate to the cavitation tube on flotation performance, cavitation tube flow rates of 2000 ml/min, 4000 ml/min, 6000 ml/min, and 8000 ml/min were evaluated. As flow rate increased from 2000 ml/min to 8000 ml/min, combustible recovery increased from 55% to 68% as shown in Figure 4-36. Also, product ash increased from 8% to 10%. Figure 4-37 shows the separation efficiency curve at different flow rates to the cavitation tube. Figure 4-38 compares the combustible recovery vs. product ash curve with nanobubbles to baseline data without nanobubbles.

Solids concentration has modest influence on flotation performance. Figure 4-39 and Figure 4-40 show that the best solids concentration is about 15%. Figure 4-41 compares the combustible recovery vs. product ash curve with nanobubbles to baseline data without nanobubbles.

From Figure 4-42 and Figure 4-43, it can be seen that higher feed rates produced lower combustible recovery and product ash. Figure 4-44 shows that combustible recovery of about 89% was obtained at about 10% product ash and 80% ash rejection.

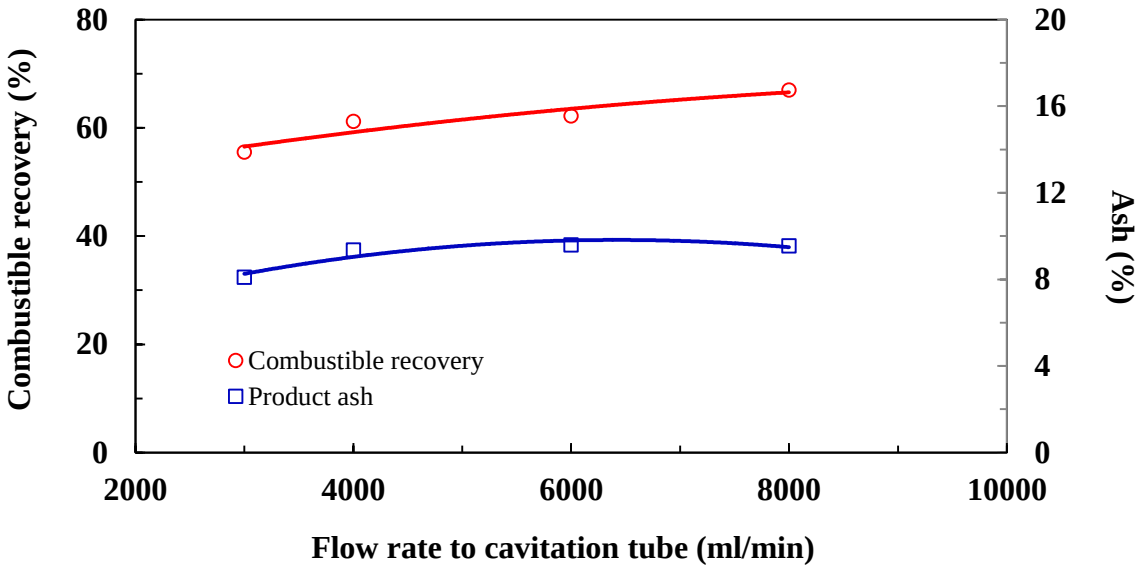

Figure 4-36. Effect of flow rate to cavitation tube on combustible recovery and product ash content in a bank of three compartment Hazen Quinn (H-Q) conventional flotation cells.

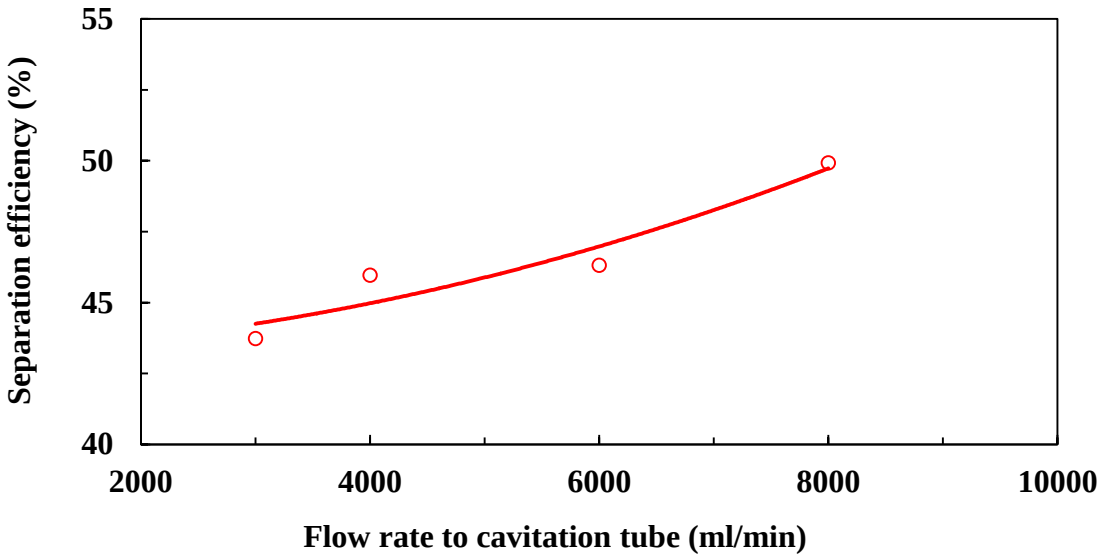

Figure 4-37. Effect of flow rate to cavitation tube on separation efficiency of a bank of three compartment Hazen Quinn (H-Q) conventional flotation cells with nanobubbles.

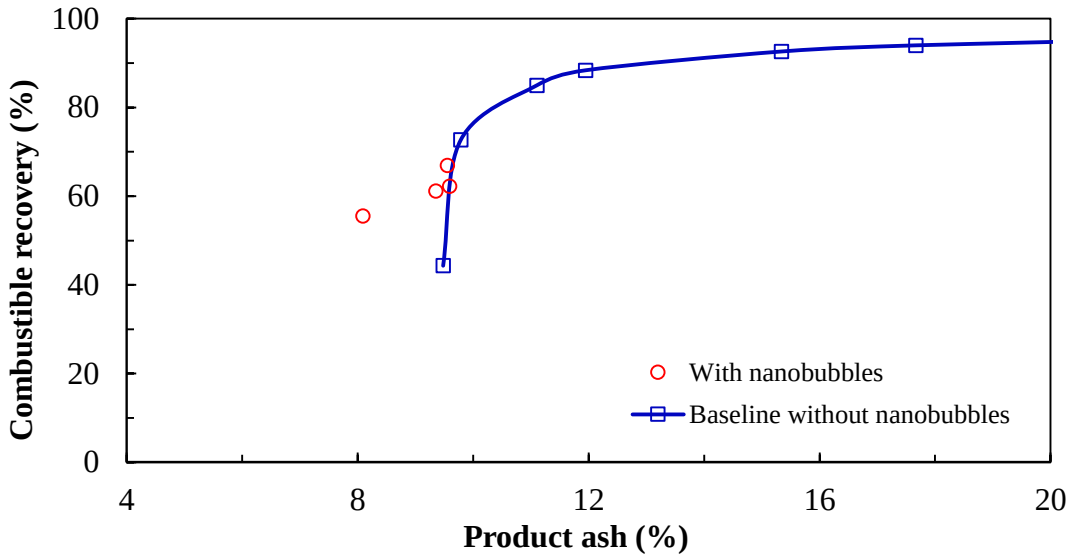

Figure 4-38. Performance Comparison of a bank of three compartment Hazen Quinn (H-Q) conventional flotation cells at different cavitation flow rates to baseline data established from a kinetic flotation test using a 5-liter Denver flotation cell.

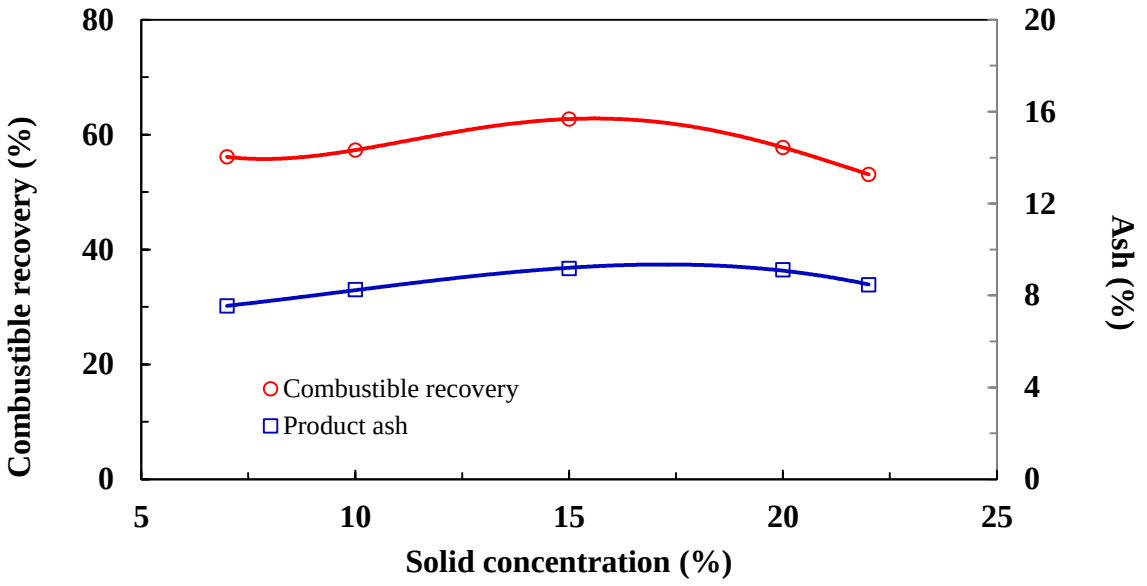

Figure 4-39. Effect of feed solids concentration on combustible recovery and product ash content in a bank of three compartment Hazen Quinn (H-Q) conventional flotation cells with nanobubbles.

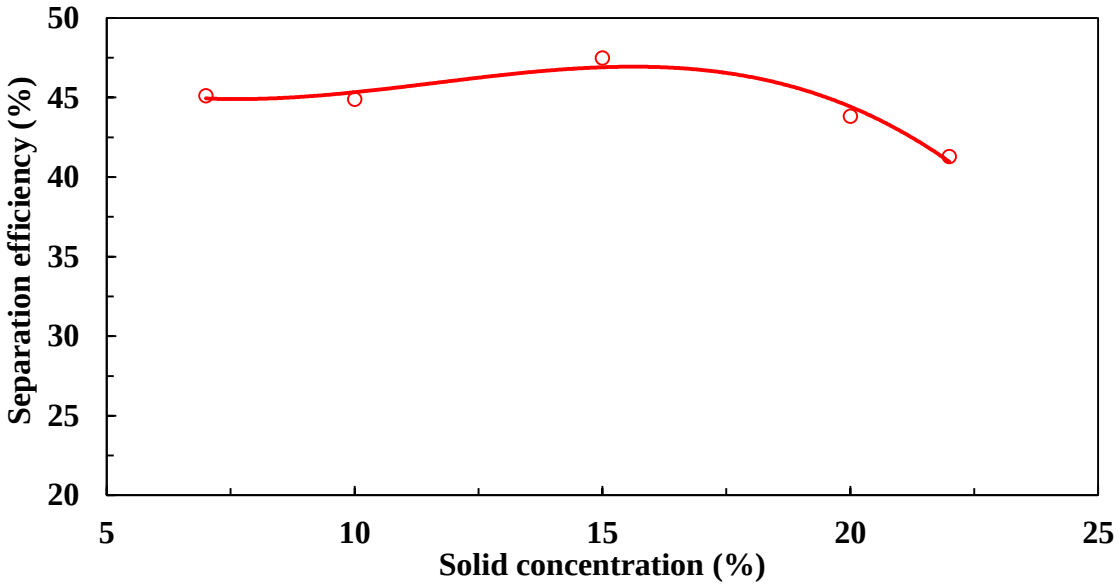

Figure 4-40. Effect of solids concentration on separation efficiency of a bank of three compartment Hazen Quinn (H-Q) conventional flotation cells with nanobubbles.

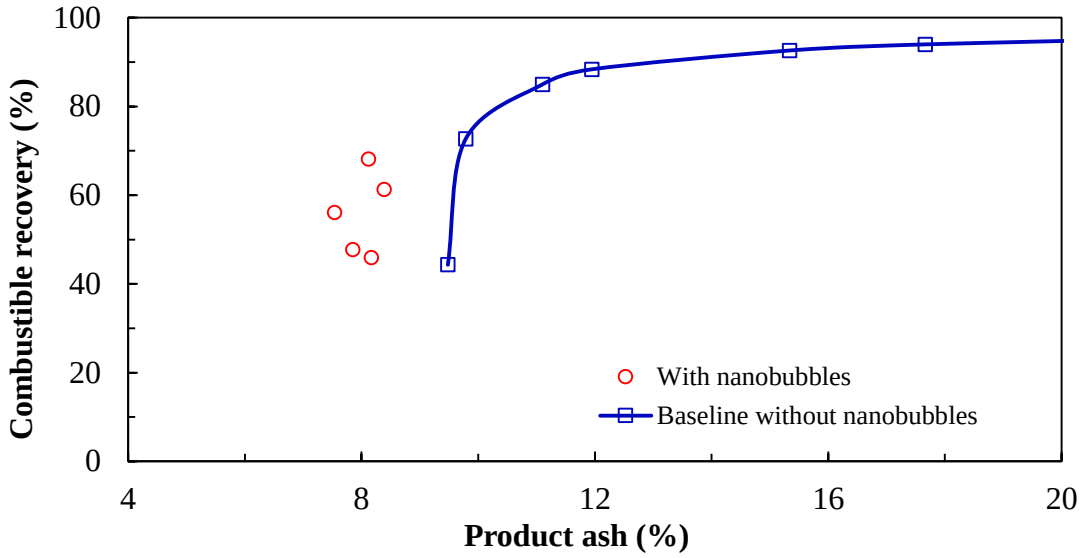

Figure 4-41. Performance Comparison of a bank of three compartment Hazen Quinn (H-Q) conventional flotation cells with nanobubbles at different feed solids concentrations to baseline data established from a kinetic flotation test using a 5-liter Denver flotation cell.

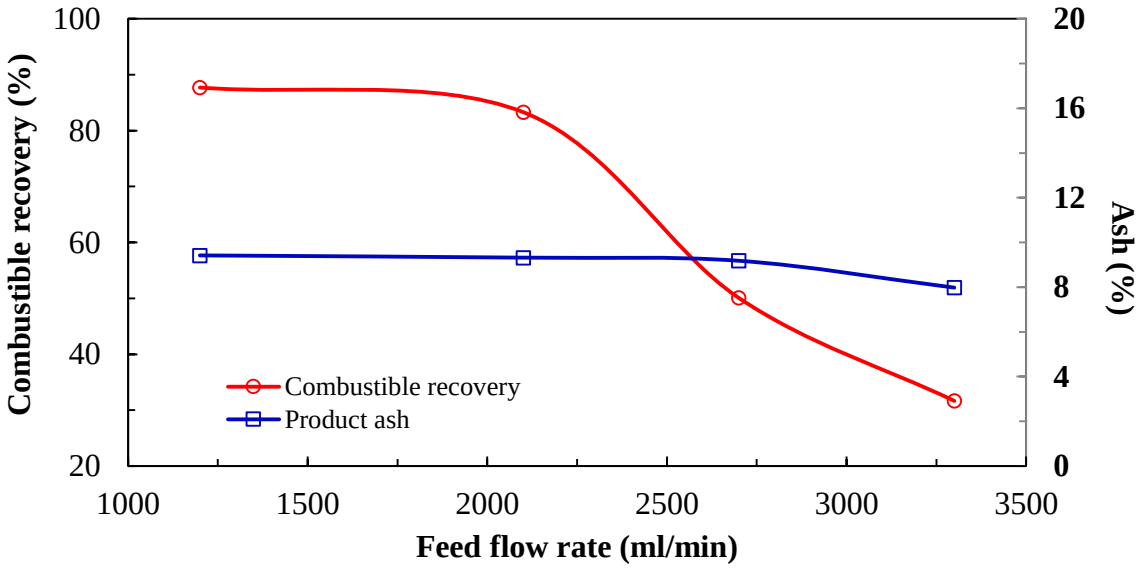

Figure 4-42. Effect of feed flow rate on combustible recovery and product ash content in a bank of three compartment Hazen Quinn (H-Q) conventional flotation cells with nanobubbles.

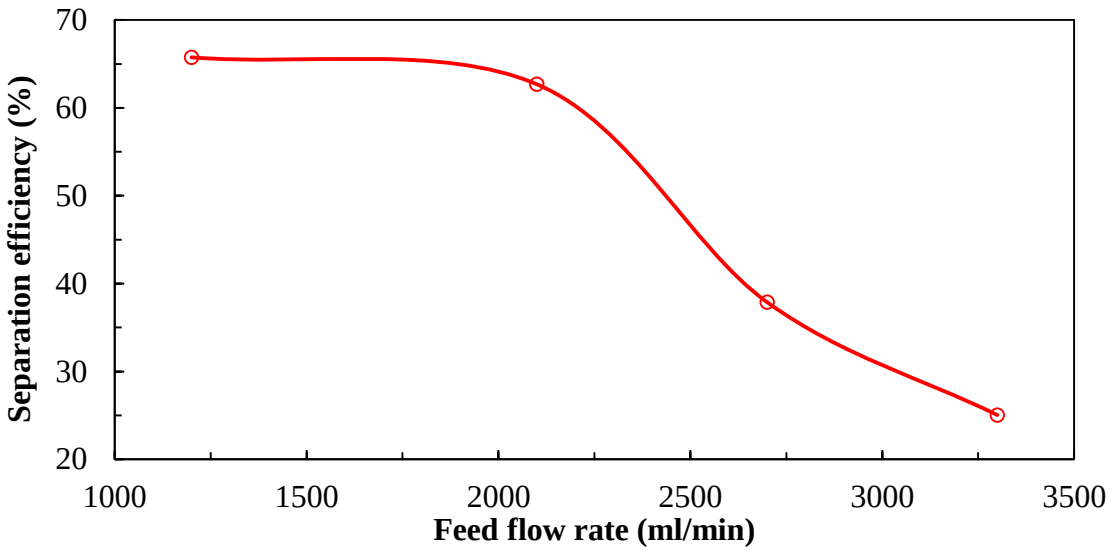

Figure 4-43. Effect of feed flow rate on separation efficiency of a bank of three compartment Hazen Quinn (H-Q) conventional flotation cells with nanobubbles.

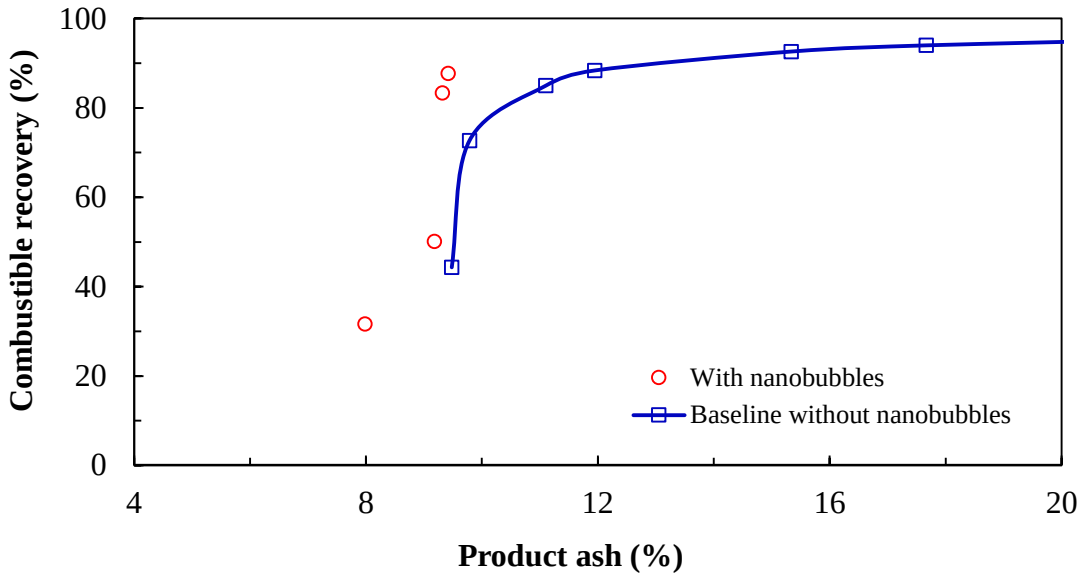

Figure 4-44. Performance Comparison of a bank of three compartment Hazen Quinn (H-Q) conventional flotation cells with nanobubbles at different feed flow rates to baseline data established from a kinetic flotation test using a 5-liter Denver flotation cell.

4.4. FUNDAMENTAL CHARACTERIZATION OF NANOBUBBLES

4.4.1. Nanobubbles Size Distribution and Stability

The nanobubbles generated by hydrodynamic cavitation process in water solution are nanoscopic sized bubbles and their size distribution was measured three times with the results are shown in Figure 4-45. The cumulative curve shows that 10%, 50% and 90% are smaller than 250 nm, 600 nm and 1000 nm, respectively.

A conventional sized bubble (e.g., 1 mm in diameter) quickly rises to the surface of the slurry and collapse. It was confirmed in this study that nanobubbles were very stable in the liquid for several minutes, hours or days without noticeable change in the diameter without being affected by buoyancy, as shown in Figure 4-46 and Figure 4-47. The bubble size distribution as a function of time is shown in Figure 4-46. Figure 4-47 shows the average bubble diameter (d_{50}) is stable at about 700 nm for more than 20 min. Cho et al. (2005) found that the effective diameter of the nanobubbles generated by ultrasonic in pure water was maintained at 750 nm without significant change within one hour. Nanobubbles can stay suspended in the water, agitated by Brownian motion, which creates a presumably random motion for nanobubbles in a liquid as a result of their collision with the surrounding water molecules as illustrated in Figure 4-48. The water molecules move constantly, randomly, freely, in all directions. The random motion of the water molecules forces the nanobubbles to move in a zigzag direction without reporting to the top of the liquid medium. Furthermore, there is an electric double layer repulsion between the surfaces of the nanobubbles that inhibits their coalescence and further growth (Ushikubo et al., 2010). The presence of electrical charges could be related to a hard hydrogen bond at the gas/liquid interface that has a difference structure from that of the bulk water. The change in the hydrogen bond was detected by infrared spectroscopy (Ohgaki et al., 2010). Ushikubo et al. (2010) found that the nanobubble size distribution was in the range of a few hundred nanometers in diameter and these nanobubbles were stable for less than one day, in case of air bubbles, to some days, in the case of oxygen

bubbles. In summary, nanobubbles are formed from dissolved air or dissolved oxygen in the liquid and they persist as tracer elements, moving with the liquid.

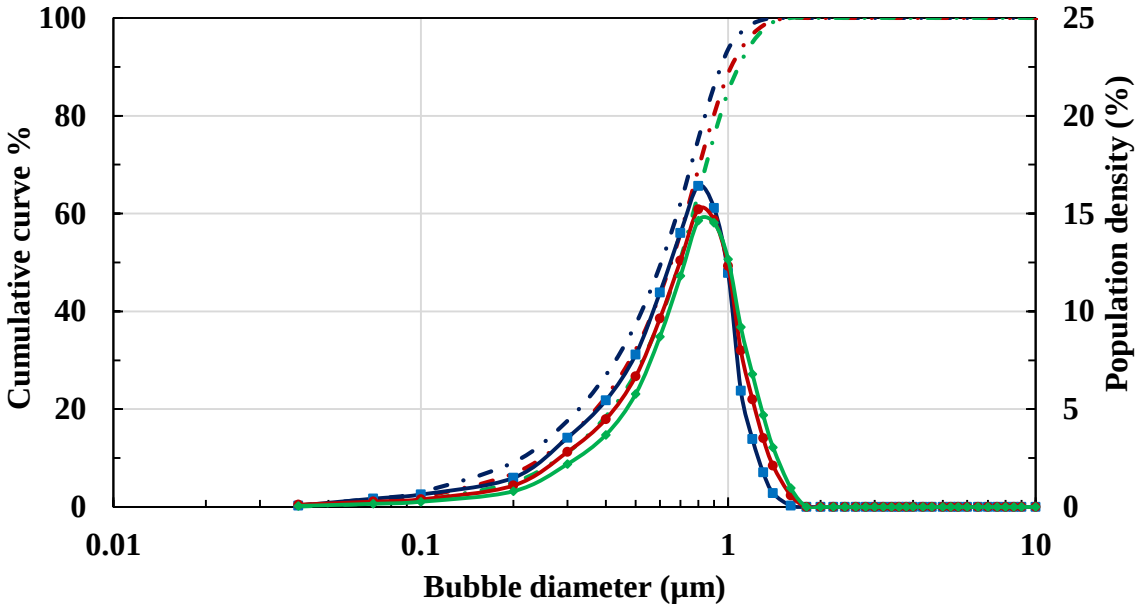

Figure 4-45. The size distribution curve for the bubble once generated by hydrodynamic cavitation in water solution of 10 ppm MIBC frother and without air.

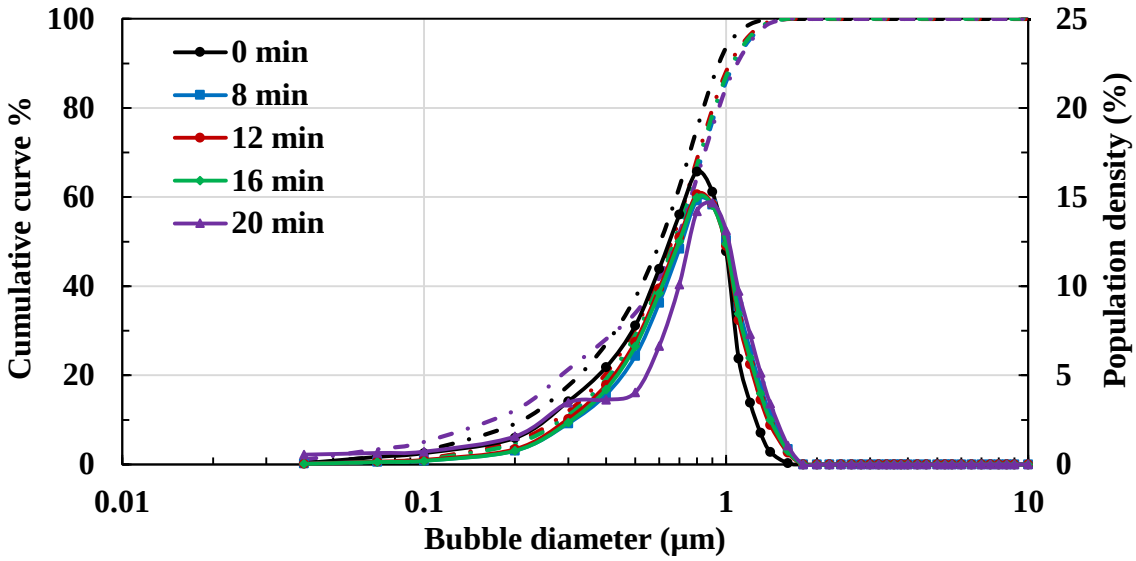

Figure 4-46. Change of bubble size distribution as a function of time in water with 10 ppm MIBC and without air after stopping the generation process of the nanobubbles.

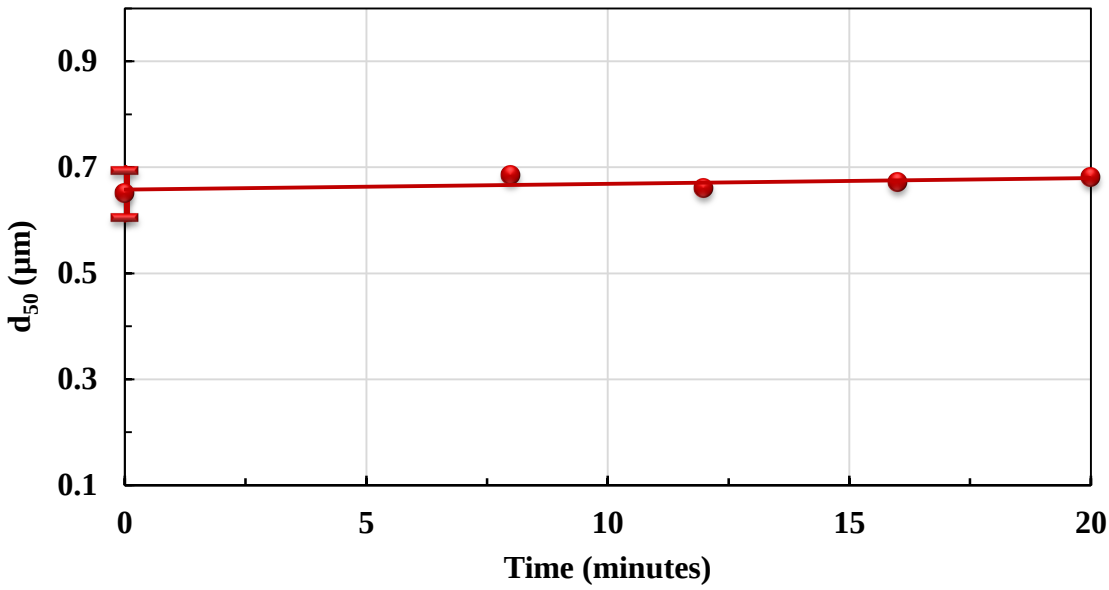

Figure 4-47. Change of average bubble diameter (d_{50}) as a function of time in water with 10 ppm MIBC and without air after stopping the generation process of the nanobubbles.

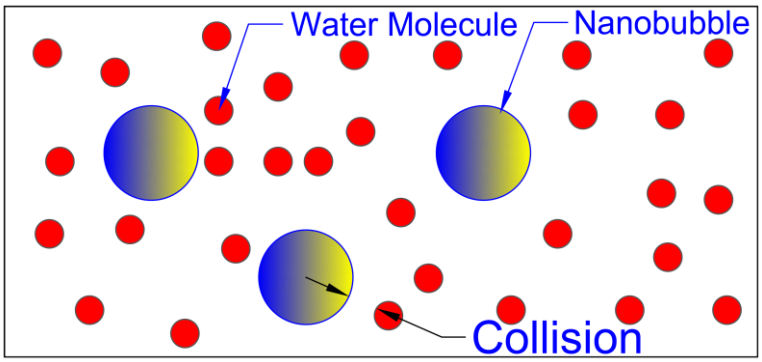

Figure 4-48. Illustration of Brownian motion of nanobubbles in a liquid as a result of its collision with water molecules (Ibe, 2013).

4.5. FUNDAMENTAL STUDIES OF ROLE OF NANOBUBBLES

4.5.1. Particle-Bubble Interaction

Froth flotation is a separation process in which bubble-particle interaction plays a vital role. Air bubbles are used as carriers to capture hydrophobic particles selectively from a complex slurry. Factors such as bubble diameter, particle diameter, particle density and particle hydrophobicity are significant parameters controlling particle-bubble interaction.

Particle-bubble interactions consist of several physicochemical and hydrodynamic phenomena in the flotation system. Most of these phenomena have been addressed extensively by the others (Jameson, Nam and Young, 1977; Schulze, 1989 and Naguyen, 1999), but the direct measurement of the particle-bubble interactions is necessary in the presence and absence of nanobubbles on the particle surface to better understand the effect of the nanobubbles on some of these phenomena. The experimental setup used in this study allows direct observation of the particle-bubble interaction including collision, sliding, adhesion and detachment in the presence and absence of the nanobubbles generated on the particles of different degrees of hydrophobicity. The method has also been found to be successful for estimating the induction time (t_i) which can't be

calculated directly by conducting the Hallimond tube flotation that allows only efficiencies or probabilities to be estimated.

A schematic illustration of particle-bubble collision, attachment and detachment is shown in Figure 4-49. The particles within the cross section area defined by limiting radius (R_c) and limiting polar position (ϕ_c) have the chance to colloid with the bubble. On the other hand, the particles outside this limiting area follow the streamlines around the bubble surface with no chance of touching the bubble. Furthermore, only the particle that colloids at a polar position of ϕ_{cr} and within the limiting cross section area of radius R_{cr} has the chance to become attached to the bubble surface. For the attachment to take place, the induction time (t_i) should be shorter than the sliding contact time (t_s).

The present experiments were focused on visualization of the particle-bubble interaction in a stationary deionized water. The interaction events were very fast, in the order of milliseconds and a system of high-speed video recording on a micrometer scale was necessary to study these events. The videos recorded during the particle-bubble approach showed a rapid change in the particle-bubble radial distance (h) and polar position (ϕ) in milliseconds. The radial distance was used to identify three distinct regimes of the particle motion around a bubble surface. Before particle-bubble collision, the particle changes its radial distance (h) quickly where the particle moves in the bulk liquid phase. After collision, as the particle moves on the bubble surface, the radial distance changes slightly as a result of thinning of the intervening water film between the particle and the bubble. If the particle is sufficiently hydrophobic, film rupture and expansion of the three-phase contact take place, resulting in a rapid change in the radial distance. The particle moves with almost a constant radial distance after producing a stable three-phase contact. No film rupture or attachment occurs to hydrophilic or very weakly hydrophobic particles.

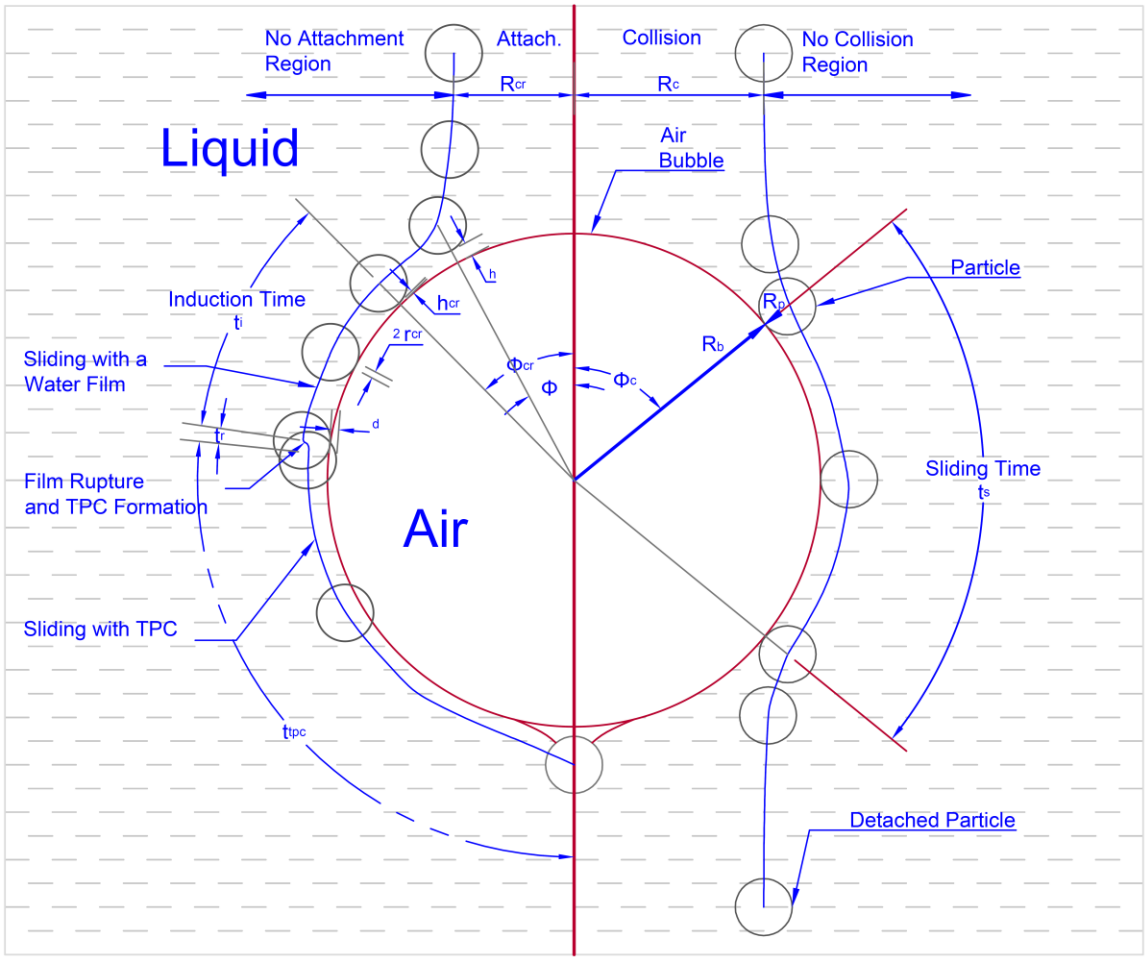

Figure 4-49. Schematic showing particle-bubble collision, attachment and detachment in froth flotation.

Nanobubble coated particles form aggregates and in consequence enhance particle bubble collisions by increasing the limiting collision area as a result of penetrating the water stream lines around the bubbles. Ishida, Kusaka and Ushijima (2012); Zhang, Kumar and Scales (2011) found that bridging of nanobubbles is responsible for the long-range (up to 500 nm) hydrophobic attractive force. Ishida, Kusaka and Ushijima (2012) found also that there is an additional attractive force (short range < 20 nm) larger than the van der Waals attraction between the hydrophobic particles in the absence of the nanobubbles. Figure 4-50 shows that hydrophobic particle aggregates have a higher attachment probability than that of a single particle. This may be a result of faster thinning of the

water layer between particle and the bubble surface with the aggregate, which flips around the particles that are attached to the bubble surface. It has been observed that this rotation phenomenon of aggregates is a fast process and facilitates water film penetration.

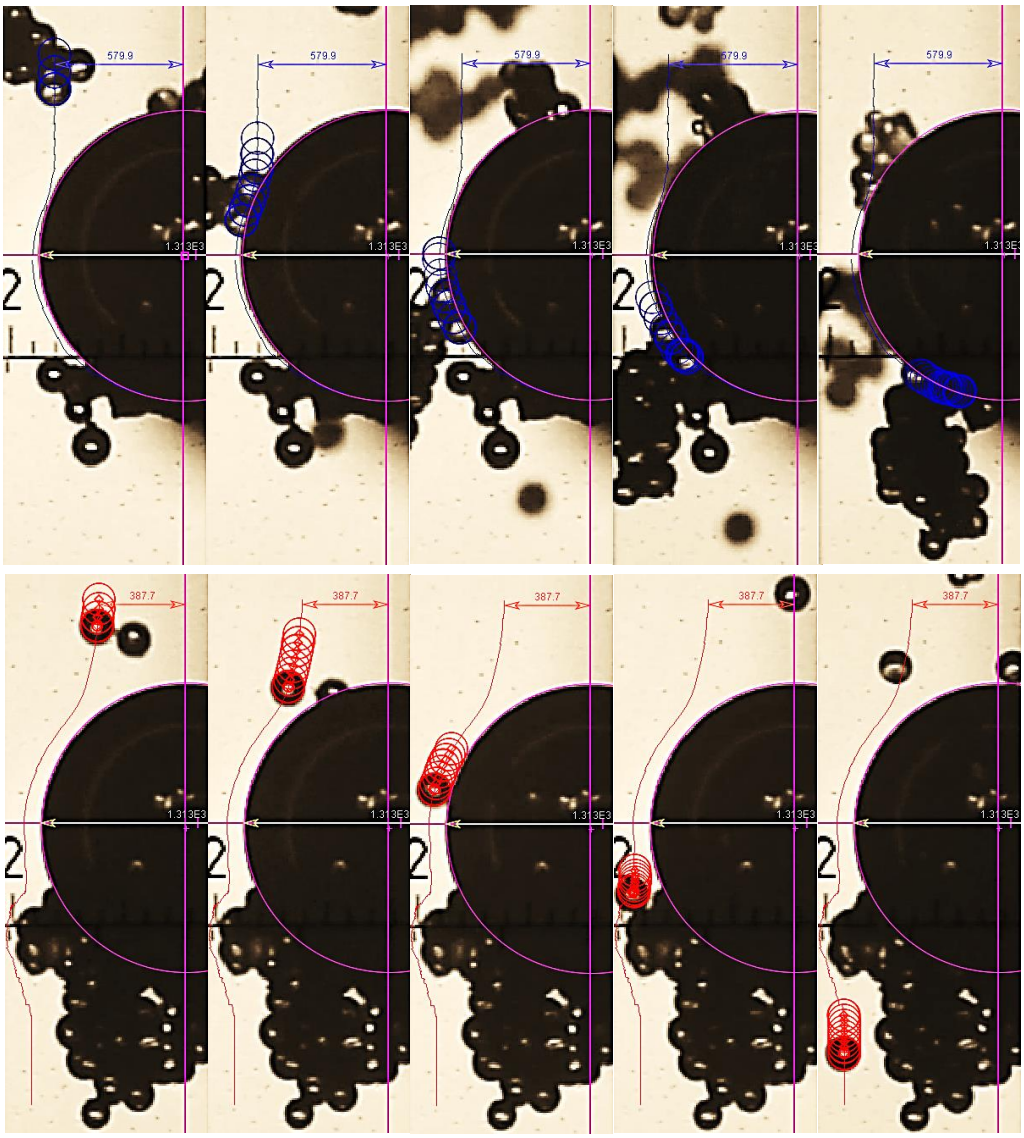

Figure 4-50. Nanobubble coated particle surface bridges particles to form aggregates, and in consequence enhances particle-bubble interaction. Hydrophobic particle aggregates have a higher attachment probability than that of a single particle.

Figure 4-51 shows the attachment of very strongly hydrophobic particles of 110° contact angle. It is noticed that the larger the collision angle (ϕ_o), the longer the travelling distance of a particle in approximately the same period of time on the bubble surface prior to the jump in action. This time is the induction time (t_i).The induction time is the time a particle takes to travel from the collision point to the water film penetration point. In the absence of nanobubbles, the average induction time of a very strongly hydrophobic particle was 48 ms, as shown in Figure 4-52.

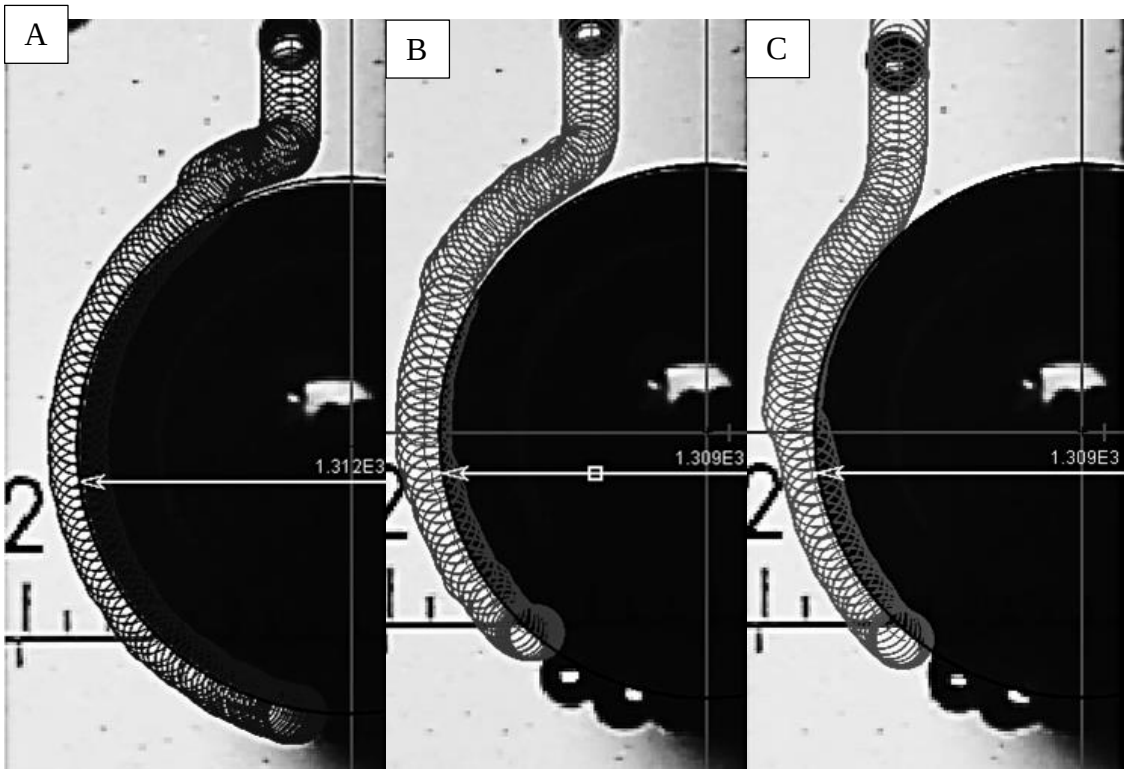

Figure 4-51. Attachment of very strongly hydrophobic particles (θ =110°) without nanobubbles to stationary air bubble in deionized water (A) 160 µm particle diameter, 1312 µm bubble diameter, 12° collision angle (B) 150 µm particle diameter, 1310 µm bubble diameter, 26° collision angle (C) 150 µm particle diameter, 1310 µm bubble diameter, 44° collision angle.

Figure 4-52 shows the polar position and radial distance vs. the time for particles of the same degree of hydrophobicity (θ =110°) with different sizes or collision angles. The slope of the polar position vs. time curve determines the angular speed. At the moment of particle collision with the bubble surface, the angular speed was at a small value. As the particle moved on the bubble surface, the speed increased and maintained a fairly constant value until the particle got attached and the angular speed became zero.

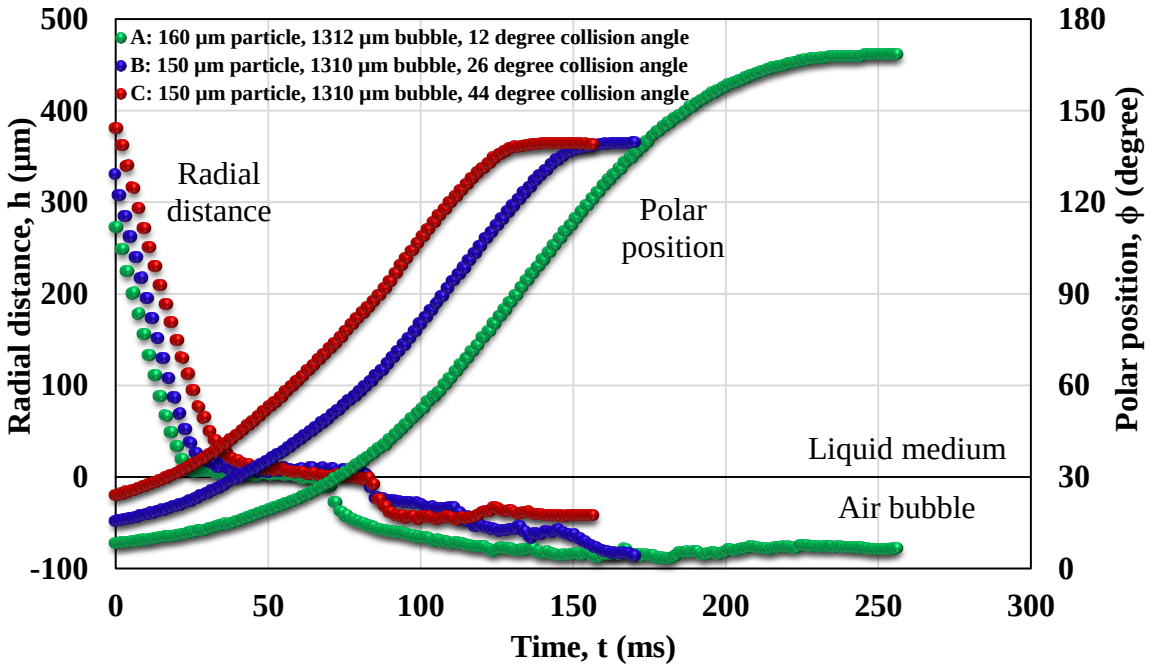

Figure 4-52. Attachment of very strongly hydrophobic particles (θ =110°) without nanobubbles to stationary air bubble in deionized water: the average induction time was about 48 ms.

The nanobubbles generated on the surface of a very strongly hydrophobic particle improved the attachment probability by reducing the induction time (t_i) by about one-half, from 48 ms to 27 ms (Figure 4-53 and Figure 4-54). The nanobubbles adsorbed on the hydrophobic particles caused a faster film rupture and particle attachment to the air bubble. Fan, Zhao and Tao (2012) found that nanobubbles increased particles hydrophobicity in terms of contact angle (θ) and it is noticed that nanobubbles

increased the particle hydrophobicity in terms of the induction time (t_i) and reduced the dosage of the collector used to increase the differential flotation rate in column flotation to one-half, as shown in Figure 4-13.

Figure 4-54 shows that particle (B) was sliding faster than particle (A) because the sliding velocity increases with increasing the collision angular (polar) position. The sliding velocity reaches its maximum value at 90^o polar position at which the largest slope of polar position vs. time curve is obtained. The average induction time for very strongly hydrophobic particle of 110^o contact angle was 27 ms, as shown in Figure 4-54.

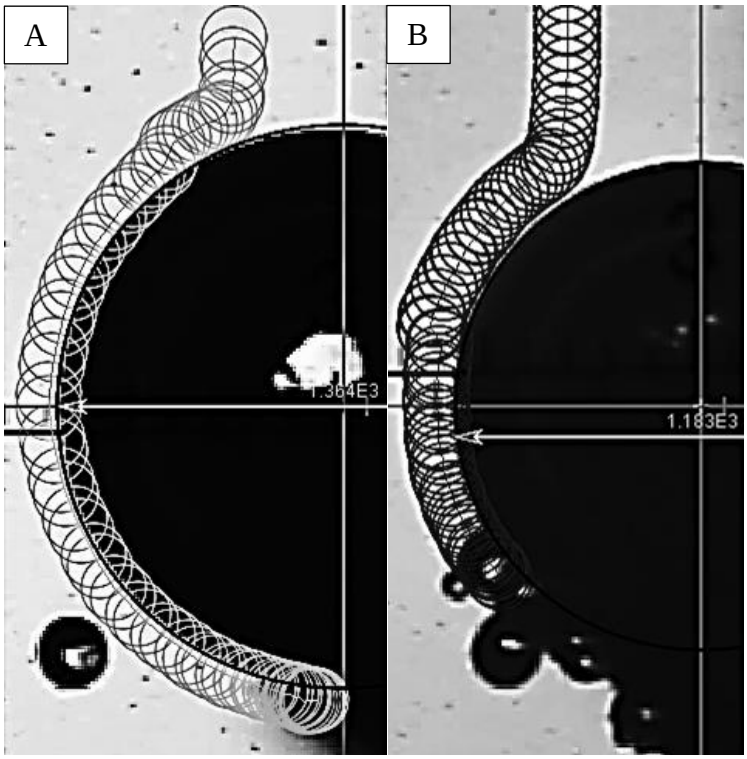

Figure 4-53. Attachment of very strongly hydrophobic particles (θ =110^o) with nanobubbles to stationary air bubble in deionized water (A) 160 µm particle diameter, 1364 µm bubble diameter, 22^o collision angle (B) 160 µm particle diameter, 1183 µm bubble diameter, 33^o collision angle.

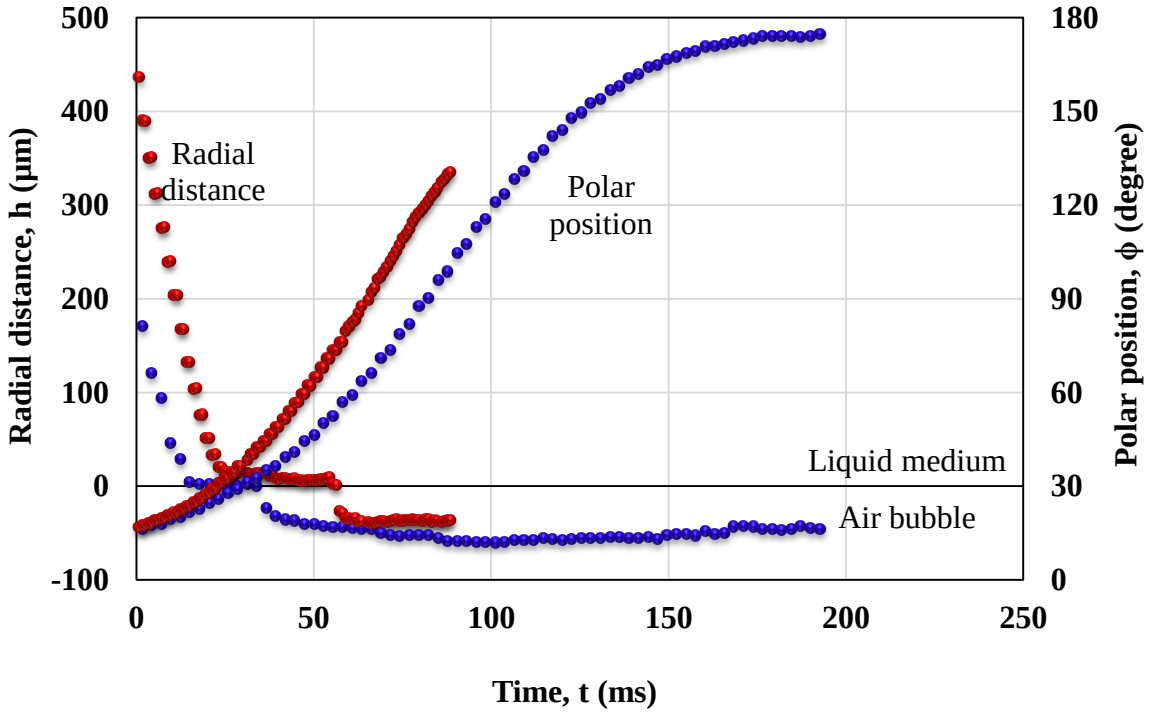

Figure 4-54. Attachment of very strongly hydrophobic particles (θ =110^{o}) with nanobubbles to stationary air bubble in deionized water: the average induction time was about 27 ms.

Reducing the particle hydrophobicity to 85^{o} contact angle increased the induction time to 52 ms in the absence of nanobubbles (Figure 4-55 and Figure 4-56). The presence of nanobubbles on the surface of these particles reduced the induction time from 52 ms to 35 ms (Figure 4-57 and Figure 4-58).

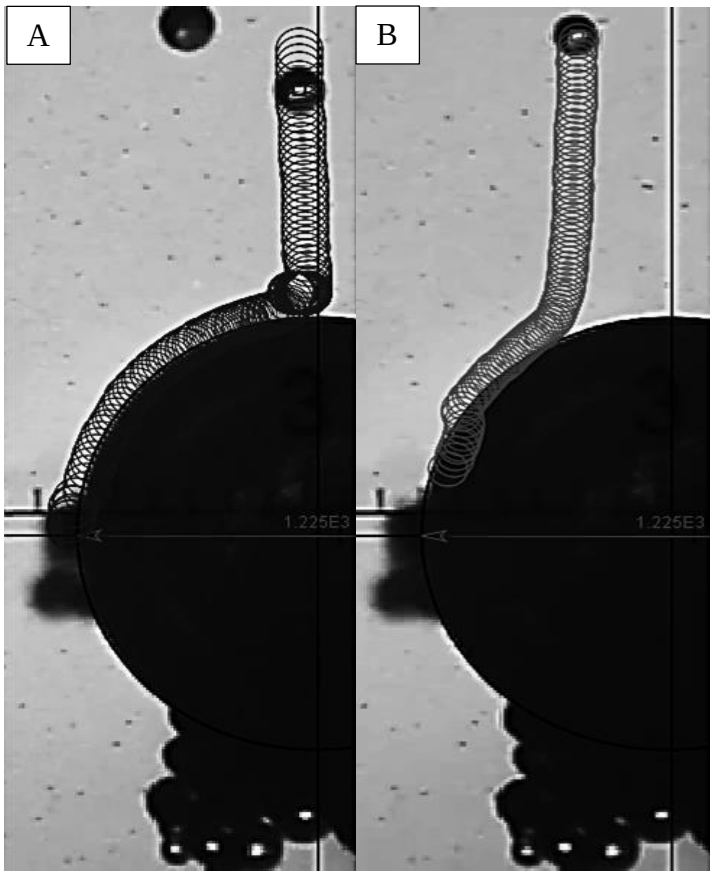

Figure 4-55. Attachment of moderately hydrophobic particles (θ =85^{o}) without nanobubbles to stationary air bubble in deionized water (A) 150 µm particle diameter, 1225 µm bubble diameter, 2^{o} collision angle (B) 125 µm particle diameter, 1225 µm bubble diameter, 9.5^{o} collision angle.

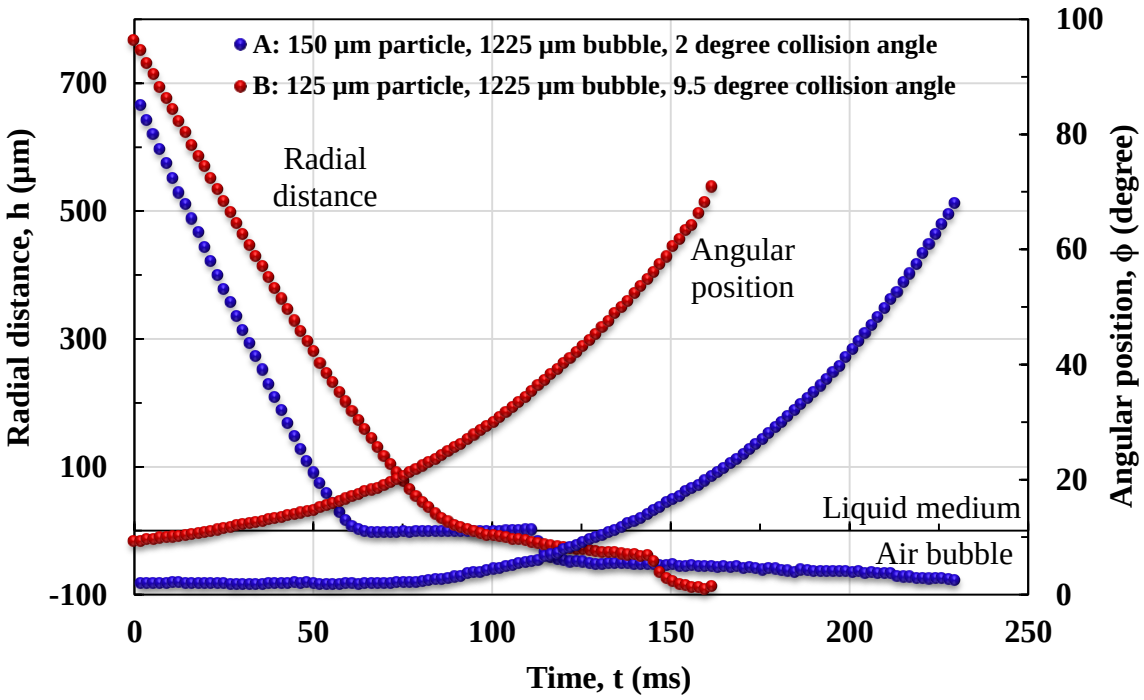

Figure 4-56. Attachment of moderately hydrophobic particles (θ =85^{o}) without nanobubbles to stationary air bubble in deionized water: the average induction time was about 52 ms.

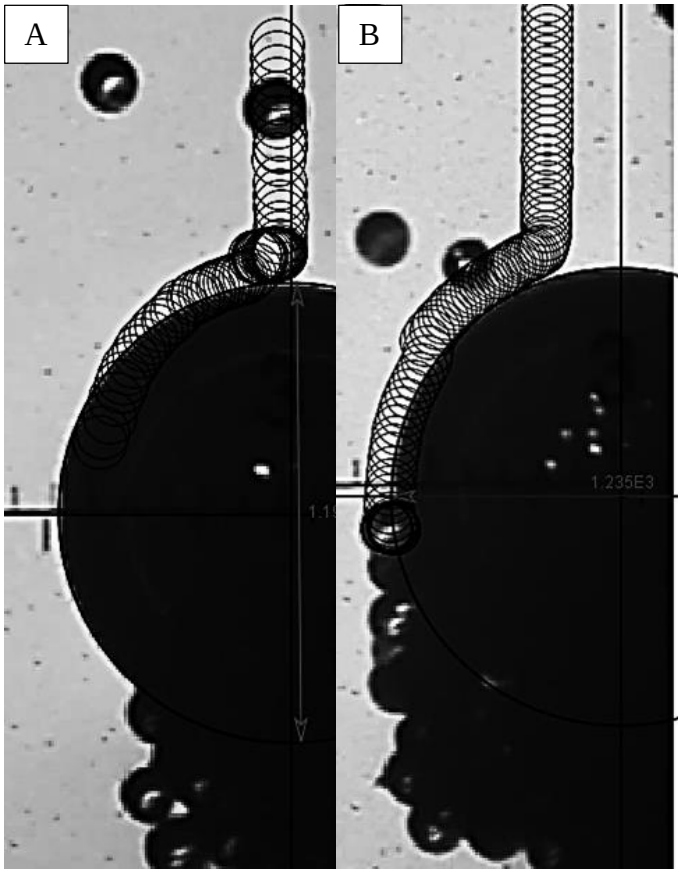

Figure 4-57. Attachment of moderately hydrophobic particles (θ =85^{o}) with nanobubbles to stationary air bubble in deionized water (A) 150 µm particle diameter, 1200 µm bubble diameter, 2^{o} collision angle (B) 150 µm particle diameter, 1240 µm bubble diameter, 9^{o} collision angle.

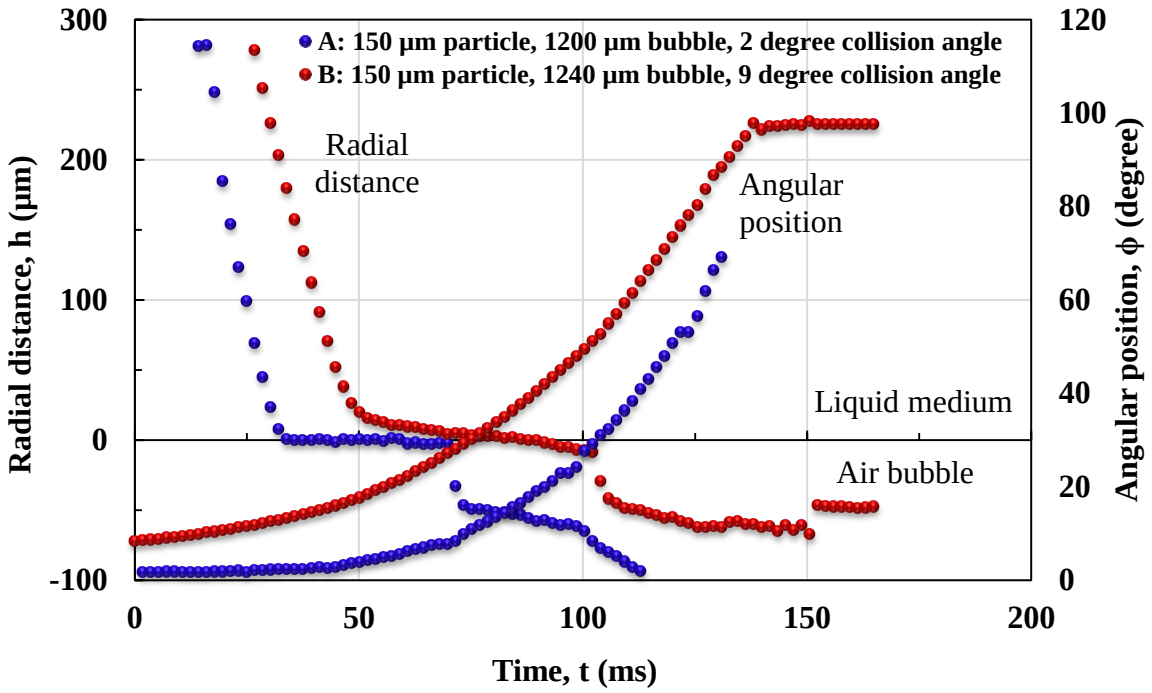

Figure 4-58. Attachment of strongly hydrophobic particles (θ =85^{o}) with nanobubbles to stationary air bubble in deionized water: the average induction time is about 35 ms.

For weakly hydrophobic particles of 50^{o} contact angle, the induction time was increased to 75 ms in the absence of nanobubbles (Figure 4-59 and Figure 4-60), while in the presence of nanobubbles the induction time was 43 ms (Figure 4-61 and Figure 4-62).

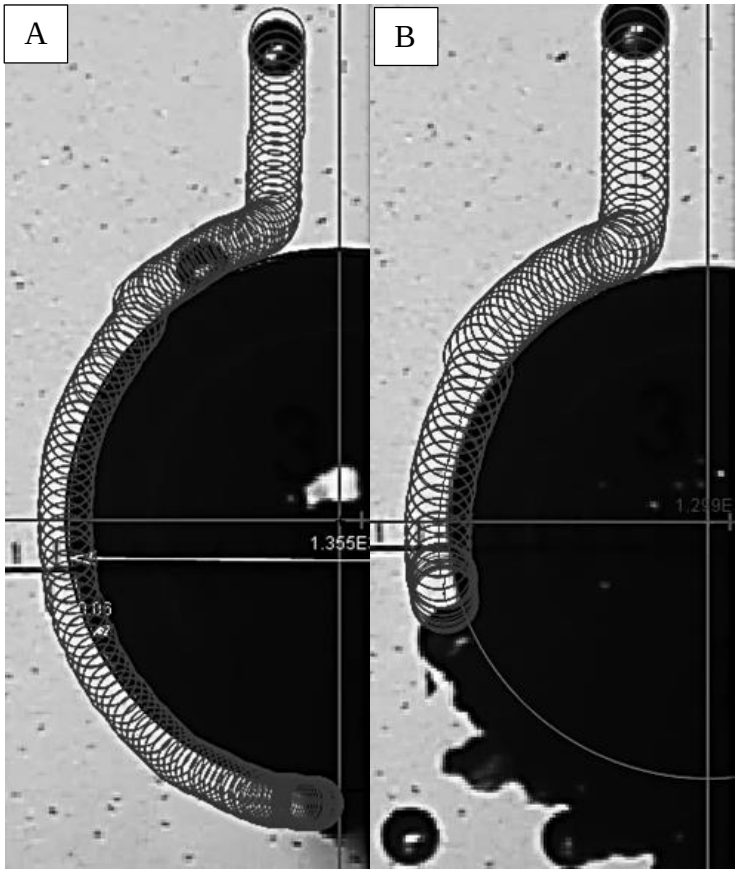

Figure 4-59. Attachment of weakly hydrophobic particles (θ =50^{o}) without nanobubbles to stationary air bubble in deionized water (A) 150 µm particle diameter, 1355 µm bubble diameter, 14^{o} collision angle (B) 150 µm particle diameter, 1300 µm bubble diameter, 17^{o} collision angle.

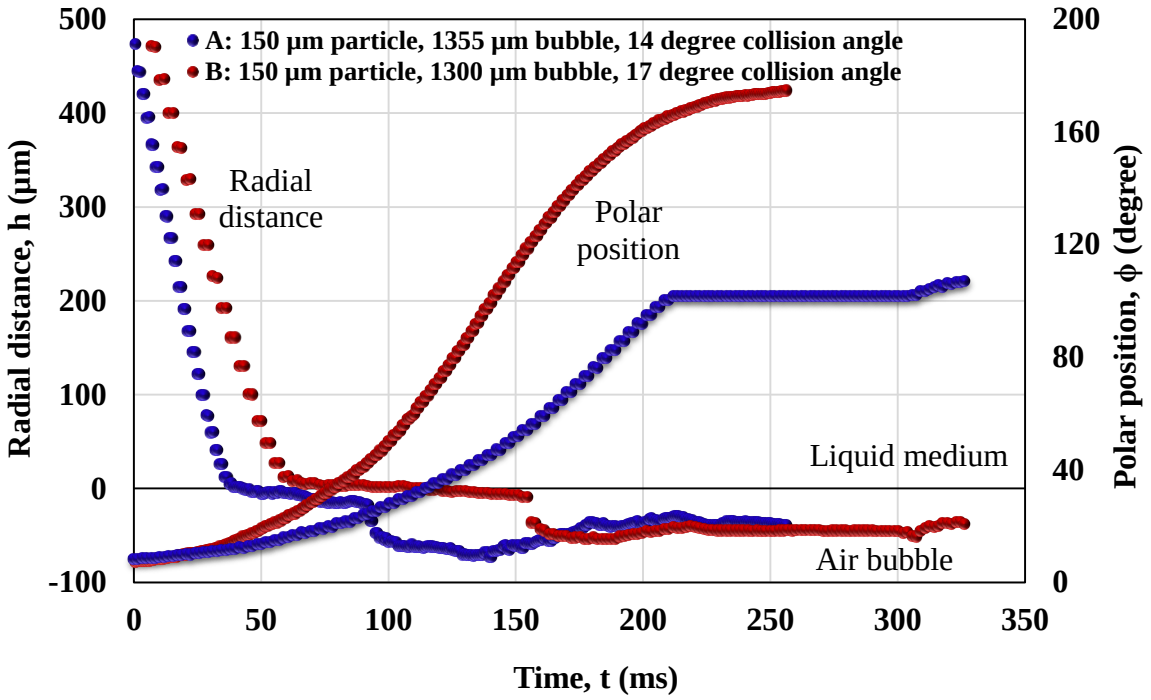

Figure 4-60. Attachment of weakly hydrophobic particles (θ =50°) without nanobubbles to stationary air bubble in deionized water: the average induction time was about 75 ms.

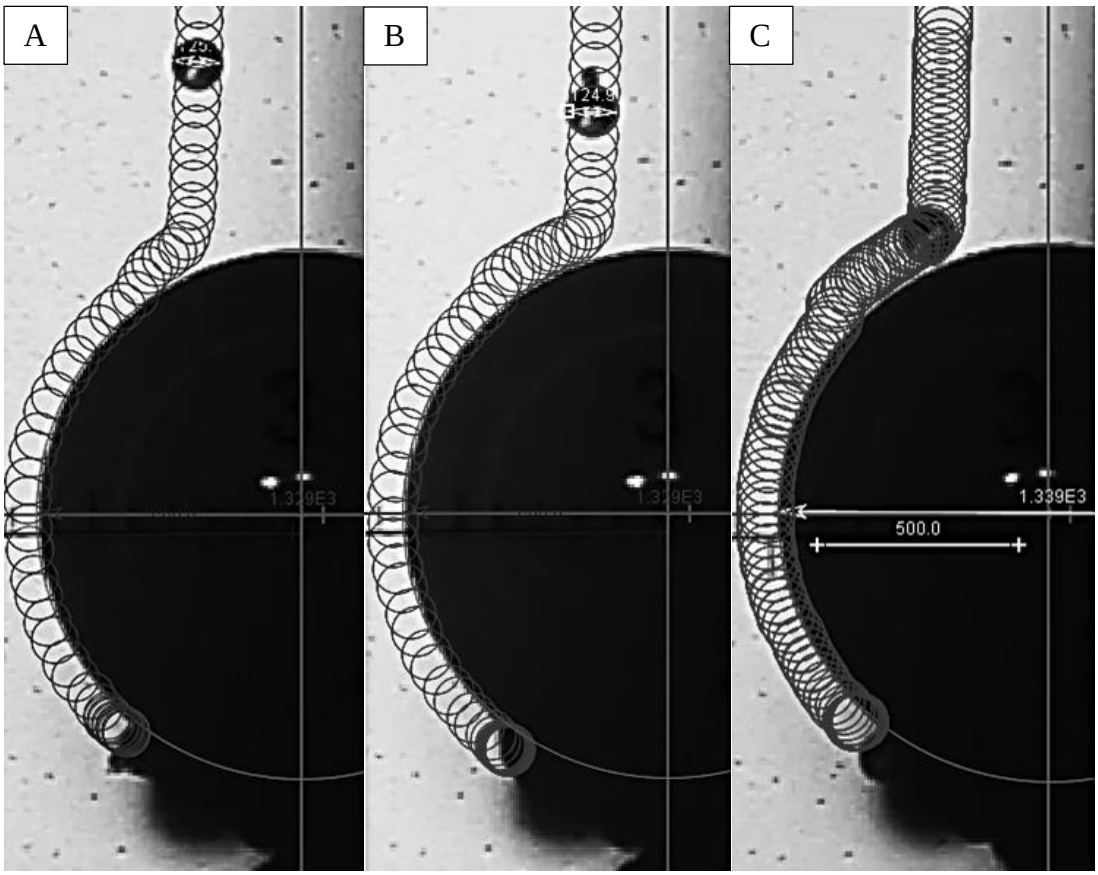

Figure 4-61. Attachment of intermediate hydrophobic particles (θ =50^{o}) with nanobubbles to stationary air bubble in deionized water (A) 125 µm particle diameter, 1330 µm bubble diameter, 22^{o} collision angle (B) 125 µm particle diameter, 1330 µm bubble diameter, 16^{o} collision angle (C) 150 µm particle diameter, 1340 µm bubble diameter, 22^{o} collision angle.

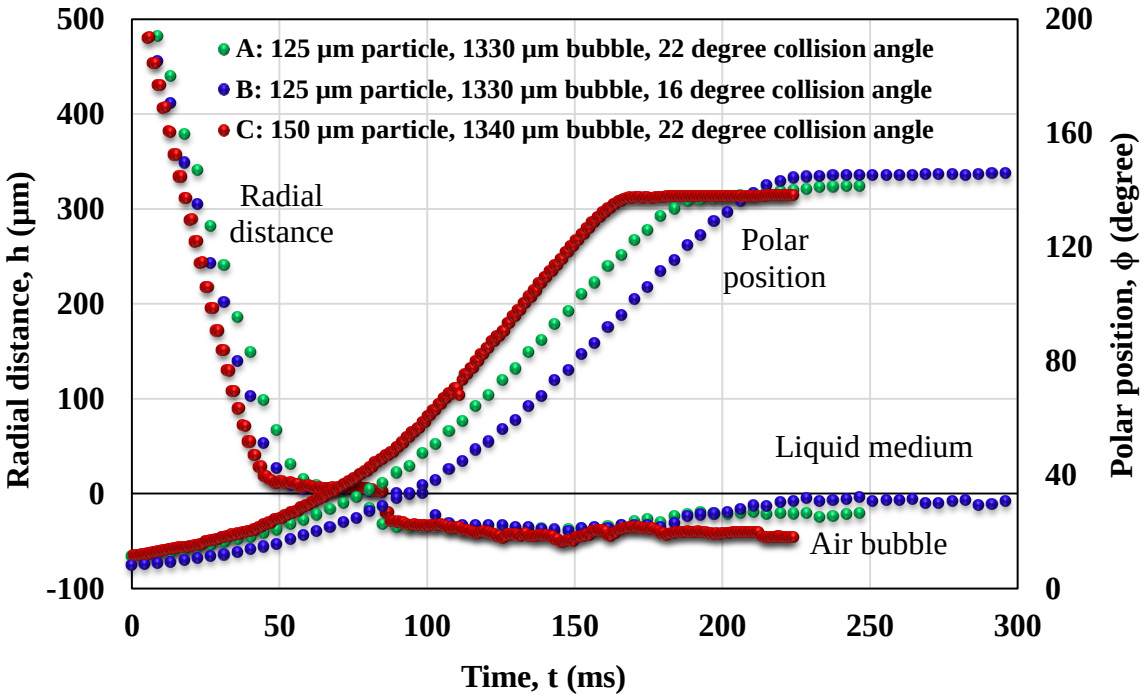

Figure 4-62. Attachment of weakly hydrophobic particles (θ =50°) with nanobubbles to stationary air bubble in deionized water: the average induction time was about 43 ms.

For very weakly hydrophobic particles approaching a bubble surface, the jump-in action was hard to be observed and the induction time could not be estimated as shown in Figure 4-63, which shows that nanobubble enhanced the attachment probability by increasing the critical attachment radius (r_{cr}) to about 250 µm (Figure 4-63A). In the absence of the nanobubbles, the critical radius was in the range 126 to 201 µm (Figure 4-63B).

The particle size is another factor significantly affecting the attachment probability. It changes the sliding time and the centrifugal force of a particle sliding on a bubble surface. Increasing the particle size increases the sliding time to a critical value after which the particle slides faster with a higher centrifugal force, and thus reduces the attachment probability. When the sliding time becomes shorter than induction time the

sliding particle will eventually detaches from bubble surface (Figure 4-64 and Figure 4-65). Figure 4-64 shows that the smaller particle (125 μm in diameter) had a higher attachment probability than a larger particle (175 μm in diameter). Figure 4-65 also shows that the larger particle had a greater angular speed on the bubble surface than that of the smaller particle.

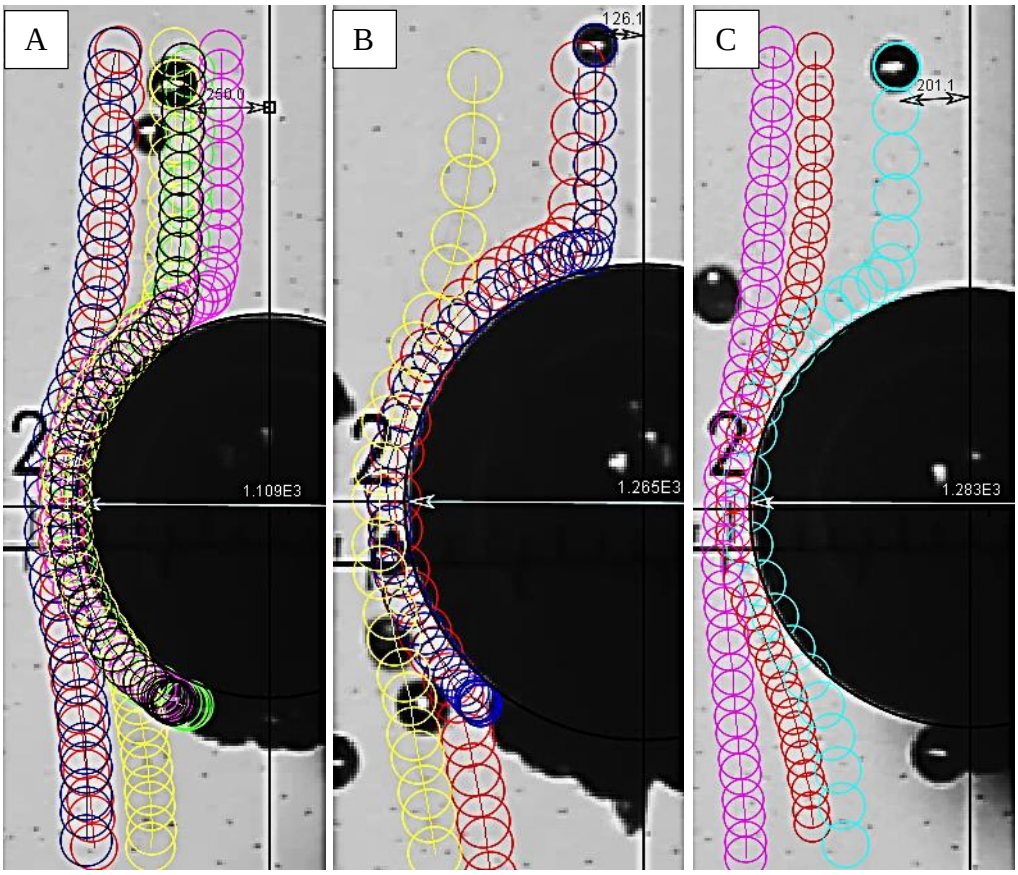

Figure 4-63. Very weakly hydrophobic particles (θ=35^{o}) approaching a stationary air bubble in deionized water (A) with nanobubbles, "larger attachment probability" (B, C) without nanobubbles.

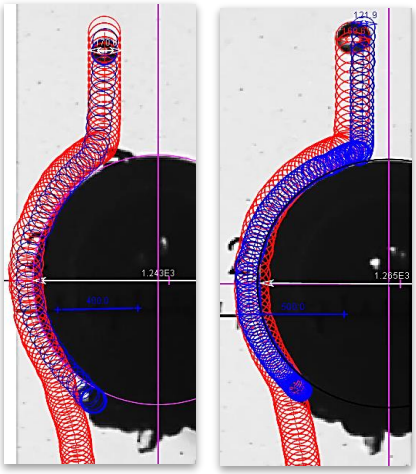

Figure 4-64. Effect of particle size (125 and 175 μm) on the attachment probability of very weakly hydrophobic particles (θ =35^{o}) without nanobubbles approaching a stationary air bubble in deionized water.

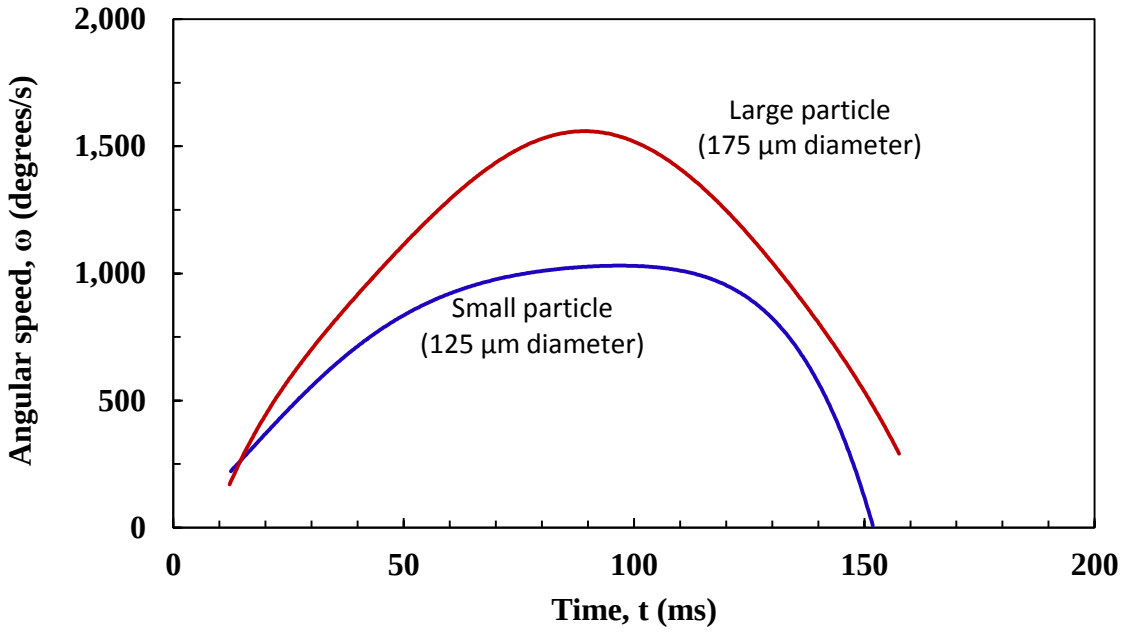

Figure 4-65. Angular speed of very weakly hydrophobic particles (θ =35^{o}) of different sizes without nanobubbles approaching a stationary air bubble in deionized water.

The forces acting on a particle approaching a bubble surface and their directions are shown in Figure 4-66. The forces can be divided into (Schimmoller, Luttrell and Yoon, 1993):

- Hydrodynamic forces: streamline force (F_s), bubble film thinning force (F_r), drag force (F_D), gravitational force (F_g) and buoyancy force (F_b)

- Surface chemistry forces: electrostatic force (F_e), dispersive force (F_d) and hydrophobic force (F_h)

The balance between the hydrodynamic and surface chemistry forces controls the trajectory of a particle around a bubble surface. Under certain conditions at which the summation of the attaching forces is larger than the summation of the detaching forces, the thin film between the particle and the bubble spontaneously ruptures. The particle position can be defined by the radial distance (h) and polar angle (ϕ) shown in Figure 4-49. The particle colloids at an initial polar position θ_o and detaches at a polar angle θ_m (Figure 4-66).

Streamline flow around a bubble surface generates a streamline force (F_s) that moves the particle around the bubble surface in two directions: radial and tangential directions. Another resistance force (F_r) is produced due to water film thinning in the radial direction only and resists the particle movement toward the bubble surface (Schimmoller, Luttrell and Yoon, 1993). The motion of the particle is influenced by other hydrodynamic forces such as the gravity (F_g), buoyancy (F_b) and drag (F_D) forces.

As the radial distance (h) between the particle and the bubble surface decreases, an electrostatic force (F_e) is created as a result of the interaction between the electrical double layers of the particle and bubble surface, which can be attractive or repulsive,

depending on the surface charges of the particle and the bubble. The fluctuating dipoles of the molecules of the particle and the air bubble in a third medium produce a dispersive force (F_d) which is a repulsive for froth flotation since the dielectric constant of water lies between that of the bubble and the particle (Schimmoller, Luttrell and Yoon, 1993). The hydrophobic force (F_h) is the most important surface force in the bubble-particle interaction (Schimmoller, Luttrell and Yoon, 1993). F_h is an attractive force for hydrophobic particles and decays exponentially with the separation distance (h) between the particle and the bubble (Schimmoller, Luttrell and Yoon, 1993). Fan, Zhao and Tao (2012) found that nanobubbles increase the particle hydrophobicity by up to 20 degrees in terms of contact angle. This should have a significant impact on the hydrophobic attraction that enhances the attachment probability as a result of reducing the induction time (t_i), which was confirmed.

Derjaguin and Dukhin (1960) divided the particle-bubble capture process into three zones: hydrodynamic interaction, diffusiophoretic and surface force zones (Figure 4-66). The hydrodynamics controls the collision process and governs the particle-bubble approach in the pulp phase of the flotation process. Diffusiophoretic zone is a zone of spontaneous motion of dispersed particles in a fluid induced by a diffusion gradient (concentration gradient) of a substrate. As the particle approaches the bubble to within the range of surface forces, the intervening liquid film between the particle and bubble surface drains, producing a critical thickness at which the film rupture takes place to establish a stable wetting perimeter (three-phase contact). If the particle does not approach the bubble surface close enough or the kinetic forces exceed the attaching forces, the particle may dislodge from the bubble surface and the detachment process can occur (Nguyen and Schulze, 2004). Once the particle attaches to the bubble surface as shown in Figure 4-67, the probability of attachment stability (the strength of the particle attachment) is determined by the balance between the attachment forces (F_{Attach}) and detachment forces (F_{Detach}) acting on the adsorbed particle with wetting perimeter of

three-phase contact angle (θ) to the bottom of the rising bubble surface in the flotation system (Heindel, 1997).

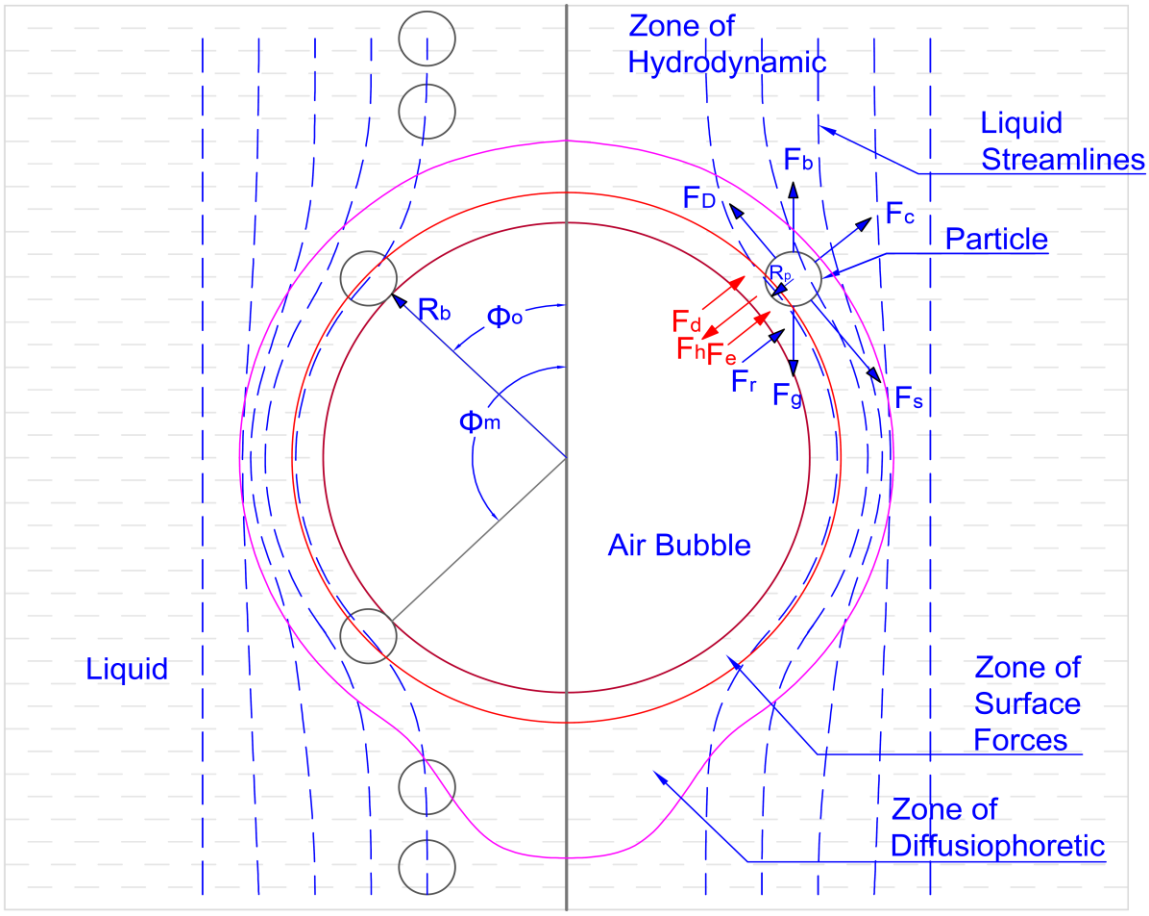

Figure 4-66. Schematic showing hydrodynamic and surface forces involved in the bubble-particle interaction (Derjaguin and Dukhin, 1960; Schimmoller, Luttrell and Yoon, 1993; Nguyen and Schulze, 2004).

The detachment forces (F_{Detach}) consist of the apparent weight of particle (F_{Wt}), the velocity dependent drag force (F_D), and the capillary pressure force on the side of the bubble due to surface tension (F_σ). F_σ is a measure of the tendency of a bubble to minimize its surface area.

$$F_{Detach} = F_{Wt} + F_D + F_\sigma \tag{13}$$

The apparent weight (F_{wt}) consists of the gravity and buoyancy forces, as shown in Equation (14)

$$F_{Wt} = \frac{4}{3}\pi R_p^3 \left(\rho_p - \rho_l\right) g \tag{14}$$

The velocity dependent drag force (F_D) is shown in Equation (15):

$$F_D = \frac{4}{3}\pi R_p^3 \rho_p \frac{1.9\varepsilon^{\frac{2}{3}}}{\left(R_b + R_p\right)^{\frac{1}{3}}} \tag{15}$$

where ε is the turbulent energy density and it has a constant value between 10^{-3} and 10^{-1} kW/kg (Schulze, 1984)

The capillary pressure force on the side of the bubble due to surface tension (F_σ) is given by Equation (16):

$$F_\sigma = \pi R_p^2 \left(\frac{2\sigma}{R_b} - 2R_b \rho_l g \right) \sin^2 \omega \tag{16}$$

The attachment forces (F_{Attach}) include the hydrostatic pressure force (F_H) of the liquid column (H) on the area enclosed by the three-phase contact and the capillary force acting on the three-phase contact line (F_{Ca}).

$$F_{Attach} = F_H + F_{Ca} \tag{17}$$

$$F_{Ca} = -2\pi R_p \sigma \sin\omega \sin\left(\omega + \theta\right) \tag{18}$$

The two capillary forces can be maximized by setting (Schulze, 1989):

$$\omega = \pi - \frac{\theta}{2} \tag{19}$$

Equations (17) and (18) become

$$F_{\sigma} = \pi R_p^2 \left(\frac{2\sigma}{R_b} - 2R_b \rho_l g \right) \sin^2 \left(\pi - \frac{\theta}{2} \right) \tag{20}$$

$$F_{Ca} = -2\pi R_p \sigma \sin\left(\pi - \frac{\theta}{2} \right) \sin\left(\pi + \frac{\theta}{2} \right) \tag{21}$$

where σ is the interfacial surface tension between the liquid and the gas, ρ_p and ρ_l are the particle and liquid densities, respectively, g is the acceleration of gravity, R_b and R_p are the radii of the bubble and the particle, respectively, ω is the angle shown in Figure 4-67 and θ is three-phase contact angle.

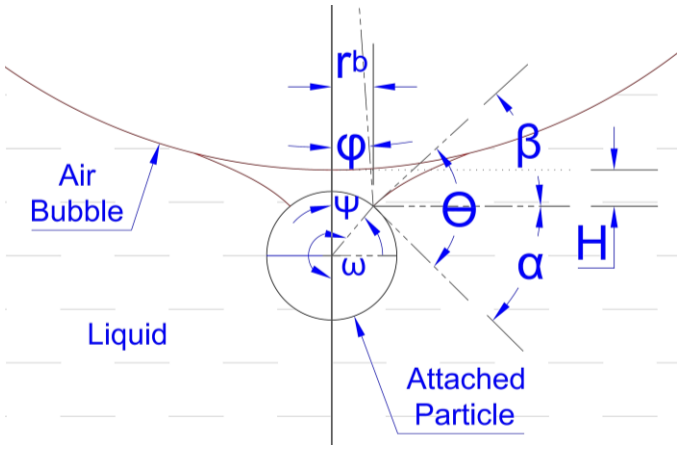

Figure 4-67. Illustration of a particle attached to a regular flotation bubble.

The overall attachment and detachment forces are given in Equations (23) and (24), respectively.

$$F_{Attach} = 6\,\sigma \sin\left(\pi - \frac{\theta}{2} \right) \sin\left(\pi + \frac{\theta}{2} \right) \tag{23}$$

$$F_{Detach} = 4R_p^2\left[\Delta\rho_p g + \frac{1.9\rho_p \varepsilon^{2/3}}{\left(R_p + R_b\right)^{1/3}}\right] + 3R_p\left[\frac{2\sigma}{R_b} - 2R_b\rho_l g\right]\sin^2\left(\pi - \theta/2\right) \quad (24)$$

Plate (1993) and Schulze (1989) show that the probability of attachment stability can be given by Equation (25):

$$P_{Stability} = 1 - \exp\left(1 - \frac{F_{Attach}}{F_{Detach}}\right) \quad (25)$$

4.5.2. Flotation Froth Stability

Froth stability has a significant impact on the froth flotation process. When the froth is not stable, the bubbles rupture before they report to the concentrate launder and the hydrophobic particles drop-back down the pulp zone. On contrast, a froth that is too stable will also carry entrained gangue to the concentrate. Thus, the degree of froth stability strongly affects the process efficiency and selectivity.

Coalescence of two bubbles in water is thermodynamically favorable to form a larger, single bubble. For example, shaking a container of water creates bubbles that collapse within few seconds, if the water was pure. The force generated by Laplace pressure drains the water between the approaching bubbles, which is sufficient to deform the bubbles surfaces as illustrated in Figure 4-68 and in sequence the thin draining film joining the two bubbles ruptures (Pashley and Karaman, 2005). The pressure difference given by Laplace equation: $\nabla P = 2\gamma/R$ across a flat interface A-B is zero, while there is a pressure difference where the interface is curved at A-C. Thus, the drainage of the liquid from the laminar part of the thin film (B) is governed by the pressure of the liquid in this region compared with that of the liquid in the Plateau borders (C) or in the bulk liquid. The film may either thin continuously and eventually rupture, or attain an equilibrium thickness depending on the balance of the forces which favor film thinning such as van der Waals attractive forces and a capillary pressure and the forces which resist film thinning similar to overlapping of similar charged electric double layers

(Shaw, 1992). The thinning of the interbubble layer of liquid takes place at first by drainage under gravitational forces and is then followed by movement of the liquid within the lamella by capillary pressure (Sagert and Quinn, 1978).

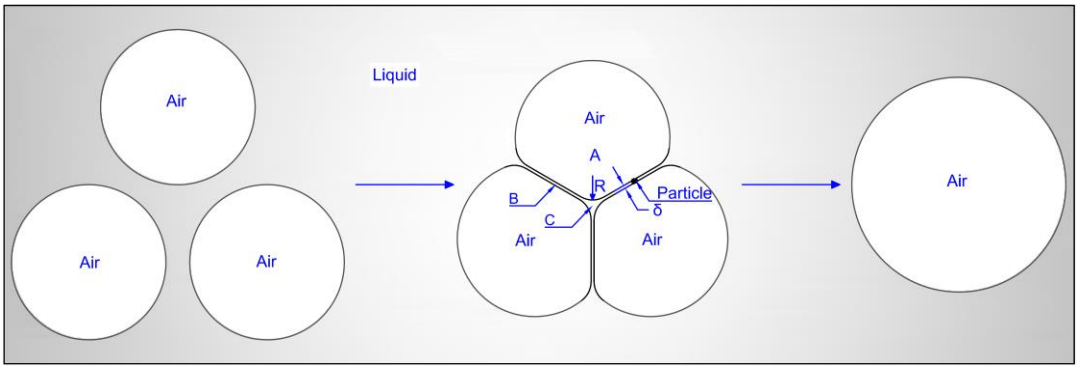

Figure 4-68. Deformation of approaching bubbles, rupturing of thin film and collapsing of bubbles in water (Dippenaar, 1982; Pashley and Karaman, 2005).

Any random disturbance caused by nanobubbles, surfactants, solid particles, etc., within the film may significantly affect the equilibrium film thickness and subsequently the froth stability. For example, lowering interfacial tension by adsorption of surfactant (frother) at air-water interface facilitates the stability of a large interfacial area. The persistence of the froth is also directly linked to the fraction of bubble surface covered by particles (Gaudin, 1957). The existence of particles is necessary to achieve a stable froth and small bubbles are less likely to coalesce, especially when loaded with particles (Szatkowski and Freyberger, 1985).

Variation in bubble size distribution and Sauter-mean bubble diameter was evaluated and the results are plotted as a function of column height in froth zone for glass spheres of various degree of hydrophobicity in the presence and absence of nanobubbles. Five degrees of hydrophobicity were investigated, i.e. very strong, strong, moderate, weak and very weak hydrophobicity, corresponding to a contact angle of 110^{o}, 85^{o}, 70^{o}, 50^{o}, 20^{o}, respectively. The study was focused on investigating the effect of nanobubbles in the presence of particles of different hydrophobicity on froth stability.

The very strongly hydrophobic particles with a contact angle of 110^{o} agglomerate and destabilize the froth zone. The agglomerated particles plug the column and then settle down to the pulp zone without reporting to the concentrate stream due to the high effective weight of the agglomerated particles, as shown in Figure 4-69. Lovell (1976) found that fine hydrophobic particles destabilize the froth, especially at low concentrations, but coarse hydrophobic particles can stabilize the froth. Hemmings (1981) reported that the solids concentration has a positive effect on the froth stability. Dippenaar (1982) found that spherical hydrophobic particles with a contact angle greater than 90^{o} or irregular particles with a lower contact angle destabilize the froth as a result of thinning of the inter-bubble liquid bridged by the particles, as shown in Figure 4-68. For a certain particle size there is an optimum degree of hydrophobicity that maximizes the froth stability.

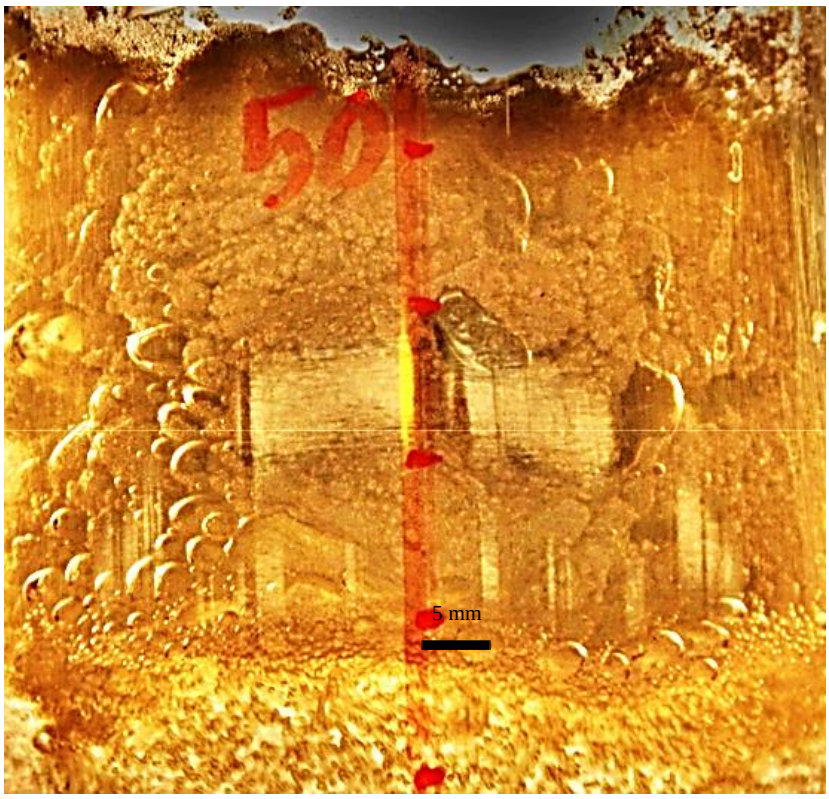

Figure 4-69. Very strongly hydrophobic particles agglomerate and destabilize the froth zone in a column flotation.

In contrast, the very weakly hydrophobic particles with a contact angle less than 20^{o} may have minimal impacts on the froth stability. It was noticed that the very weakly hydrophobic particles detach from the bubble surface before reporting to the froth zone or just settle down to the reject stream. Ata, Ahmed and Jameson (2003) found that hydrophilic or very weakly hydrophobic particles have a stabilizing effect on the froth by increasing the effective viscosity or by mechanical blockage of particles held on the surfaces of the bubbles when the film thickness between the bubbles becomes close to the size of the particles.

The existences of hydrophobic particles and/or relatively small bubbles coated with hydrophobic particles generate a stable froth, as shown in Figure 4-71. Figure 4-71 shows that the bubble coated with particles is very stable and it has a significantly smaller size than the bubbles that are not coated with particles. The particles in the laminar zone of the thin film also help prevent bubble coalescence by maintaining a thicker film.

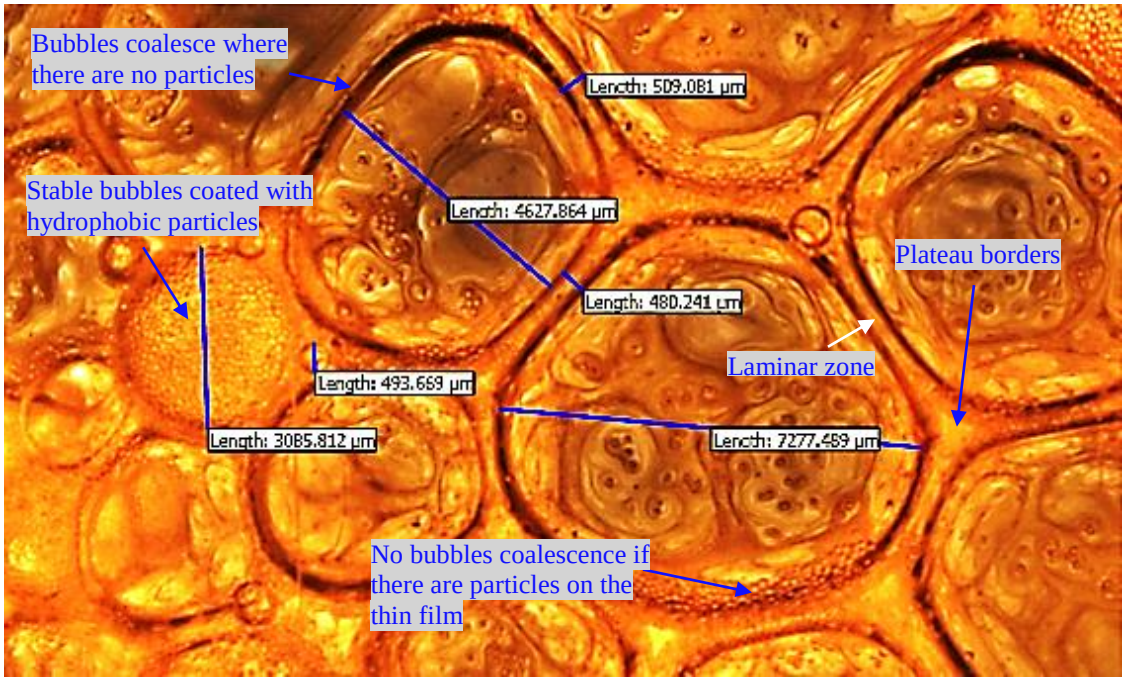

Figure 4-70. Solid particles and smaller bubbles coated with particles stabilize froth zone in column flotation.

It is noticed that the number of particles in the froth zone decreases with increasing the froth height as a result of particles drop-back as shown in Figure 4-71. Thus, the froth zone is less stable starting from a certain distance from the froth-pulp interface as shown in Figure 4-72(A-B). This phenomenon was identified by Moys (1978) who found that the detachment starts to occur above a particular distance from the froth-pulp interface. Figure 4-76, Figure 4-77 and Figure 4-78 show that the froth instability starts to take place at 50 mm above the interface as confirmed. In addition, Lynch et al. (1974) observed significant changes in the solids concentration along the froth height and found that when bubbles coalesce, the particles on their surface return to the lower part of the froth zone or to the pulp zone. Figure 4-72 (A-B) shows that the coalescence rate was significantly higher in the absence of the nanobubbles.

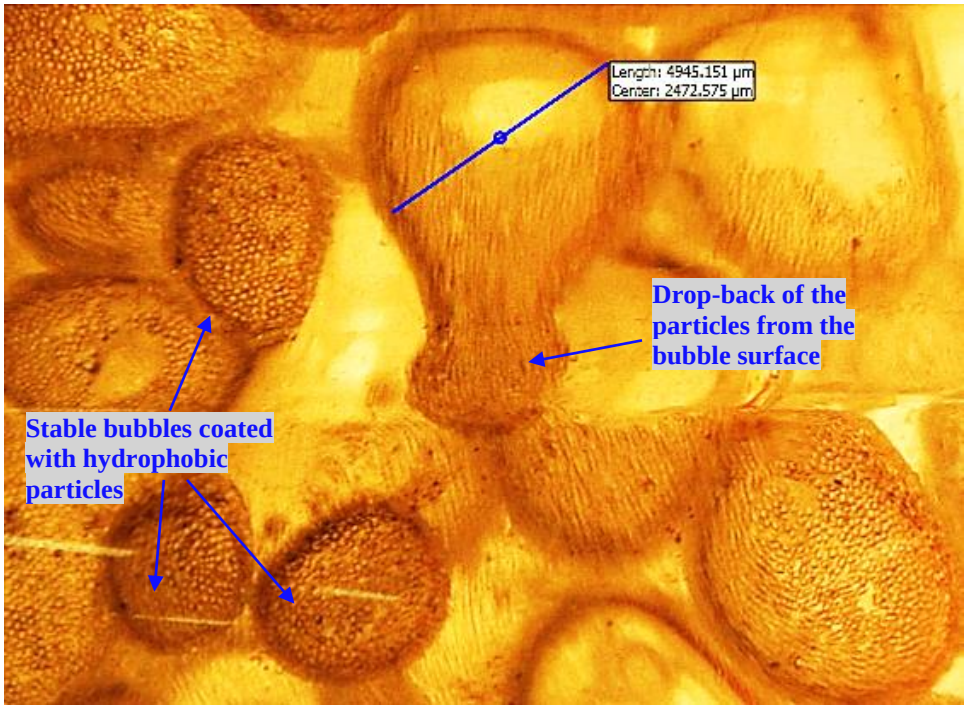

Figure 4-71. Drop-back of hydrophobic particles from bubble surface at the top of froth zone in column flotation.

Comparisons between bubble size distributions in the presence and absence of nanobubbles at six levels of froth height for other three samples: weakly, moderately, and

strongly hydrophobic particles are shown in Figure 4-73, Figure 4-74 and Figure 4-75, respectively. The bubble size distribution at the pulp-froth interface was very narrow and the bubble size distribution became wider with increasing froth height as a result of coalescence of bubbles.

Figure 4-76, Figure 4-77 and Figure 4-78 show the Sauter-mean bubble size at various heights from the interface. The Sauter-mean bubble size was estimated at least 5 times, and the standard deviation is less than 0.6%. The bubble size distribution and the Sauter-mean bubble size at froth heights 50 mm to 150 mm from the interface are closer to each other than the distribution below or above this range. The slight increase in bubble coalescence at a height above 150 mm is a result of wash water addition to the top froth zone, which is known as the washing zone.

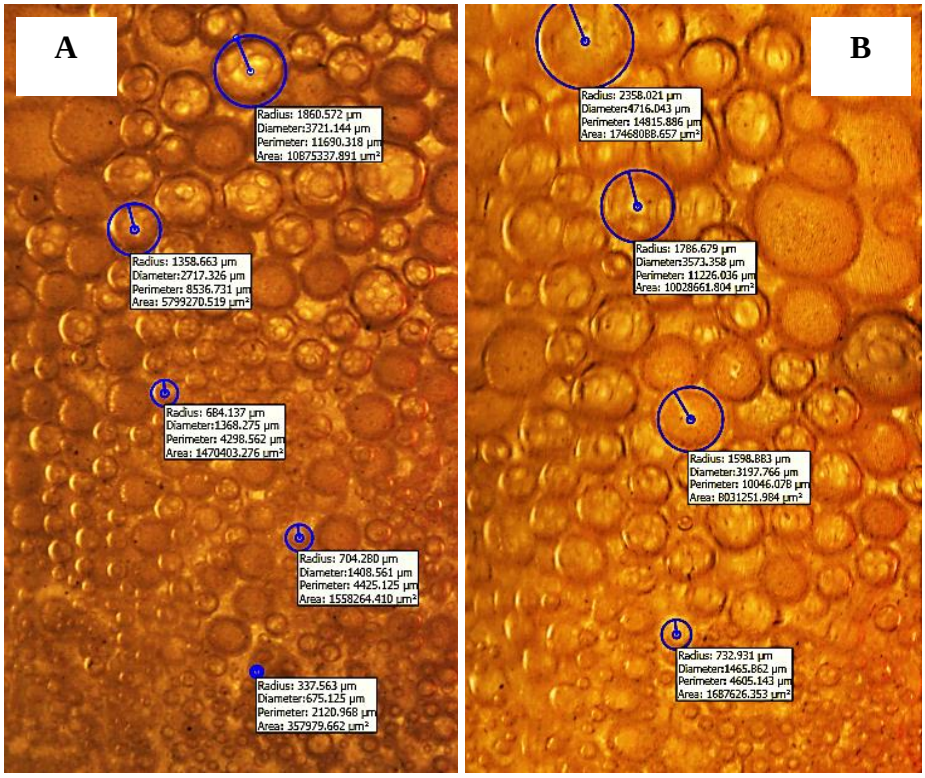

Figure 4-72. Froth zone is less stable starting from a certain distance from the froth-pulp interface in column flotation: (A) with nanobubbles (B) without nanobubbles.

Nanobubbles significantly influence the bubble diameter and froth stability as a result of increasing particle hydrophobicity, as shown in Figure 4-73 to Figure 4-78. It is clear from these figures that nanobubbles have a stronger impact on reducing bubble size distribution and Sauter-mean bubble diameter for strongly hydrophobic particles than for moderately or weakly hydrophobic particles. The maximum froth stability was accomplished when froth contains particles with moderately hydrophobic particles with a contact angle of about 70^{o}, which are capable of forming stable bridges across the liquid film between the bubbles in the froth. For example at 100 mm above the interface, the Sauter-mean bubble diameter was 5 mm, 3.5 mm and 4.75 mm in the absence of nanobubbles and 4 mm, 2.75 mm and 3.25 mm in the presence of nanobubbles for weakly, moderately, and strongly hydrophobic particle as shown in Figure 4-76, Figure 4-77 and Figure 4-78, respectively.

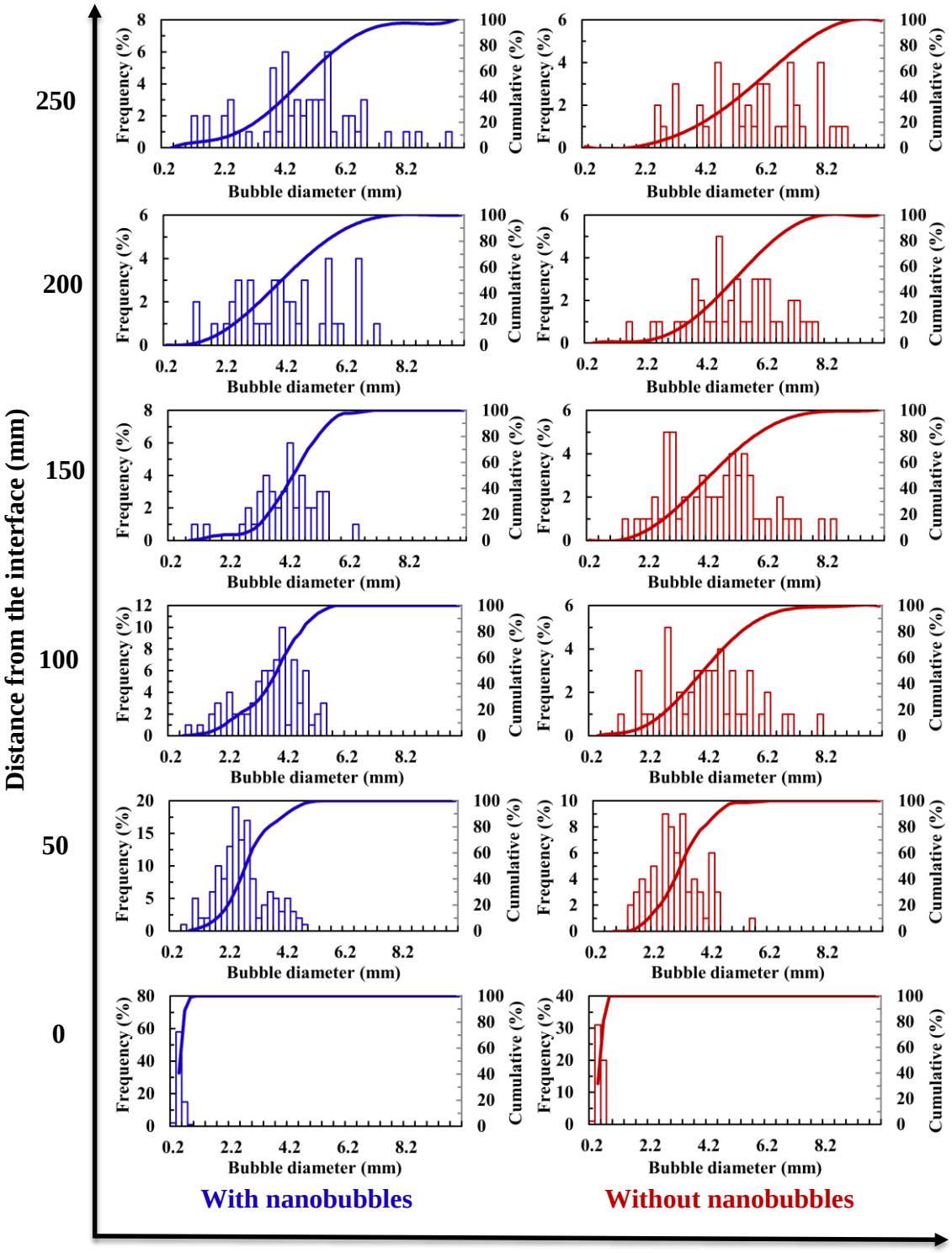

Figure 4-73. Bubble size distribution in the froth zone with and without nanobubbles as a function of froth height for weakly hydrophobic glass particle ($\theta = 50^{o}$).

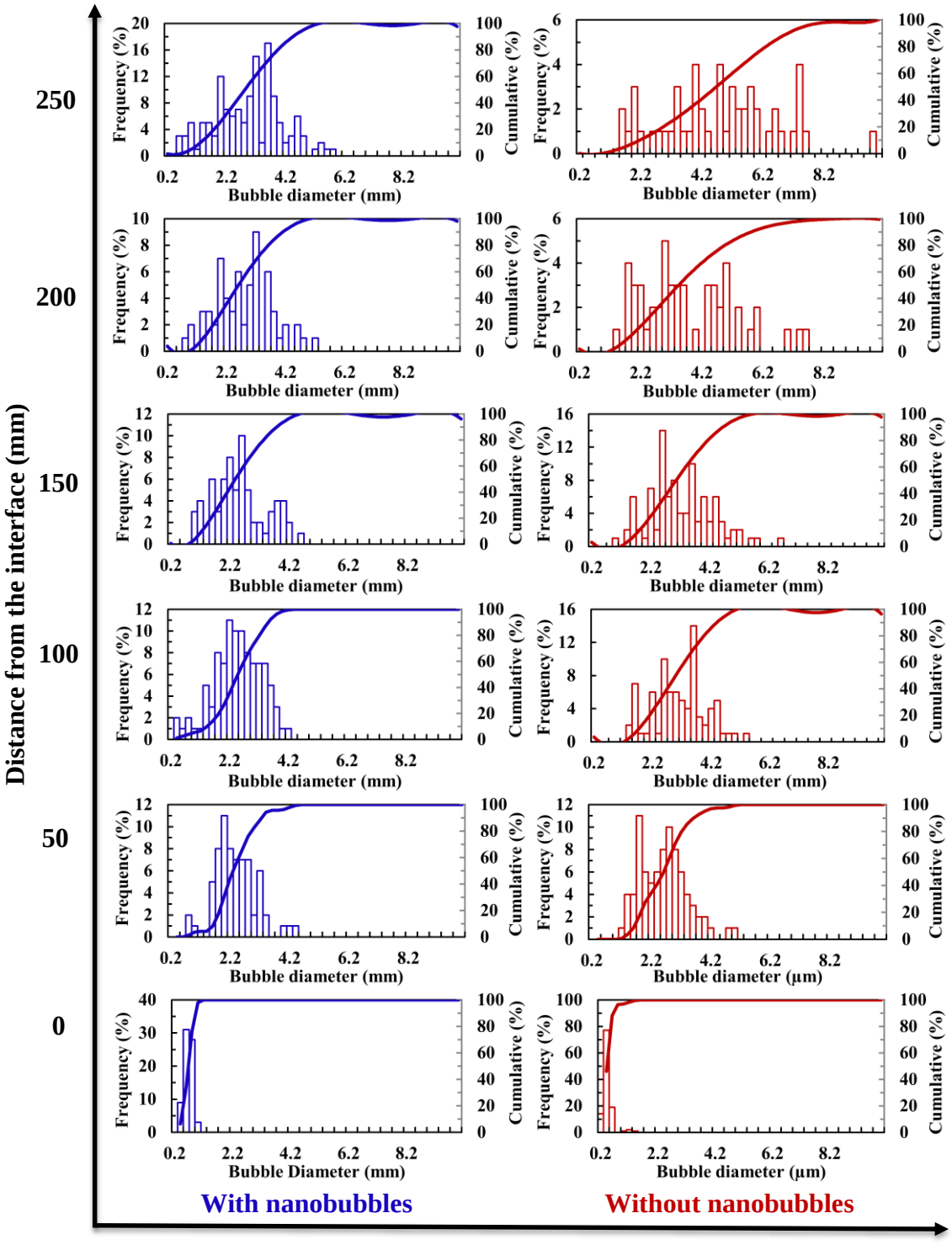

Figure 4-74. Bubble size distribution in the froth zone with and without nanobubbles as a function of froth height for moderately hydrophobic glass particle ($\theta = 70^{o}$).

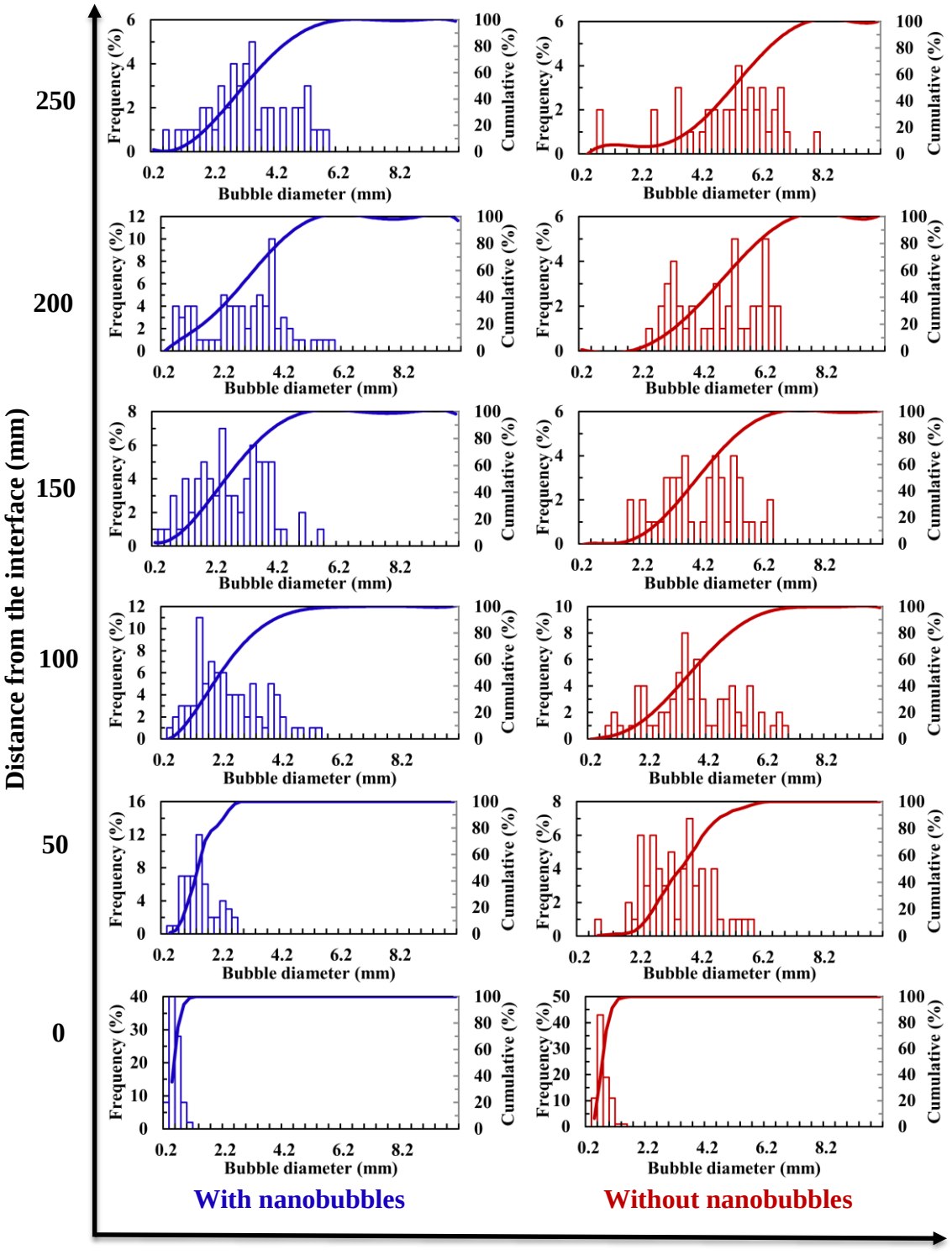

Figure 4-75. Bubble size distribution in the froth zone with and without nanobubbles as a function of froth height for strongly hydrophobic glass particle ($\theta = 85^{o}$).

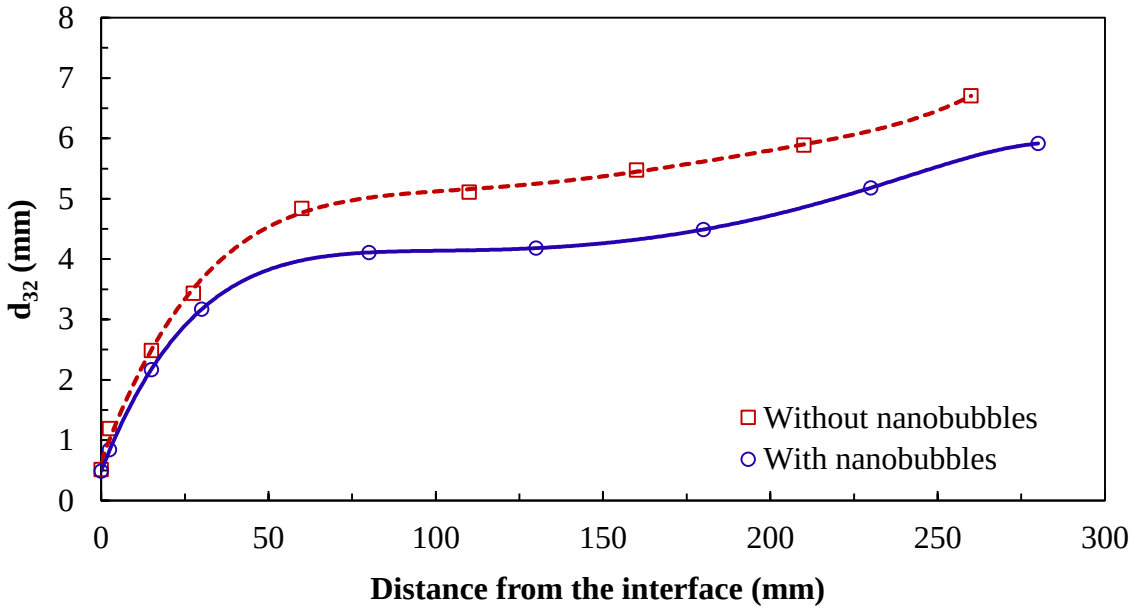

Figure 4-76. Variation of Sauter-mean bubble diameter as a function of froth height for weakly hydrophobic glass ($\theta = 50^o$) with and without nanobubbles in column flotation.

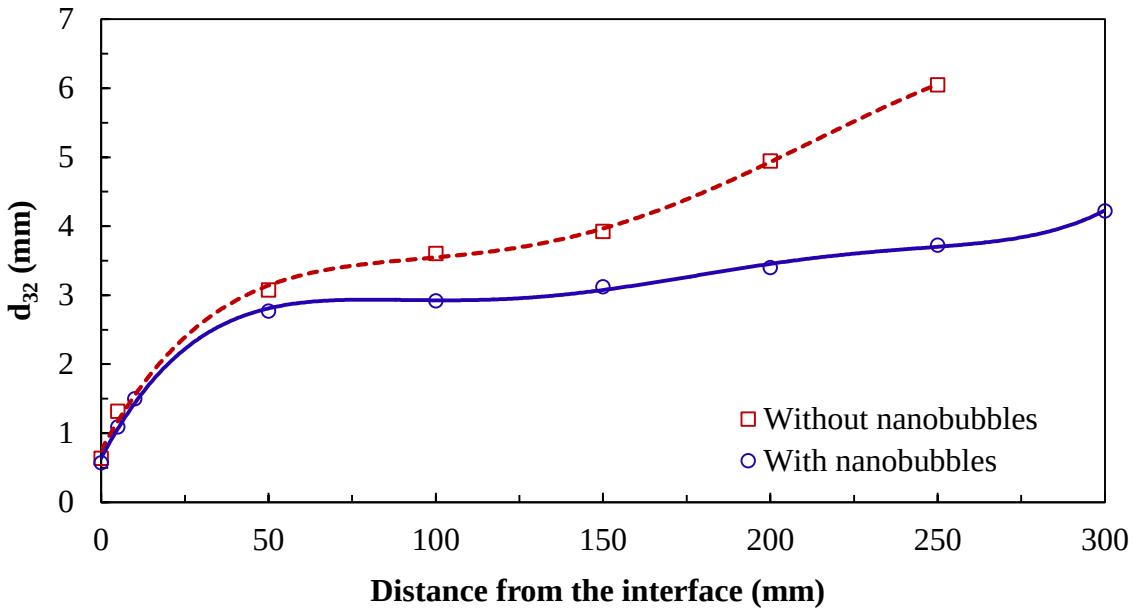

Figure 4-77. Variation of Sauter-mean bubble diameter as a function of froth height for moderately hydrophobic glass ($\theta = 70^o$) with and without nanobubbles in column flotation.

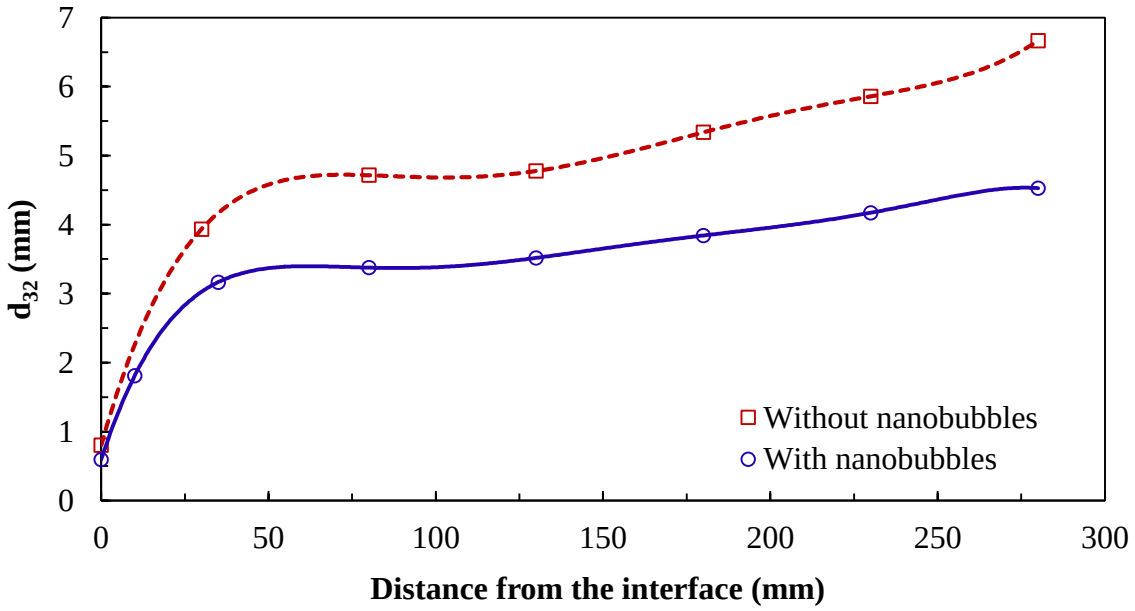

Figure 4-78. Variation of Sauter-mean bubble diameter as a function of froth height for strongly hydrophobic glass (θ = 85º) with and without nanobubbles in column flotation.

4.5.3. Surface Area Flux

Bubble surface area flux (S_b) is the total surface area of bubbles that ascend a flotation cell through a cross sectional area per unit time. It is determined using the superficial gas velocity (V_g) and Sauter-mean bubble diameter (d_{32}),

$$S_b = \frac{6V_g}{d_{32}}$$

The impact of nanobubbles on the total bubble area flux (S_b) is shown in Figure 4-79, Figure 4-80 and Figure 4-81 for weakly, moderately, and strongly hydrophobic glass spheres, respectively.

Higher S_b is associated with increased flotation rate. The S_b can reach up to 70 s^{-1} but most of the flotation processes are in the range between 15 and 30 s^{-1} where the superficial gas velocity is about 1 cm/s (Nesset et al., 2005). Increasing the gas flow rate results in increasing the mean bubble diameter and the S_b may approach a maximum value which is worth considering as the target operating point. The superficial gas velocity was kept at 0.73 cm/s, which created a relatively small bubble surface area flux in the froth zone. Higher gas flow rate may not be the most favorable for the recovery of the valuable minerals. Figure 4-79, Figure 4-80 and Figure 4-81 show that the existence of nanobubbles on the hydrophobic particles and in the slurry increased the bubble surface area flux by about 2, 3 and 4 units, respectively with increasing particle hydrophobicity. It is also clear that the highest S_b was accomplished by using moderately hydrophobic particles in the presence of the nanobubbles as shown in Figure 4-80.

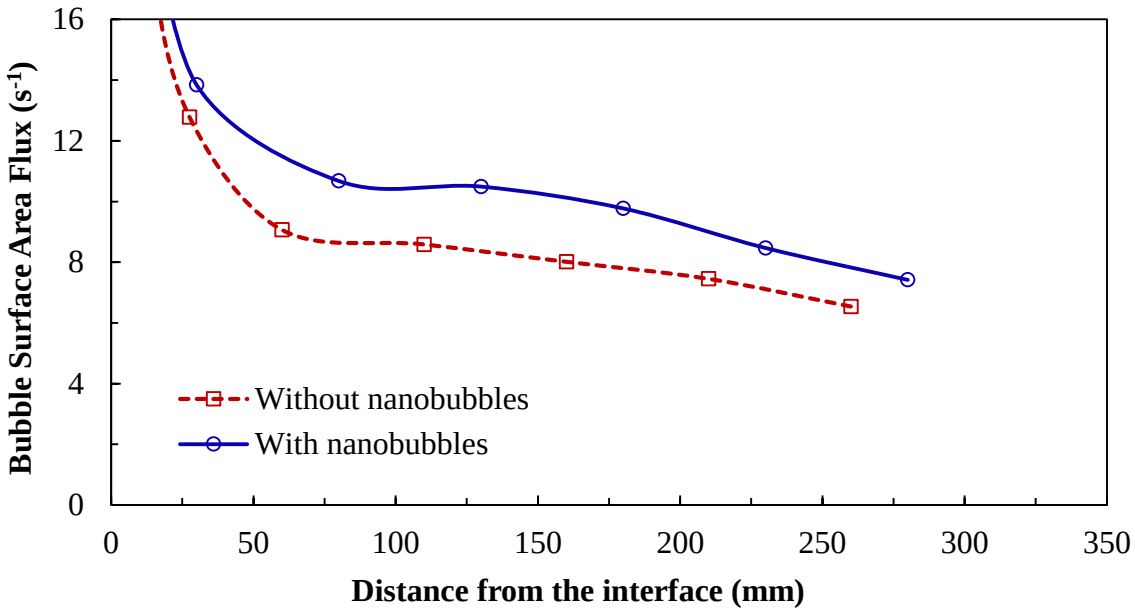

Figure 4-79. Variation of bubble surface area flux as a function of froth height for weakly hydrophobic glass (θ = 50º) with and without nanobubbles in column flotation.

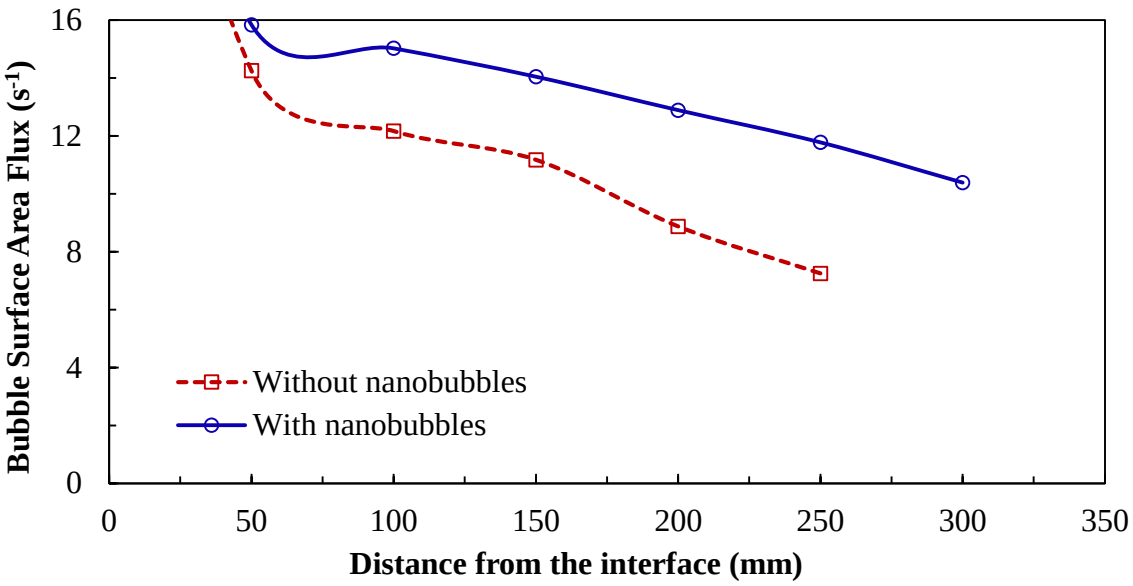

Figure 4-80. Variation of bubble surface area flux as a function of froth height for moderately hydrophobic glass ($\theta = 70^{o}$) with and without nanobubbles in column flotation.

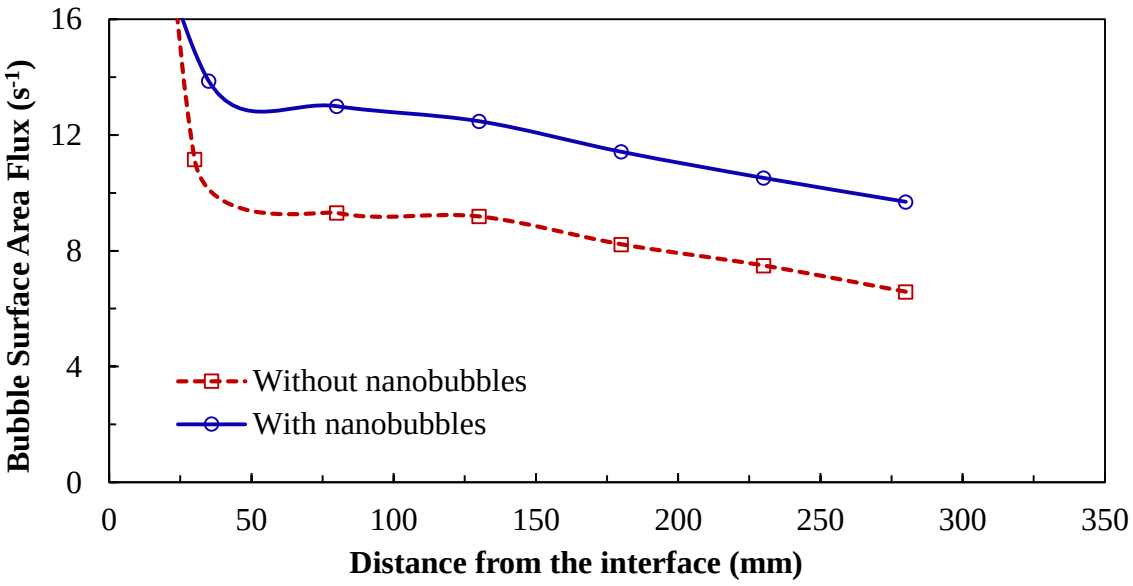

Figure 4-81. Variation of bubble surface area flux as a function of froth height for strongly hydrophobic glass ($\theta = 85^{o}$) with and without nanobubbles in column flotation.

4.6. ECONOMIC EVALUATION OF NANOBUBBLE ENHANCED FINE COAL FLOTATION

Depending on the type of flotation equipment used and characteristics of the coal being processed, the recovery improvement achieved with nanobubbles varied from 5% up to more than 50%. To estimate the potential economic benefits of applying nanobubbles in the flotation process, an economic evaluation was conducted.

The economic evaluation is based on assuming the average ash content of the feed is about 35% and the flotation feed is about 100 ton/hr. The cost associated with nanobubble application includes operational and capital costs. The capital cost mainly includes cavitation tubes and additional pumps.

A 100 ton/hr flotation feed requires one bank of conventional cells, which can be either 4-compartment or 6-compartment with a processing capacity of 100 ton/hr. With a solids concentration of 10%, each conventional flotation cell will have a flow rate of about 1000 m^3/hr (0.278 m^3/s). Compared to the laboratory scale cavitation tube, this flow rate is much larger; consequently, the cavitation tube size will be increased to avoid possible congestion. To minimize energy consumption by the cavitation tube, feed with this flow rate can be directed to flotation cells through multiple Venturi tubes. For the flow rate of 0.278 m^3/s, one Venturi tubes can be used for each flotation bank, with the size of 4" at the throat and 16" at the cylindrical part. The pressure drop under this feed flow rate and Venturi tube is 88 Kpa, higher than the threshold value of 69 Kpa measured at the laboratory. The total cost of a Venturi tube is $8,000. The Venturi tube will last in about three months and thus the annual cost will $32,000.

As the installation of cavitation tubes increases the resistance to the feed flow, an additional pump may be needed to maintain the flow rate. A Goulds Model JCU submersible slurry pump with a total flow rate of 4000 GPM or 0.25 m^3/s can be used for this purpose. The current price for this model is about $15,000. Assuming the pump will

last five years and allowing for inflation and warehousing costs, the annual cost will be approximately $5,000.

Therefore, total annual equipment cost will be $37,000. Considering a factor of 1.1 for miscellaneous accessories (including valves and flow meters) and a factor of 1.3 for installation cost, the total capital cost becomes about $52,910.

Based on our measurement with the laboratory nanobubble generator, it is estimated that energy consumption will be increased by less than 5 kwh/ton of solids if the pump efficiency is 55%. Assuming the cost of the electricity is $0.12/kwh, the cost of electricity per year is $240,000 (=$0.12/kw x 5 kwh/ton x 4000 hours/year x 100 ton/hr). Thus, the total increase in costs for the nanobubble application is $52,910 + $240,000 = $292,910 each year.

For the Illinois coal tested, the recovery improvement can be as great as 35% with column flotation. To make a conservative estimation, the recovery improvement for an industrial application is assumed to be 10%.

With 100 ton/hr, flotation feed rate, 35% average ash content, 10% product ash requirement, and 10% combustible recovery improvement, the total increase in flotation product per hour would be:

100 ton/hr x (1-35%) x 10%/ (1-10%) = 7.2 ton/hr.

At the current price for clean coal of about $60/ton, the annual revenue generated by nanobubble application would be, assuming 4000 working hr/year:

7.2 ton/hr x 4000 hr/year x $60/ton = $1,728,000.

Therefore, the net profit brought by nanobubble application would be:

$1,728,000 - $292,910 = $1,435,090.

CHAPTER 5. CONCLUSIONS

Laboratory nanobubble application to coal flotation has proven very successful. It not only significantly improved combustible recovery, but also reduced reagent consumption. An economic evaluation has shown this technique is economically applicable, even for a plant with small processing capacity. Specific conclusions are:

- Nanobubbles significantly enhanced the coal flotation process efficiency with higher recovery.

- The flotation recovery of fine coal was increased by 5 to 50 absolute percentage points for different particle size fractions, depending on process operating conditions.

- Collector dosage was reduced by about one-half as a result of the adsorption of nanobubbles on coal particle surfaces. Nanobubbles have a stronger affinity for hydrophobic solid surfaces than conventional-sized bubbles and can act as a strong secondary collector.

- The frother dosage was also reduced by up to one-third because nanobubbles are mostly smaller than 1 μm when they are formed from dissolved air in the slurry. This is because nanobubbles significantly influence the froth stability as a result of increasing particle hydrophobicity, and the maximum froth stability was accomplished when froth zone contains particles with moderately hydrophobic with a contact angle of about 70^{o}. Furthermore, the existence of nanobubbles on the hydrophobic particles and in the slurry significantly increased the bubble surface area flux.

- The improved flotation performance by nanobubbles can be attributed to increased probabilities of collision and attachment and reduced probability of detachment.

- Nanobubbles improved flotation separation performance with coal particles in all size ranges, especially with ultrafine and relatively coarse coal particles.

- The best conditions for column flotation with nanobubbles included a feed rate of 0.5 cm/s, an aeration rate of 0.5 cm/s with wash water rate of 0.1 cm/s (or aeration rate of 1.20 cm/s with wash water rate of 0.16 cm/s), frother concentration of 30-35 ppm, collector dosage 0.3 kg/ton, and slurry distribution ratio of 60% to the cavitation tube.

- Nanobubble application increased the kinetic flotation rate constant by 41%, which implies a significant increase in processing capacity.

- Nanobubbles coated particles form aggregates and in consequence enhance particle bubble collisions probability.

- Nanobubbles generated on the surface of a hydrophobic particle improved the attachment probability by reducing the induction time by up to one-half.

- For a coal washing plant with a 100 ton/hr feed rate to the flotation cell, the annual increase in profit from nanobubble application is estimated at close to $1.44 million.

CHAPTER 6. SUGGESTIONS FOR FUTURE STUDY

The results of this work showed that nanobubbles significantly improved fine coal separation performance. However, the following further studies are recommended to estimate the benefits that can be obtained by using the nanobubbles technology in froth flotation process:

- More fundamental studies that deal with the hydrodynamic conditions and the effect of the nanobubbles are needed to better understand how nanobubbles enhance the flotation process performance.

- Nanobubble enhanced column flotation should be applied to a wide variety of minerals.

- Feasibility study should be performed using the data generated from the pilot and industrial scale-testing program.

REFERENCES

Agrawal, A. and McKinley, G.H., 2006, Mater. Res. Soc. Symp. Proc. 899E

Albijanic, B., Ozdemir, O., Nguyen, A.V. and Bradshaw, D., 2010, "A review of induction and attachment times of wetting thin films between air bubbles and particles and its relevance in the separation of particles by flotation", Advances in Colloid and Interface Science, 159: 19:j.

Ata, S., Ahmed, N. and Jameson, G.J., 2003, "A study of bubble coalescence in flotation froths", International Journal of Mineral Processing, 72: 255-266.

Ata, S., 2009, "The detachment of particles from coalescing bubble pairs", Journal of Colloid and Interface Science, 338: 558-565.

Ata, S. (2012), "Phenomena in the froth phase of flotation – a review", International Journal of Mineral Processing, 102-103: 1-12.

Aveyard, R., Binks, B.P., Fletcher, P.D.I., Peck, T.G. and Rutherford, C.E., 1994, "Aspects of aqueous foam stability in the presence of hydrocarbon oils and solid particles", Advanced Colloid Interface Science, 48: 93–120.

Blake, P. and Ralston, J., 1985, "Controlled methylation of quartz particles", Colloids and Surfaces, 15: 101-118.

Contini, N.J., Wilson, N.S. and Dobby, G., 1988, "Measurements of rate data in flotation columns", Column Flotation 88, SME/AIME, 69–80.

Derjaguin, B.V. and Dukhin, S.S., 1960, "Theory of flotation of small and medium size particles", Trans. Inst. Mining Met., 70: 221.

Dippenaar, A., 1982, "The destabilization of froth by solids: I. The mechanism of film rupture" International Journal of Mineral Processing, 9: 1–14.

Fan, M., Tao, D., 2008, “A study on picobubble enhanced coarse phosphate froth flotation, Separation Science and Technology”, 43(1): 1-10.

Fan, M., Tao, D., Honaker, R., Luo, Z., 2010a, “Nanobubble generation and its application in froth flotation (Part I): Nanobubble generation and its effects on the properties of microbubble and millimeter scale bubble solutions”, Mining Science and Technology (China), 20(1): 1-19.

Fan, M., Tao, D., Honaker, R., Luo, Z.F., 2010b, “Nanobubble generation and its application in froth flotation (part II): Fundamental study and theoretical analysis”, Mining Science and Technology”, 20(2): 159-177.

Fan, M., Tao, D., Honaker, R., Luo, Z.F., 2010c, “Nanobubble generation and its application in froth flotation (part III): Specially designed laboratory scale column flotation of phosphate”, Mining Science and Technology, 20(3): 317-338.

Fan, M., Tao, D., Honaker, R., Luo, Z.F., 2010d, “Nanobubble generation and its application in froth flotation (part IV): Mechanical cells and specially designed column flotation of coal”, Mining Science and Technology, 20(5): 641-671.

Fan, M., Zhao, Y. and Tao, D., 2012, “Fundamental studies of nanobubble generation and applications in flotation”, Separation Technologies for Minerals, Coal and Earth Resources, 2012 Society for Mining, Metallurgy, and Exploration (SME), 459-469.

Farmer, A.D., Collings, A.F. and Jameson, G.J., 2000, “Effect of ultrasound on surface cleaning of silica particles”, International Journal of Mineral Processing, 60: 101-113.

Gaudin, A.M., 1957. “Flotation”, McGraw-Hill, New York, 2nd Edition, 573.

Hampton, M.A., Donose, B.C. and Nguyen, A.V., 2008, “Effect of alcohol-water exchange and surface scanning on nanobubbles and the attraction between hydrophobic surfaces”, Journal of Colloid and Interface Science, 325: 267-274.

Hampton, M.A. and Nguyen, A.V., 2010, “Nanobubbles and the nanobubble bridging capillary force”, Advances in Colloid and Interface Science, 154(1-2): 30-55.

Heindel, T.J. 1997, “Fundamentals of flotation deinking”, TAPPI Journal, 82: 115-124.

Heiskanen, K., 2000, “On the relationships between flotation rate and bubble surface area flux”. Mineral Engineering, 13(2): 141–149.

Hemmings, C.E., 1981, "On the significance of flotation froth liquid lamella thickness", Transactions of the Institution of Mining and Metallurgy, 90: C96-C102.

Ishida, N., Kusaka, Y. and Ushijima, H., 2012, “Hydrophobic attractive between silanated silica surfaces in the absence of bridging bubbles”, Langmuir, American Chemical Society, 13952-13959.

Jameson, G.J., Nam, S. and Young, M.M, 1977, “Physical factors affecting recovery rates in flotation”, Minerals Science and Engineering, 9: 103-118.

Johansson, G. and Pugh, R.J., 1992, “The influence of particle size and hydrophobicity on the stability of mineralized froths”, International Journal of Mineral Processing, 34: 1–20.

Johansson, B., Pugh, R. and Alexandrova, L., 2000, “Flotation de-inking studies using model hydrophobic particles and non-ionic dispersants”, Colloids and Surfaces, 170: 217-229.

Johnson B. and Cooke, R., 1981, “Generation of stabilized microbubbles in seawater”, Science, 213: 209–211.

Jowett, A., 1980, “Formation and disruption of particle-bubble aggregates in flotation”, Fine Particles Processing, 1: P Somasundaran (Ed.). AIME, New York, N.Y, 720-754

Kennedy, D.L., 2008, “Redesign of industrial column flotation circuits based on a simple residence time distribution model”, Master of Science, Virginia Polytechnic Institute and State University, 6-8.

Kim, J.Y., Song, M.G. and Kim, J.D., 2000, “Zeta Potential of Nanobubbles Generated by Ultrasonication in Aqueous Alkyl Polyglycoside Solutions”, Journal of Colloid Interface Science, 223: 285-291.

Ibe, O.C., 2013, “Brownian motion”, Markov Processes for Stochastic Modeling (Second Edition), 263-293, http://dx.doi.org/10.1016/B978-0-12-407795-9.00009-8.

Kukizaki, M. and Goto, M., 2006, “Size control of nanobubbles generated from Shirasu-porous-glass (SPG) memberanes”, Journal of Membrane Science, 281: 386-396.

Lou, S.T., Ouyang, Z-Q., Zhang, Y., Li, X-J., Hu, J., Li, M-Q., and Yang, F-J., 2000, “Nanobubbles on solid surface imaged by atomic force microscopy”, Journal of Vacuum Science and Technology B, 18: 2573–2575.

Lovell, V.M., 1976, In: Fuerstenau, M.C. (Ed.), Flotation A.M. Gaudin Memorial volume. AIME, New York.

Luttrell G.H. and Yoon, R.-H., 1992, “A hydrodynamic model for bubble-particle attachment”, Journal of Colloid Interface Science, 154: 129–137.

Lynch, A.J., Johnson, N.W., McKee, D.J. and Thorne, G.C., 1974,"The behavior of minerals in sulfide flotation processes, with reference to simulation and control", Journal of the South African Institute of Mining and Metallurgy, 74: 349-361.

Mao, L. and Yoon, R.-H., 1997, “Predicting flotation rates using a rate equation derived from first principles,” International Journal of Mineral Processing, 51: 171-181.

Mishchuk, N., 2004, “The role of hydrophobicity and dissolved gases in non-equilibrium surface phenomena”, Colloids and Surfaces A: Physicochemical and Engineering Aspects, 267 (1-3): 139-152.

Mishchuk, N., Ralston, J. and Fomasiero, D., 2006, “Influence of very small bubbles on particle/bubble heterocoagulation”, Journal of Colloid and Interface Science, 301: 168-175.

Moys, M.H., 1978, "A study of a plug-flow model for flotation froth behavior", International Journal of Mineral Processing, 5: 21-38.

Nesset, J.E., Gomez, C.O., Finch, J.A., Hernandez-Aguilar, J.R. and Difeo, A., 2005, “The use of gas dispersion measurements to improve flotation Performance”, 37th Annual Meeting of the Canadian Mineral Processors (CMP), Ottawa, on, Canada, 401-421.

Nguyen, A.V., Schulze, H.J. and Ralston, J., 1997, “Elementary steps in particle-bubble attachment”, International Journal of Mineral Processing, 51: 183-195.

Nguyen, A.V., Ralston, J. and Schulze, H.J., 1998, “On modeling of bubble-particle attachment probability in flotation”, International Journal of Mineral Processing, 53(4): 255-249.

Nguyen, A.V. and Schulze, H.J., 2004, “Colloidal science of flotation”, Surfactant Science Series, 118: 173-182.

Ohgaki, K., Khan, N.Q., Joden, Y., Tsuji, A. and Nakagawa, T., 2010, “Physicochemical approach to nanobubbles solution”, Chemical Engineering Science, 65(3): 1296–1300.

Paxton, W.F., Kistler, K.C., Olmeda, C.C., Sen, A., Angelo, S.K., Cao, Y.Y., Mallouk, T.E., Lammert, P.E., and Crespi, V.H., 2004, “Catalytic nanomotors autonomous

movement of striped nanorods", Journal of American Chemical Society, 126: 13424-13431.

Ralston, J. and Dukhin, S.S., 1999, "Interaction between particles and bubbles", Colloids and Surfaces A: Physicochemical and Engineering Aspects, 151: 3–14.

Pashley, R.M. and Karaman, M.E., 2005, "Bubble coalescence, foam and thin surfactant films", in Applied Colloid and Surface Chemistry, John Wiley & Sons, Ltd, Chichester, UK. doi: 10.1002/0470014709.ch8.

Plate, H. PhD Thesis, ADW, UVR, Freiberg/Sa. Chemnitzer Str. 40, unpubl. (Work quoted in Schulze, H.J., 1993, "Flotation as a heterocoagulation process: Possibilities of calculating the probability of flotation", B. Dobias (Ed.), Coagulation and Flocculation, 321–353.).

Raut, J.S., Stoyanov, S.D., Duggal, C., Pelan, E.G., Arnaudov, L.N. and Naik, V.M., 2012, "Hydrodynamic cavitation: a bottom-up approach to liquid aeration", Soft Matter, 8, 4562.

Sagert, N.H. and Quinn, M.J., 1978, "The coalescence of gas bubbles in dilute aqueous solutions", Chemical Engineering Science, 33: 1087-1095.

Schimmoller, B.K., Luttrell, G.H. and Yoon, R-H., 1993, "A combined hydrodynamic-surface force model for bubble-particle collection", XVIII International Mineral Processing Congress, Sydney, 23-28 May 1993, 751-756.

Schubert, H. and Bischofberger, C., 1979, "On the optimization of hydrodynamics in flotation processes," Proceedings of 13th International Mineral Processing Congress, Warszawa, 2: 1261-1287.

Schubert, H., 2005, "Nanobubbles, hydrophobic effect, heterocoagulation and hydrodynamics in flotation", International Journal of Mineral Processing, 78: 11-21.

Schulze, H.J., 1984, “Flotation as a hetero-coagulation process: possibilities of calculating the probability of flotation”, in Physico-Chemical Processes in Flotation, Chapter 7, Elsevier, Berlin.

Schulze, H.J., 1989, “Hydrodynamics of bubble-mineral particle collisions”, in Frothing in Flotation, Laskowski, J.S. (Ed.), Mineral Processing and Extractive Metallurgy Review: The Jan Leja Volume Gordon & Breach, New York, 5: 43-76.

Seddon, J.R.T., Kooij, E.S., Poelsema, B., Zandvliet, H.J.W. and Lohse, D., 2011, “Surface bubble nucleation stability”, Physical Review Letters, 106(5): 056101:1-4.

Shaw, D., 1992, “Introduction to Colloid and Surface Chemistry”, 4th Edition, Butterworth-Heinemann, Elsevier Science Ltd., 270-274.

Simonsen, A.C., Hansen, P.L., and Klosgen, B., 2004, “Nanobubbles give evidence of incomplete wetting at a hydrophobic interface”, Journal of Colloid and Interface Science, 273: 291-299.

Stockelhuber, K.W., Radoev, B., Wenger, A. and Schulze, H.J., 2004, “Rupture of wetting films caused by nanobubbles”, Langmuir, 20: 164-168.

Szatkowski, M. and Freyberger, W.L., 1985, "Kinetics of flotation with fine bubbles", Transactions of the Institution of Mining and Metallurgy, 94: C61-C70.

Tadros, T.F., 2005, “Role of surfactants in wetting, spreading and adhesion, in Applied Aurfactants: Principles and Applications”, Wiley-VCH Verlag GmbH & Co. KGaA, Weinheim, FRG. doi: 10.1002/3527604812.ch11.

Tao, D., Luttrell, G.H. and Yoon, R.-H., 2000, “A parametric study of froth stability and its effect on column flotation of fine particles”, International Journal of Mineral Processing, 59: 25–43.

Tao, D., 2004, “Role of bubble size in flotation of coarse and fine particles - a review”, Separation Science and Technology, 39(4): 741-760.

Tao, Y., Liu, J., Yu, S. and Tao, D., 2006, "Picobubble Enhanced Fine Coal Flotation", Separation Science and Technology, 41: 3597-3607.

Tao, D., Yu, S., Zhou, X., Honaker, R.Q. and Parekh, B.K., 2008, "Picobubble column flotation of fine coal", International Journal of Coal Preparation and Utilization, 28(1): 1-14.

Tao, D., Fan, M. and Honaker, R., 2010, "Enhanced fine coal column flotation using cavitation concept", International Coal Preparation Congress XVIICPC 2010 Conference Proceedings, 413-420.

Anon., U.S. Energy Information Administration, 2009 (http://www.eia.gov/cneaf/coal/page/acr/tables2.html)

Ushikubo, F.Y., Furukawa, T., Nakagawa, R., Enari, M., Makino, Y., Kawagoe, Y., Shiina, T. and Oshita, S., 2010, "Evidence of the existence and the stability of nano-bubbles in water", Colloids and Surfaces A: Physicochemical Engineering Aspects, 361: 31–37.

Verrelli, D.I., Koh, P.T.L. and Nguyen, A.V., 2011, "Particle-bubble interaction and attachment in flotation", Chemical Engineering Science, 66: 5910-5921.

Weber, M.E. and Paddock, D., 1983, "Interceptional and gravitational collision efficiencies for single collectors at intermediate Reynolds numbers," Journal of Colloid Interface Science, 94: 328-335.

Wiegel, R.L., Lawver, J.E., 1986, "Reducing theory to practice (or vice versa) in mineral processing", In Advances in Mineral Processing, SME/AIME, 685–694.

Anon., World Coal Association, Dec. 2011 (http://www.worldcoal.org/coal/uses-of-coal/)

Yang, S., Dammer, S.M., Bremond, N., Zandvliet, H.J.W., Kooij, E.S. and Lohse, D., 2007, "Characterization of nanobubbles on hydrophobic surfaces in water", Langmuir, 23: 7072–7077.

Yang, S., Tsai, P., Kooij, E.S., Prosperetti, A., Zandvliet, H.J.W. and Lohse, D., 2009, "Electrolytically generated nanobubbles on highly orientated pyrolytic graphite surfaces", Langmuir, 25: 1466-1474.

Yoon, R.-H. and Luttrell, G.H., 1989, "The Effect of Bubble Size on Fine Particle Flotation", Mineral Processing Extractive Metallurgy, Revised, 5: 101-122.

Yoon, R.-H., Luttrell, G.G., Adel, G.T. and Mankosa, M.J., 1989, "Recent advances in fine coal flotation. In advances in coal and mineral processing using flotation", Chander, S., Ed.; Society of Mining Engineers: Littleton, CO, Chap, 23: 211-218.

Yoon, R.-H., 1993, "Microbubble flotation", Minerals Engineering, 6(6): 619-630.

Yoon, R.-H., 2000, "The role of hydrodynamic and surface forces in bubble-particle interaction," International Journal of Mineral Processing, 58: 128-143.

Young, F R., 1989, "Cavitation", McGraw-Hill Book Company, London.

Zhang, X., Kumar, A. and Scales, P.J., 2011, "Effect of solvency and interfacial nanobubbles on surface forces and bubble attachment at solid surface", Langmuir, American Chemical Society, 2484-2491.

Zhang, X.H., Zhang, X.D., Lou, S.T., Zhang, Z.X., Sun, J.L. and Hu, J., 2004, "Degassing and temperature effects on the formation of nanobubbles at the mica/water interface", Langmuir, 20: 3813-3815.

Zhang, X.H., Wu, Z.H., Zhang, X.D., Li, G., and Hu, J., 2005, "Nanobubbles at the interface of HOPG and ethanol solution", International Journal of Nanoscience, 3: 399-407.

Zhang, X.H., Maeda, N. and Craig, V.S.J., 2006a, "Physical properties of nanobubbles on hydrophobic surface in water and aqueous solutions", Langmuir, 22: 5025–35.

Zhang, L.J.., Zhang, Y., Zhang, X.H., Li, Z.X., Shen, G.X., Ye, M., Fan, C.H., Fang, H.P. and Hu, J., 2006b, "Electrochemically controlled formation and growth of hydrogen nanobubbles", Langmuir, 22: 8109-8113.

Zhang, X.H., Zhang, X., Sun, J., Zhang, Z., Li, G., Fang, H., Xiao, X., Zeng, X. and Hu, J., 2007, "Detection of novel gaseous states at the highly oriented pyrolytic graphite-water interface", Langmuir, 23: 1778-1783.

Zhang, W., 2009, "Water overflow rate and bubble surface area flux in flotation", Master of Engineering, Department of Mining and Materials Engineering, McGill University, Montreal, Canada.

Zhang, X.H. and Maeda, N., 2011, "Interfacial gaseous states on crystalline surfaces", Journal of Physical Chemistry, 115: 736-743.

Zhang, X.H., Khan, A. and Ducker, W.A., 2007, "A nanoscale gas state", Physics Review Letters, 98: 136101.

Zhou, Z.A. Xu, Z. Finch, J.A. Hu, H. and Rao, S.R., 1997, "Role of hydrodynamic cavitation in fine particle flotation", International Journal of Mineral Processing, 51: 139–149.

VITA

Author's Name: Ahmed Sobhy Abdel-Fattah Sayed-Ahmed

Birthplace: Egypt

EDUCATION

- Ph.D. Candidate in Mining and Mineral Processing Engineering, University of Kentucky, Lexington, January 2010 – present
- M.Sc. in Physical Chemistry, Cairo University, Egypt, November 2008.
- International Summer Course in Material Processes, Royal Institute of Technology, Sweden, July 2006
- Pre-Master Study in Inorganic Chemistry, Cairo University, Egypt, October 2005
- Bachelor of Science (B.Sc.) in Special Chemistry, Cairo University, Egypt, May 2003

PROFESSIONAL POSITIONS

- Graduate Research Assistant & Teaching Assistant, University of Kentucky, Lexington, KY, 1/10 – present
- Assistant Researcher & Assistant Lecturer, Central Metallurgical R&D Institute, El-Tibbin, Cairo, Egypt, 1/09 – present
- Visiting Scholar, University of Kentucky, Lexington, KY, 8/08 – 7/09
- Research Assistant, Central Metallurgical R&D Institute, El-Tibbin, Cairo, Egypt, 5/04 – 12/08

JOURNAL PUBLICATIONS

- **Sobhy, A.** and Tao, D., 2013, "Nanobubble column flotation of fine coal particles and associated fundamentals", International Journal of Mineral Processing, http://dx.doi.org/10.1016/j.minpro.2013.04.016.

- Tao, D., **Sobhy, A.**, Li., Q. and Honaker, R., 2011, "Dry cleaning of pulverized coal using a novel rotary triboelectrostatic separator (RTS)", International Journal of Coal Preparation and Utilization, 31: 187-202.
- Selim, A.Q., El-Midany, A.A., **Abdel-Fattah, A.S.**, Ibrahim, S.S., 2010, "Rationalization of the up-grading circuit of celestite for advanced applications", Powder Technology, 198(2), 233 – 239.

OTHER PUBLICATIONS

- Sobhy, A. and Tao, D., 2013, "Innovative RTS technology for dry beneficiation of phosphate", 2nd International Symposium on Innovation and Technology in the Phosphate Industry [SYMPHOS 2013].
- **Sobhy, A.**, Honaker, R. and Tao, D., 2013, "Nanobubble column flotation for more efficient coal recovery", 2013 SME Annual Meeting & Exhibit and CMA 115th National Western Mining Conference.
- **Sobhy, A.** and Tao, D., 2012, "Nanobubble enhanced flotation – fundamental and mineral application", Rare Earth Elements Conference, San Diego, CA, USA.
- Tao, D., **Sobhy, A.**, Li., Q. and Honaker, R., 2010, "Pre-Combustion Cleaning of Pulverized Fine Coal at Power Plant Using Novel RTS Dry Separation Technology", twenty – Seventh Annual International Pittsburgh Coal Conference, October 11 - 14, Hilton Istanbul, Istanbul, TURKEY.
- Tao, D., **Sobhy, A.**, Li., Q. and Honaker, R., 2010, "Dry Fine Coal Cleaning Using Rotary Triboelectrostatic Separator (RTS)", Annual SME Meeting, Phoenix, AZ.
- El-Midany, A.A., **Abdel-Fattah, A.S.**, Ibrahim, S.S., 2009, "The Assessment of Falcon Concentrator Performance in Celestite Separation", MPM 11, 15-18 March, Sharm El-Sheikh, Egypt.
- El-Midany, A.A., **Abdel-Fattah, A.S.**, Ibrahim, S.S., 2008, "Statistical Modeling of Celestite Separation Using Jigging Process", Proceeding of the 11th International Processing Symposium 21-23 October, Betek Antalya, Turkey.

HONORS AND AWARDS

- The second place in the Educational Sustainability Graduate Student Poster Contest "Nanobubble effect on particle-bubble interaction in froth flotation", 2013 SME Annual Meeting & Exhibit and CMA 115th National Western Mining Conference
- Partnership and Ownership fellowship (ParOwn) for 6 months in 2008, Ministry of Higher Education and State for Scientific Research of Egypt

MEMBER

- SME - Society for Mining, Metallurgy and Exploration
- Golden Key International Honor Society

Ahmed Sobhy Sayed Ahmed

Student's Signature

8/21/2013

Date